Charles University

Faculty of Science

Study programme: Chemistry (N1407)

Branch of study: NANORD (1401T002)

Bc. David Dunlop

Development of novel photoactive cationic zirconocene complexes
Vývoj nových fotoaktivních kationtových zirkonocenových komplexů

Diploma thesis

Supervisor: RNDr. Martin Lamač Ph.D.
Advisor: prof. RNDr. Petr Štěpnička, Ph.D., DSc.

Prague, 2021

Declaration

I hereby declare that this thesis is my original work. All information sources and literature are cited in full. The thesis has not been submitted or is not being concurrently submitted for the same or other academic degree.

Prohlášení

Prohlašuji, že jsem tuto závěrečnou práci zpracoval samostatně a že jsem uvedl všechny použité informační zdroje a literaturu. Tato práce ani její podstatná část nebyla předložena k získání jiného nebo stejného akademického titulu.

In Prague, 22. 8. 2021 Bc. David Dunlop

Acknowledgments

At the time of writing this thesis, we have been impacted continuously for over a year by the COVID-19 pandemic, with no end in sight. The pandemic introduced obstacles to our daily lives, work and education. Countless had both their physical and psychological well-being impaired and many lives were lost. Therefore, I would first like to honour and thank everybody who put their lives on the line to provide us healthcare, goods and services, ensured that education would not halt completely and also those who simply stayed strong despite the dire situation. It is you to whom the future generations owe for pulling through.

As for the persons I wish to acknowledge. I express my sincerest gratitude to Dr. Martin Lamač who had the patience, motivation and most importantly the skill to guide me through my first scientific endeavours. Without him, I would have most likely continued on my original path of becoming a failed dental assistant.

I owe my friends, family, my soulmate Veronika and my dog Björn a heartfelt ‘thank you’, for the endless emotional support they provided me.

I would like to thank Dr. Tomáš Slanina (mentorship), doc. Róbert Gyepes (X-ray), Miloš Večeřa (synthesis), Dr. Pavel Kubát and Dr. Kamil Lang (photophysical characterization), Dr. Ludmila Petrusová (melting points) and Dr. Jiří Pinkas and Dr. Michal Horáček (NMR and elemental analysis) and Ondřej Groborz (proofreading) for their contributions to the project discussed in this thesis. I thank as well prof. Petr Štěpnička and Dr. Jiří Schulz for their part in facilitating my scientific work.

I would also like to thank Dr. Tomáš Hodík for keeping me company during my writing sessions, an acknowledgment he himself unapologetically demanded.

Lastly, I would like to thank myself. I truly did not expect to make it this far.

This work has been supported by the Czech Science Foundation (project no. 1900204S).

Název práce: Vývoj nových fotoaktivních kationtových zirkonocenových komplexů

Autor: Bc. David Dunlop

Katedra: Katedra anorganické chemie

Vedoucí práce: RNDr. Martin Lamač Ph.D

Konzultant: prof. RNDr. Petr Štěpnička, Ph.D., DSc.

Abstrakt: Současné obavy o životní prostředí daly vznik nebývalé poptávce po udržitelných zdrojích energie, mezi nimiž elektromagnetické záření, světlo, dominuje. V důsledku je vývoj světlo-sběrných materiálů jedním z předních témat současné vědy, neboť je nezbytný pro náš technologický pokrok.

Diplomová práce přispívá do tohoto oboru vývojem nových fotoaktivních sloučenin na bázi kationtových metalocenových komplexů 4. skupiny. Kationtové sloučeniny jsou stabilizovány coby soli aniontu $[B(C_6F_5)_4]^-$ intramolekulárně vázanými iminovými a pyridinylovými či *N,O*-chelatujícími aromatickými ligandy. Příprava je založena na protonaci iminových skupin výchozích látek pomocí $PhNMe_2H[B(C_6F_5)_4]$, či abstrakci chloridového ligandu pomocí $Li[B(C_6F_5)_4]\cdot 2.5Et_2O$ nebo $Ph_3C[B(C_6F_5)_4]$/2 eq. Et_3SiH. Látky byly charakterizovány pomocí monokrystalové rentgenové difrakční analýzy a NMR spektroskopie. Dále byla provedena studie jejich fotofyzikálních vlastností. Kationtové komplexy emitují z tripletových excitovaných stavů, které odpovídají přechodům přenosu náboje ligand-kov. Doba života luminiscence činí až 62 µs a kvantové výtěžky luminescence až 58 %, v pevné fázi, při pokojové teplotě. Fotofyzikální vlastnosti byly výpočetně podloženy. Připravené komplexy byly dále prověřeny coby fotosenzitizéry singletového kyslíku (s kvantovými výtěžky až 77 % v roztocích) a coby fotokatalyzátory redukce arylhalogenidů (redukce bromopentafluorobenzenu proběhla s kompletní konverzí).

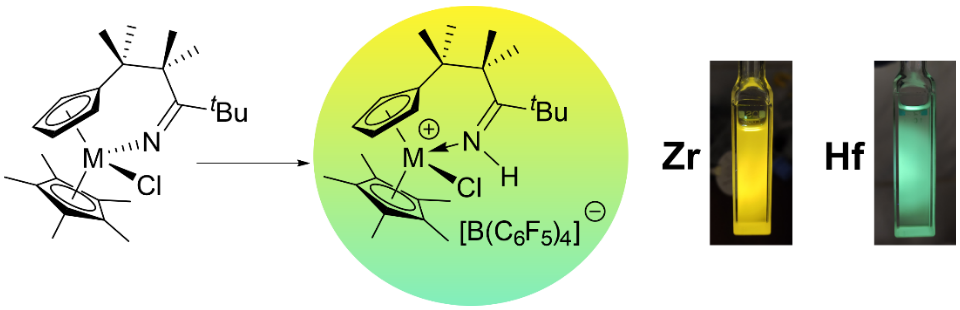

Klíčová slova: metalocenové komplexy, prvky 4. skupiny, luminiscence, DFT, singletový kyslík, fotoredoxní katalýza, LMCT

Title: Development of novel photoactive cationic zirconocene complexes

Author: Bc. David Dunlop

Department: Department of inorganic chemistry

Supervisor: RNDr. Martin Lamač Ph.D.

Advisor: prof. RNDr. Petr Štěpnička, Ph.D., DSc.

Abstract: Environmental concerns have brought about an unprecedented demand for sustainable energy sources among which electromagnetic radiation, light, currently dominates. Development of novel light-harvesting compounds and materials is at the forefront of current science, as it is essential to further our technological progress.

This thesis contributes to the field by development of novel photoactive cationic group 4 metallocene complexes stabilized by pendant imine and pyridinyl donor groups, or *N*,*O*-donor aromatic ligands, as crystalline $[B(C_6F_5)_4]^-$ salts. The complexes are prepared either by protonation of the intramolecularly bound imine moiety by $PhNMe_2H[B(C_6F_5)_4]$ or by chloride ligand abstraction, by $Li[B(C_6F_5)_4]\cdot 2.5Et_2O$ or *in situ* generated $Et_3Si[B(C_6F_5)_4]$. Prepared compounds were characterized by NMR spectroscopy. Solid state structures of the compounds were determined by X-ray diffraction analysis. The cationic complexes of Zr and Hf exhibited significantly enhanced luminescence which originates from triplet ligand-to-metal (^{3}LMCT) excited states with lifetimes of up to 62 μs and quantum yields of up to 58% in the solid state, at room temperature. DFT calculations were performed to explain the photophysical properties of the complexes. The complexes were investigated as potential photosensitizers of singlet oxygen (quantum yields of up to 77% in solution) and for applications in photoredox catalyzed reduction of arylhalogenides (reduction of bromopentafluorobenzene proceeded with complete conversion).

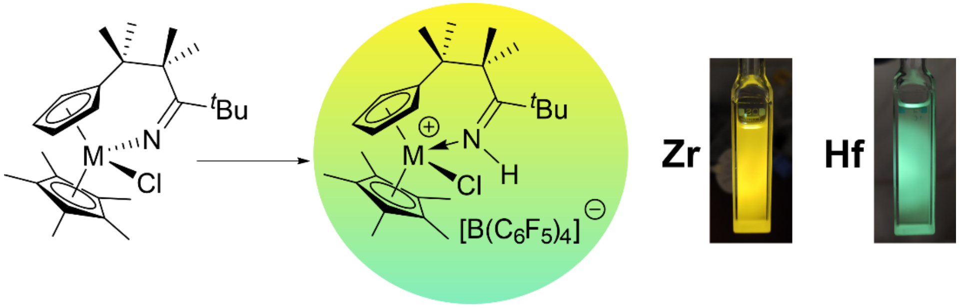

Keywords: metallocene complexes, group 4 elements, luminescence, DFT, singlet oxygen, photoredox catalysis, LMCT

Table of contents

1 Foreword

Electromagnetic radiation is the most abundant energy source on Earth. Most living creatures on the face of our planet benefit daily from the roughly 1360 kW m^{-1} of energy carried by sunlight, including humans.[1] Not only that Sun's energy allows us to live our lives in a comfortable range of temperatures, but it is also the progenitor of various life-dependent photophysical and photochemical phenomena. Examples of such processes are 1) light-induced charge separation in thylakoid membranes which fuel the 'light phase' of photosynthesis (Figure 1) upon which all plant life depends,[2] 2) light induced isomerization of 11-*cis*-retinal (Figure 2), which drives the nerve impulse behind human vision,[3] 3) UV-dependent transformation of 7-dehydrocholesterol to cholecalciferol (vitamin D_3; Figure 2), an essential compound of human metabolism.[4]

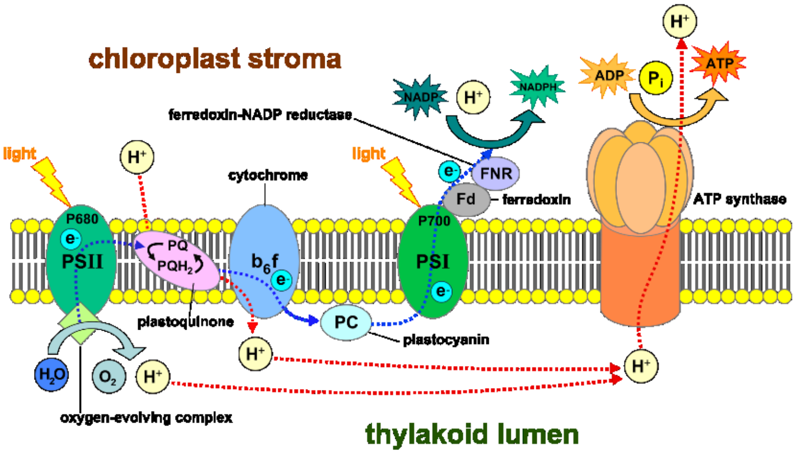

Figure 1: Schematic depiction of the light-dependent reactions on the thylakoid membrane. Reprinted from Wikimedia Commons, 2015. Creative Commons Attribution-Share Alike 4.0 International license.

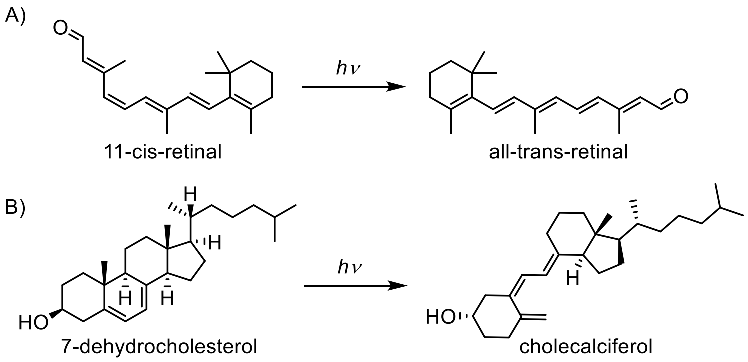

Figure 2: (A) Light-induced isomerization of 11-cis-retinal to all-trans-retinal. (B) Light-induced transformation of 7-dehydrocholesterol to cholecalciferol.

Although light is a rich source of energy, mankind has utilized it only scarcely throughout its technological evolution. Until recently, human technology mainly relied on manpower and combustible energy sources.[5] The simplistic nature of combustible energy sources is quite practical. They can be easily stored, transported and traded. The rather simple process of oxidizing black coal produces roughly 25 MJ kg^{-1}, which are sufficient to boil water, cook meat, but also power steam locomotives. The downside of combustible energy sources are the products of their combustion which are pathological to our environment (CO_2) and even our health (CO, SO_2). The addition of nuclear power to our energy source arsenal, a promising technology in its own right, did little to reduce our dependency on combustible energy sources and moreover, introduced worse possible outcomes to the human story.[6]

Therefore, we must ask with an ever-increasing urgency: 'How will we fuel our civilization, without dooming the generations to come?'

Unfortunately, this diploma thesis does not solve that question. However, it aims to contribute to one of its possible answers: Light.

Unlike the destructive combustion, light induces a rich variety of transformative processes which remain largely unexplored. Yet, as we will discuss further on, it has been well established that in contrast to heat produced by combustion, light-induced transformations can be utilized on a molecular level to promote processes which are inconceivable in 'ground state chemistry'. Light harvesting develops hand in hand with multiple fields, including visualization technologies, photocatalysis, medicine and molecular machinery.

Light harvesting is therefore a deep well of opportunities. The field inspires curiosity of current scientists and is considered one of the forefronts of humanity's knowledge. As we have traversed the technological path of combustion from campfires to locomotives, our civilization has now entered the path of light-harvesting…

…this work is one of many steps of this exciting journey.

David Dunlop

2 Theoretical background

The following chapter establishes context for the main body of this work, its experimental section. It is tailored to be well understood by a broad range of readers. The chapter introduces basic concepts considered by chemists who study the interaction of light with matter and provides some examples from recent literature for the more demanding audiences. This content is followed by background strictly relevant to the experimental section which establishes *state-of-the-art* of the use of 4th group transition metals in photochemistry.

2.1 Introduction to interactions of light and matter

As established by James C. Maxwell, electromagnetic radiation is an oscillation of the electric and magnetic fields, in other words waves.[7] This 'classical' definition is often adopted in context of classical physics which can be used for e.g. interpretation of diffraction patterns generated by a grating (Figure 3).[8] However, electromagnetic radiation has an alternative and worse yet, equivalent definition in modern physics, wherein it is described to consist of photons, elementary particles with null invariant mass.[9] The latter definition is supported by e.g. the observation of the photoelectric effect by Albert Einstein.[10]

The schismatic nature of the two definitions has its own term, 'wave-particle duality'[11] and is the first of many peculiarities we shall discuss in this thesis. Therefore, the terms 'wave' and 'photon' are both used when referring to electromagnetic radiation throughout the thesis.

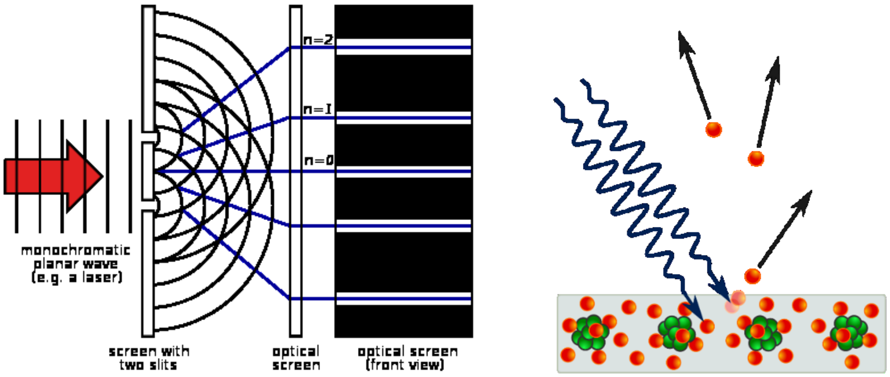

Figure 3: (Left) illustration of diffraction of light on two slits (right) illustration of the photoelectric effect. Reprinted from (left) Wikimedia Commons, 2007, (right) Wikimedia Commons 2020 under Creative Commons Attribution-Share Alike 4.0 International

2.1.1 Energy of the electromagnetic spectrum

Energy E of an electromagnetic wave rises linearly with its frequency v and decreases linearly with its wavelength λ. The slope of the linear dependency is the Planck constant $h = 6.626 \times 10^{-34}$ m^2 kg s^{-1}.[8, 12]

$$E = hv = \frac{hc}{\lambda} \qquad \text{(Equation 1)}$$

Energy of electromagnetic waves is oft interpreted as a spectrum of energy, frequency or wavelength: the electromagnetic spectrum (Figure 4). It is helpful to classify the spectrum by characteristic interactions with matter and in particular molecules,[13] as (in order of decreasing energy and increasing wavelength): gamma radiation (induces atomic core transitions), X-rays (induce core electron transitions), ultraviolet radiation and visible radiation (induce valence electron transitions), infrared radiation (induces vibrational transitions), microwave radiation (induces rotational transitions) and radio waves (induce spin transitions in external magnetic fields).

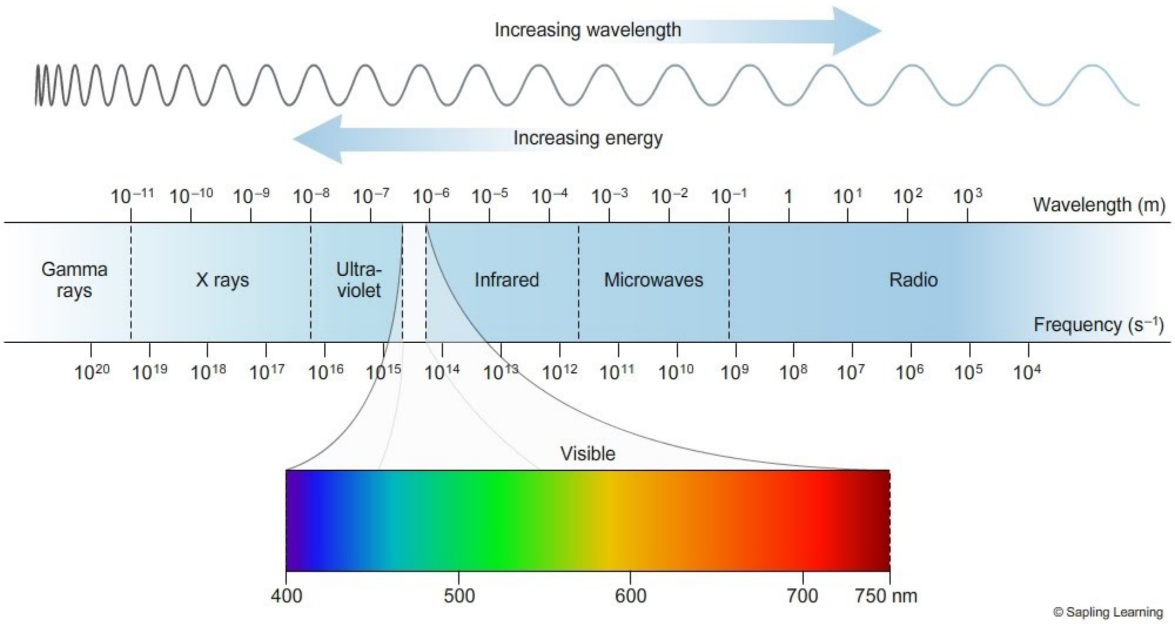

Figure 4: A depiction of the electromagnetic spectrum, illustrating the relationship between wavelength, energy, frequency, and classification of the regions of electromagnetic spectrum. Reprinted from *EM spectrum*, by Macmillan Learning, 2008. Copyright 2008 by Sapling Learning.

2.2 Electronic transitions

This thesis will focus from hereon on the electronic transitions, which are typically induced by ultra-violet and visible light. As illustrated in the previous discussion, electronic transitions cannot be fully decoupled from vibrational transitions. Jablonski diagrams are often used to depict electronic transitions and their relationship to vibrational transitions, which should adequately illustrate the relative separation of vibrational states to the electronic states (Figure 5). In this subchapter, we shall explore the processes depicted in the diagram.

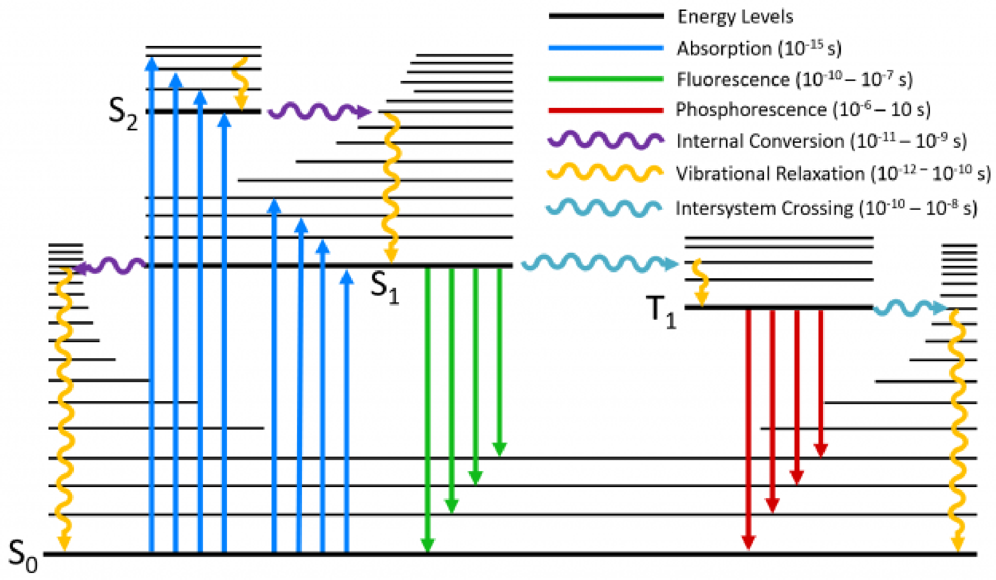

Figure 5: A Jablonski diagram of a singlet ground-state molecule. Legend is included in the figure. Copyright Edinbrugh Instruments.

2.2.1 Absorption of a photon and what follows thereafter

Upon irradiation of a sample, its molecules will absorb a photon with a certain probability.[12] This process occurs typically on a timescale of 10^{-15} s. Absorption of a photon induces a transition between two states of potential energy (for the purposes of this work of an atom or a molecule), under the condition that the photon has the exact energy of their separation (Figure 6). It is of note that this description does not hold in special cases, such as two-photon absorption, in which the molecule/atom absorbs two photons simultaneously.[14]

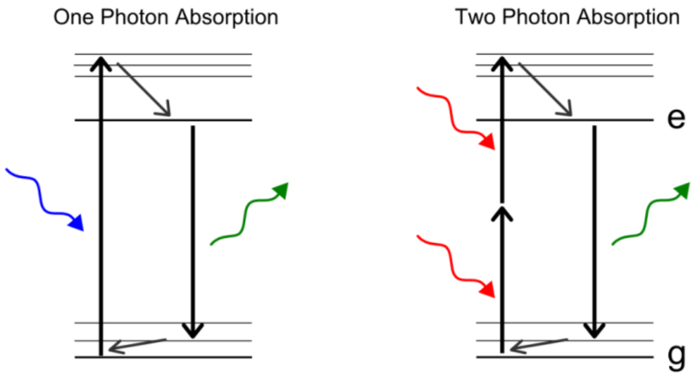

Figure 6: Schematic depiction of one- and two-photon absorption. **Thick** horizontal lines symbolize the electronic states (g for ground, e for excited). Narrow horizontal lines symbolize vibrationally excited states. Incoming photons are depicted as blue and red wavy arrows. Green wavy arrow depicts an emitted photon. Thick vertical arrows depict electronic transitions and thin arrows vibrational relaxation. Reprinted.[15]

Given the above information alone, one may expect e.g. measured absorption and emission spectra to be discrete. However, as will be demonstrated in the following examples, this is not the case. Due to the aforementioned hierarchy of the induced transitions, viability of lower-hierarchy transition results in broadening of the spectra, which is observed spectroscopically. However, commonly applied computational methods used to model electronic transitions, most importantly time-dependent density functional theory (TD-DFT),[16] a method widely applied in the experimental section of this thesis, do not account for the broadening.

Atomic absorption and emission spectra exhibit the most 'discrete' observable transitions, as single atoms lack vibrational and rotational degrees of freedom (Figure 7).[17] Nevertheless, even these transitions are fundamentally broadened by translational motion of individual atoms.

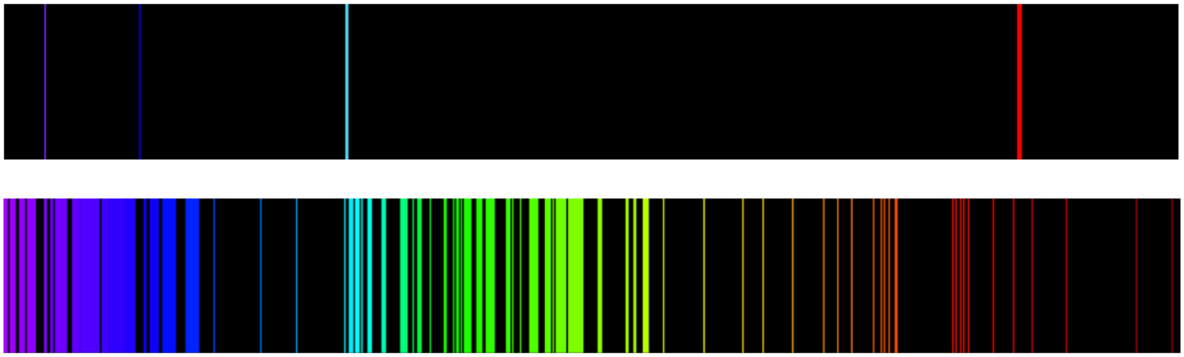

Figure 7: Atomic emission spectra of (top) hydrogen and (bottom) iron in the visible region of the electromagnetic spectrum. Wavelengths are illustrated by colours of emission lines. Figure is reprinted, in public domain.

In electronic spectra of polyatomic species (molecules), the translation broadening is accompanied by the more pervasive rotational and vibrational broadening (Figure 8).[18] Measured absorption spectra typically resemble an envelope of their electronic excited states. If measured in solution, both absorption and emission spectra will experience solvatochromism, further complicating their interpretation.[19]

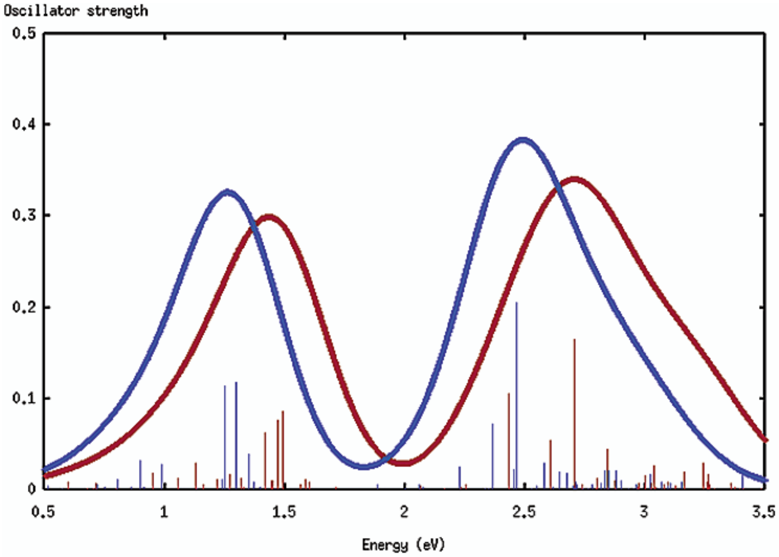

Figure 8: Spectrum of cis-[Ru(4,4‘-COOH-2,2‘-bpy)$_2$(NCS)$_2$] complex, computed *in vacuo* with the BPW91 (red lines) and LB94 (blue lines) XC functionals. Red (blue) vertical lines correspond to the unbroadened excitation energies and oscillator strength computed by the BPW91 (LB94) functional. Reprinted with permission.[20] Copyright 2003 American Chemical Society.

Born-Oppenheimer approximation applies under the conditions of absorption, which states that wavefunctions of electrons and nuclei of atoms/molecules can be treated separately, due to their mass difference (hence, different timescales of motion, see differences in timescales of absorption and vibrational relaxation in Figure 5).[21]

Born-Oppenheimer approximation allows constructing electronic potential energy surfaces (more precisely *N*-dimensional hypersurfaces, where *N* is the number of nuclei in the molecule), which define the potential energy of a system (molecule) by the position of atomic nuclei.[22] The potential energy surface can be also defined by any given internal coordinate of the molecule e.g. bond stretching or dihedral rotation (Figure 9).

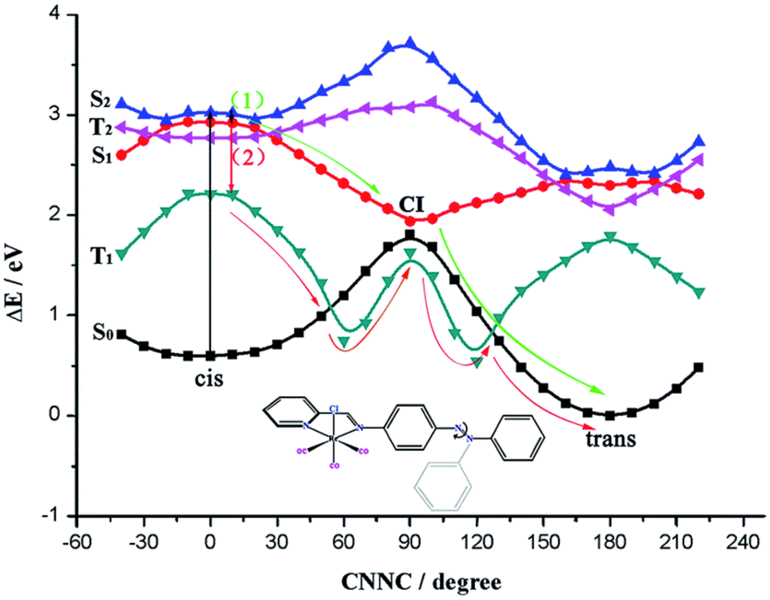

Figure 9: Calculated potential energy profiles (B3LYP/6-311++G(d,p)) in the excited states for $Re(CO)_3$–AB (a diimine ligand with an azo group substituent depicted in the figure) along the $C_5N_1N_2C_3$ rotation coordinate (corresponding to depicted shadow phenyl group). The figure illustrates 1) the different potential energy surface profiles of various excited states, 2) a resulting loss of isomerization energy barrier in states S_1 and T_1, compared to the ground state S_0. Reproduced with permission from the Royal Society of Chemistry.[23]

Topology of a potential energy surface has a direct chemical interpretation.[24] Minima of the potential energy surface correspond to minimal energy geometries of molecules. Vibrational motion results in displacement from the minimal energy geometry, along the slopes of the potential energy surface. Saddle-points of the potential energy surface indicate transition states between two minimal energy geometries, which now define two isomers or reactants and products of a chemical reaction.[24]

From the Born-Oppenheimer approximation, Franck-Condon approximation (discussed in more detail in 2.2.3) approximates electronic transitions as vertical transitions between two potential energy surfaces.[25] Franck-Condon approximation also accounts for simultaneous transitions between vibrationally excited states, which are determined by their overlap integrals.

The geometry thereafter relaxes to minimal energy geometry by vibrational relaxation. It is of note that the different topology of the excited-state potential energy surface may lead to pronounced geometric changes relative to the initial ground state geometry (also illustrated in Figure 8). In some molecules, excited state topologies which strongly deviate from grounds state topologies may manifest as photoisomerization[26] or photofragmentation.[27]

Minima of electronic excited states are meta-stable states. Molecules transition to lower-excited states by internal conversion.[28] The ground state is achieved by radiative or non-radiative transition, typically from the lowest-excited state.[25]

2.2.2 Radiative transition

Radiative transition is a mechanism by which an excited state molecule loses energy by emission of a photon of energy defined by (Equation 1).[29] The emission wavelength and the shape of the emission peak is determined by the topology of the excited-state potential energy surface and may in extreme cases resemble a mirror image of the peak of the first absorption band or *vice versa* be distorted, losing its fine structure (Figure 10).

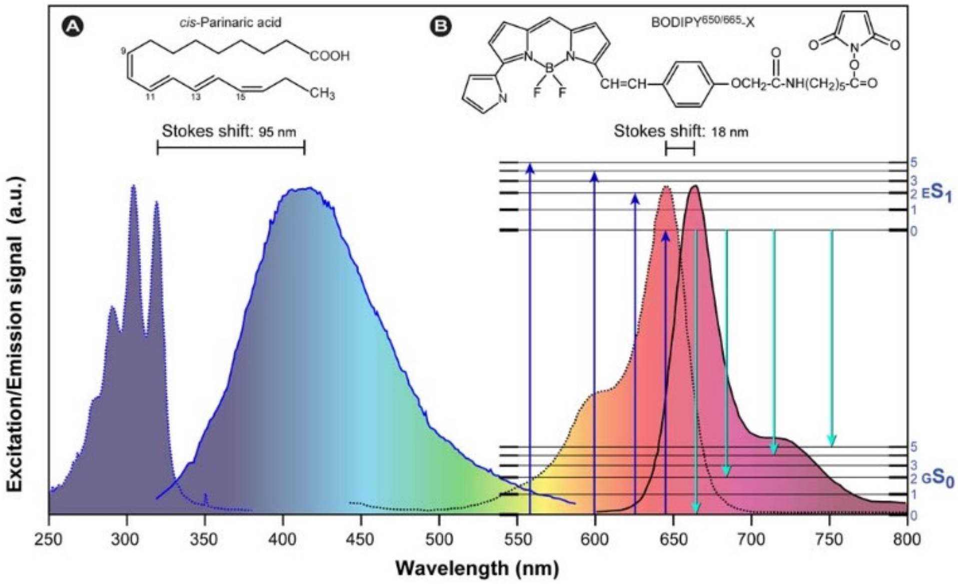

Figure 10: Absorption/excitation and emission spectra of two (A) cis-Parinaric acid and (B) BODIPY$^{650/665\text{-}X}$. Reprinted.[30]

Internal conversion between two excited states is typically more probable than a direct transition to the ground state.[31] Two empirical rules are formulated based on this finding: Kasha's rule and Vavilov's rule. Kasha's rule states that emission occurs from the lowest excited state of a molecule. Vavilov's rule follows up by adding that due to Kasha's rule, emission wavelength is independent of the excitation wavelength (under the condition that absorption occurs).[12, 31]

However, there are numerous examples of molecules that violate the rule, typically due to low internal conversion rate between the first and the second excited state.[31] A text-book example of an anti-Kasha molecule is azulene. However, several organometallic complexes exhibiting anti-Kasha behaviour have been described as well (Figure 11).[32]

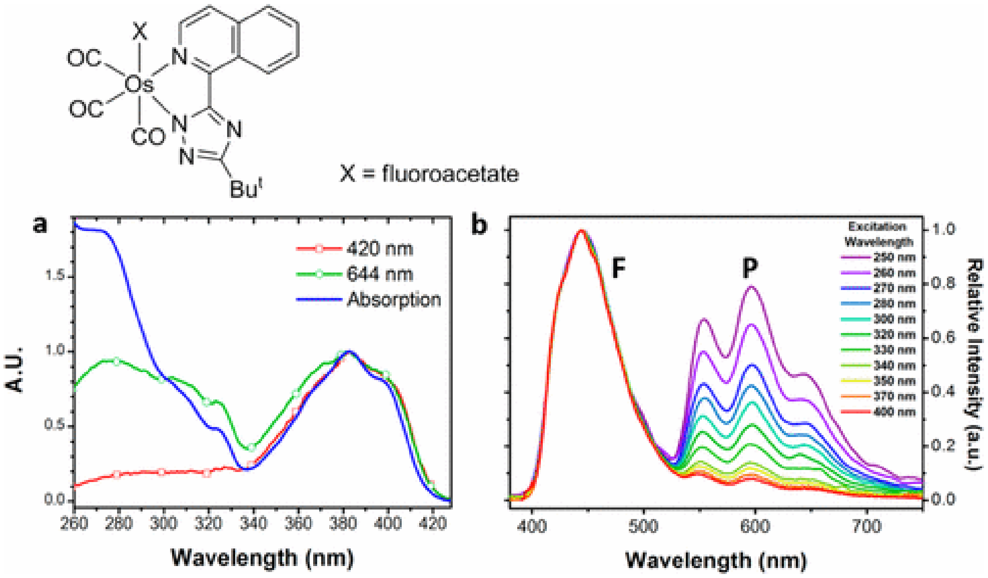

Figure 11: Steady state spectra of Os(II) complex in aerated CH_2Cl_2 at 298 K. (a) Normalized absorption and excitation spectra monitored at different emission wavelengths. The excitation spectrum monitored at 420 nm reveals a deficiency of constitution at short wavelengths as compared to those measured at 644 nm and steady state absorption. (b) Excitation-wavelength-dependent (250–400 nm) emission spectra normalized at the fluorescence peak maxima. The intensity ratio for phosphorescence (P) versus fluorescence (F) increases by about 8 times while tuning λ_{ex} from 400 to 250 nm. Reprinted with permission.[32] Copyright 2017 American Chemical Society.

2.2.3 Forbidden photophysical phenomena

In the quantum mechanical formalism, the probability of an electronic transition is given by the transition dipole moment M, an overlap integral between two states, defined by wavefunctions ψ and ψ' and the operator of the transition dipole moment $\hat{\mu}$. If treated as only electronic wave functions, they can be separated into ψ_{orb} and spin ψ_{spin} wave functions, leading to spin-selection rule and orbital-selection rule (Equation 2).

$$M_{\text{el}} = \langle\psi'|\hat{\mu}|\psi\rangle = \left\langle\psi'_{\text{orb}}\psi'_{\text{spin}}\middle|\hat{\mu}\middle|\psi_{\text{orb}}\psi_{\text{spin}}\right\rangle$$
$$= \left\langle\psi'_{\text{orb}}\middle|\hat{\mu}\middle|\psi_{\text{orb}}\right\rangle\left\langle\psi'_{\text{spin}}\middle|\psi_{\text{spin}}\right\rangle \qquad \text{(Equation 2)}$$

Despite that, the transitions forbidden by these selection rules can be observed, owing to perturbations of the wavefunctions. Perturbing mechanisms may include bimolecular collisions, magnetic interactions, vibrational perturbations, or relativistic perturbations.[33-35] Above that, recent experimental reports suggest novel mechanisms. One of such examples is a unusually high yield of triplet state in an orthogonal BODIPY dimers, which are attributed directly to the geometry of the two moieties as the authors propose it induces symmetry breaking charge-transfer.[36] Photophysically forbidden states can also be achieved by alternative methods of excitation, e.g. by chemical reactions[37] or bimolecular energy-transfer.[38] For the purposes of this thesis, we shall examine vibrational and relativistic perturbations, as these are relevant to the experimental section.

2.2.3.1 Vibrational perturbations

Molecular vibrations alter the coordinates of atomic nuclei, which may lead to a change of the molecule's symmetry and by extension, its orbital symmetry.[39] Such perturbation allows parity-forbidden electron transitions.

Under the Franck-Condon approximation (2.2.1), the wavefunction can be separated into vibrational ψ_{vib}, orbital ψ_{orb} and spin ψ_{spin} wave functions, which now account for transitions between vibrational levels of the two electronic states (Equation 3). The first term of (Equation 3) is also called the Franck-Condon (FC) factor.[25]

$$M_{\text{FC}} = \langle\psi'|\hat{\mu}|\psi\rangle = \left\langle\psi'_{\text{vib}}\psi'_{\text{orb}}\psi'_{\text{spin}}\middle|\hat{\mu}\middle|\psi_{\text{vib}}\psi_{\text{orb}}\psi_{\text{spin}}\right\rangle$$
$$= \left\langle\psi'_{\text{vib}}\middle|\psi_{\text{vib}}\right\rangle\left\langle\psi'_{\text{orb}}\middle|\hat{\mu}\middle|\psi_{\text{orb}}\right\rangle\left\langle\psi'_{\text{spin}}\middle|\psi_{\text{spin}}\right\rangle \qquad \text{(Equation 3)}$$

However, this Franck-Condon approximation does not account for the perturbation caused by the molecular vibration. Instead, it merely modulates the transitions to correspond to the overlap of vibrational wavefunctions. Hence, it is often referred to as the 'clamped nuclei model'.[39] Treatment of vibronic perturbations requires appending the Franck-Condon approximation by the Herzberg-Teller approximation.

Herzberg-Teller approximation is constructed as a first-order perturbation to the Franck-Condon approximation by accounting for the dependency of the transition moment on the j nuclear coordinates Q_j (Equation 4).[39] This dependency is experimentally well established and dubbed as 'Hertzberg-Teller effect'. It most notably manifests as intensity borrowing by symmetry-forbidden transitions.

$$M_{\text{FC-HT}} = M_{\text{FC}} + \sum_j \left(\frac{\partial M_{\text{FC}}}{\partial Q_j} \right) \qquad \text{(Equation 4)}$$

However, transition moments of any electronic transition may experience the Herzberg-Teller effect, including both allowed and forbidden transitions.[40] By their incorporation, impressively accurate simulations of electronic spectra can be performed (Figure 12).

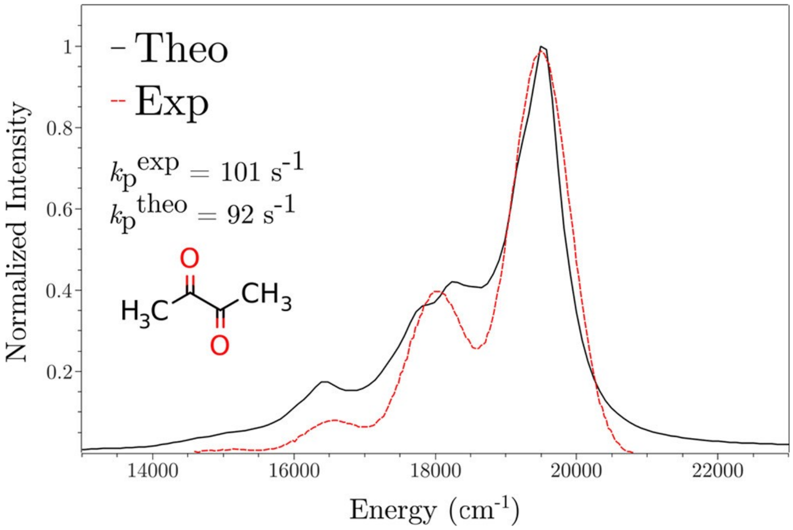

Figure 12: Predicted phosphorescence spectrum and rate for biacetyl in ethanol. The theoretical curve was blue-shifted by 2880 cm^{-1} to match the experimental 0–0 transition energy. Reprinted with permission from.[40] Copyright 2019 American Chemical Society.

An illustrative example of the Herzberg-Teller effect can be found in the simulation of electronic absorption spectra of $[PtCl_4]^{2-}$, in which transition dipole moment of *d*-*d* transitions is null under the Franck-Condon approximation (Figure 13).[39]

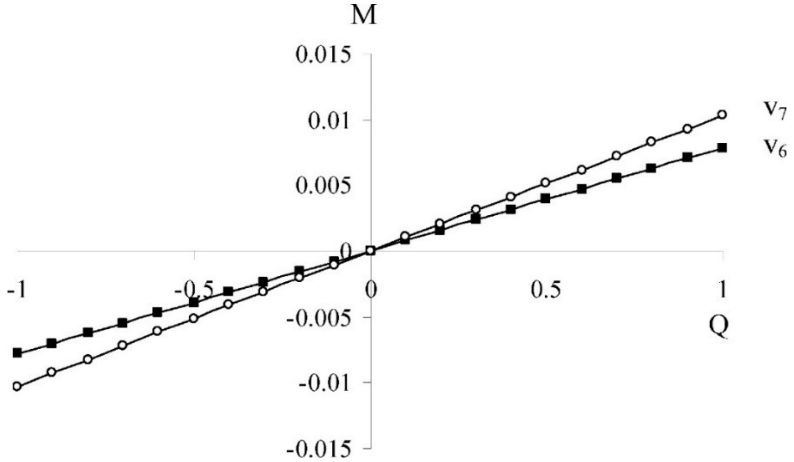

Figure 13: Calculated transition moment of $^1A_{2g} \leftarrow {}^1A_{1g}$ of $[PtCl_4]^{2-}$ as a function of displacement along the e_u modes (v_6, v_7). Reprinted with permission.[39] Copyright 2008 American Chemical Society.

2.2.3.2 Perturbation by spin-orbit coupling

Spin-orbit coupling (SOC) refers to an interaction of electron's spin with its own motion in the electric field (characterized by orbital momentum).[35] The coupling manifests as mixing of spin- and orbital- momenta. Using a model of a singlet ground state molecule, SOC results in mixing of wavefunctions of the singlet states ψ_{S_n} with wavefunctions of the triplet states ψ_{T_m}, yielding a perturbed triplet state $\widetilde{\psi}_{\mathrm{T}_m}$ (Equation 5).[35]

$$\widetilde{\psi}_{\mathrm{T}_m} = \psi_{\mathrm{T}_m} + \sum_n \delta_n \psi_{\mathrm{S}_n} \qquad \text{(Equation 5)}$$

The mixing is governed by the admixture coefficient δ_{n} (Equation 6), derived from the first-order perturbation theory formalism. Its evaluation requires solving the spin-orbit Hamiltonian $\widehat{H}_{\mathrm{SO}}$ (which in this formalism perturbs the unperturbed Hamiltonian).[35]

$$\delta_n = \frac{\left\langle \psi_{\mathrm{S}_n} \middle| \widehat{H}_{\mathrm{SO}} \middle| \psi_{\mathrm{T}_m} \right\rangle}{E(\mathrm{T}_m)\text{-}E(\mathrm{S}_\mathrm{n})} \qquad \text{(Equation 6)}$$

One of the commonly applied $\widehat{H}_{\mathrm{SO}}$ is the Breit-Pauli many-electron SOC Hamiltonian $\widehat{H}_{\text{B-P}}$ (Equation 7), which includes one-electron interaction of spin s and orbital l momenta of an electron i with a nuclei A and two-electron (i, j) interactions. This notation directly relates the SOC to atomic mass Z, as opposed to e.g. Russel-Saunders scheme.[35]

$$\widehat{H}_{\text{B-P}}=\alpha^2 \sum_A \sum_i \frac{Z_A}{r_{Ai}^3} \vec{l}_{Ai} \vec{s}_i - \sum_A \sum_{i \neq j} \frac{1}{r_{Ai}^3} \vec{\mathrm{l}}_{ij} (\vec{\mathrm{s}}_i + 2\vec{\mathrm{s}}_j) \qquad \text{(Equation 7)}$$

A common interpretation in literature is that the spin and orbital quantum numbers become 'bad' quantum numbers in presence of strong SOC. As a result, spin-forbidden transitions become 'allowed' by SOC, including radiative (e.g. singlet-triplet transitions) and non-radiative (intersystem crossing) transitions.[35]

2.3 Interaction of excited-state molecule with its surroundings

Last subchapter illustrated that excited molecules are carriers of energy which can induce emission and monomolecular non-radiative transformations. In this chapter, we shall cover intermolecular interactions of excited state molecules.

Excited-state molecules may exchange energy with their surroundings by molecular collisions, by emission and subsequent reabsorption and by energy-transfer mechanisms. Excited states may also induce chemical reactions and electron-transfer processes.[12]

2.3.1 Excited-state energy-transfer

Mechanisms of bimolecular charge-transfer can be associated with formation of an excimer, exciplex or a collision complex. Excimers and exciplexes are a well-defined chemical species which correspond to minima on their respective potential energy surface.[41] 'Excimer' refers typically to a homodimer, whereas 'exciplex' refers exclusively to heterodimer. In contrast, collision complexes form by chaotic collisions of molecules and must be modelled statistically.[42] Upon formation, these species can lose energy radiatively, non-radiatively or by energy-transfer between the two molecules.

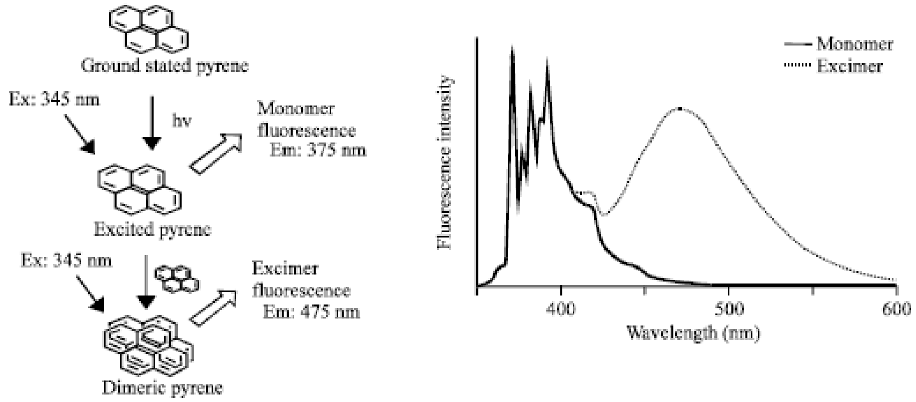

Figure 14: (Left) Illustration of excimer formation of pyrene and (right) impact of excimer formation on the measured emission spectra. Reprinted.[43]

Excited-state energy-transfer is facilitated by two mechanisms, Förster mechanism and Dexter mechanism (Figure 15).[44] Förster mechanism is characterized as a long-range dipole-dipole interaction and requires overlap of the emission spectrum of the donor with absorption spectrum of the acceptor. Dexter mechanism proceeds by a short-range electron exchange and is limited by overlap of the electron wave-functions of donor and acceptor.[45] Both mechanisms are not limited by the selection rules defined for photoinduced transitions, but rather the Wigner-Witmer rule.

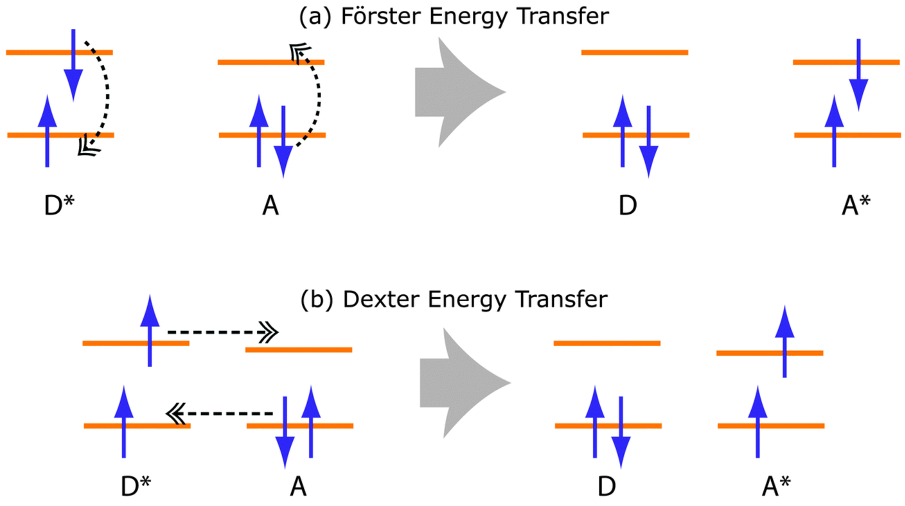

Figure 15: (a) Förster energy-transfer. (b) Dexter energy-transfer. The horizontal lines are HOMO and LUMO energy levels of donor (D) and acceptor (A) molecules; the asterisk denotes excited state. The dashed arrows represent simultaneous rearrangement of the electronic configuration. Reproduced with permission from the Royal Society of Chemistry.[44]

2.3.2 Photosensitization of singlet oxygen

Photosensitization of singlet oxygen is a heavily covered topic in scientific literature for its applications in medicine,[46] material chemistry[47] and chemical synthesis.[48] Ground state of singlet oxygen has two unpaired electrons and thus, is a triplet state. Its two singlet excited states, $^1\Delta_g$ a $^1\Sigma_g$, can be reached by a spin-forbidden electron transition.

Direct photoexcitation of oxygen results in low yields of the singlet states under laboratory conditions. Singlet oxygen can be prepared stoichiometrically by the reaction of hydrogen peroxide with sodium hypochlorite (Figure 16).[48] However, the preferred method (and more economical method) of singlet oxygen generation is photosensitization (energy-transfer from excited states of excited-state donors to the molecule of oxygen).

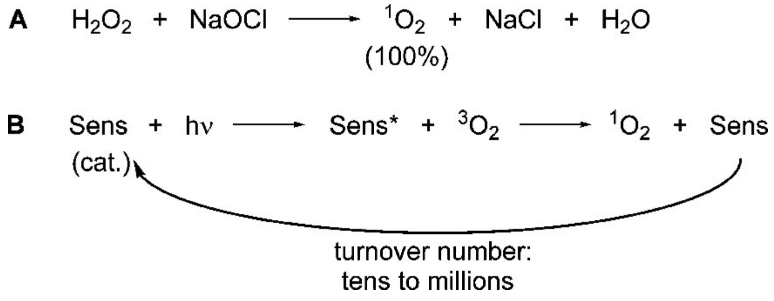

Figure 16: Generation of Singlet Oxygen (A) by reaction of hydrogen peroxide with sodium hypochlorite, (B) by photosensitization. Reprinted with permissions.[48] Copyright 2016 American Chemical Society.

Singlet oxygen can be photosensitized by both singlet and triplet state photosensitizers, although triplet photosensitizers are more common in literature, as the charge-transfer is preferred by the Wigner-Witmer rule (singlet oxygen sensitization is typically facilitated by Dexter mechanism).[33] Typical singlet-oxygen photosensitizers include porphyrines, phtalocyanines, various complexes of Ru(II), Os(II) and Ir(III), and organic dyes.

Singlet oxygen is a highly reactive specie. It can be utilized in photodynamic therapy to induce cell-death, which may be applied to treat various tumours, but has also been researched for treatment of fungal infections, dental infections and mammalian viruses.[49] Singlet oxygen photosensitization is applied in self-cleaning surface coatings based on TiO_2 nanoparticles.[50] Singlet oxygen is also used as a reagent in chemical synthesis.[48] Examples of reactions of singlet oxygen include photooxygenation, which is a cycloaddition reaction of the oxygen molecule with a double bound which yields endoperoxides, and 'eneone' (also Schenk) reaction, which is an allylic oxidation by singlet oxygen (Figure 17). Singlet oxygen also reacts with inorganic substrates, such as phosphorous or sulphur.[48]

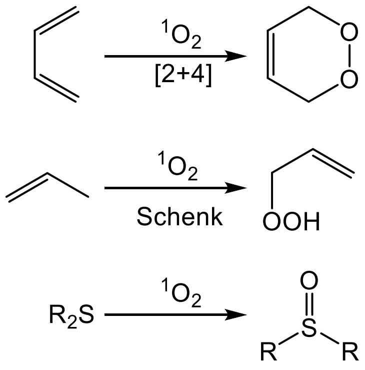

Figure 17: Reactions of singlet oxygen. From the top, [2+4] cycloaddition of singlet oxygen onto 1,3-butadiene, 'eneone' reaction with propylene and oxidation of a secondary thiol.[48]

2.3.3 Excited-state electron-transfer (photoredox reactions)

Photoredox reactions are redox reactions in which electron is transferred from or into a molecule in its excited state.[51] Although redox reactions are certainly not limited to excited-state molecules, electron excitation promotes redox reactions. Electron is excited from HOMO into a higher-energy LUMO and consequentially, less energy is required to remove the excited electron from its orbital. *Vice versa*, electron excitation results in a ‘hole’ in the HOMO and thus, less energy is required to insert an electron into the orbital.[51]

The principle is illustrated in an example of $[Ru(bpy)_3]^{2+}$ (Figure 18). Upon excitation, the reduction potential of redox pair $[Ru(bpy)_3]^{3+}/[Ru(bpy)_3]^{2+}$ (vs. SCE at 22 °C) shifts from 1.29 V to −0.81 V and *vice versa*, the reduction potential of redox pair $[Ru(bpy)_3]^{2+}/[Ru(bpy)\ ]^{3+}$ shifts from −1.33 V to 0.77 V.[52]

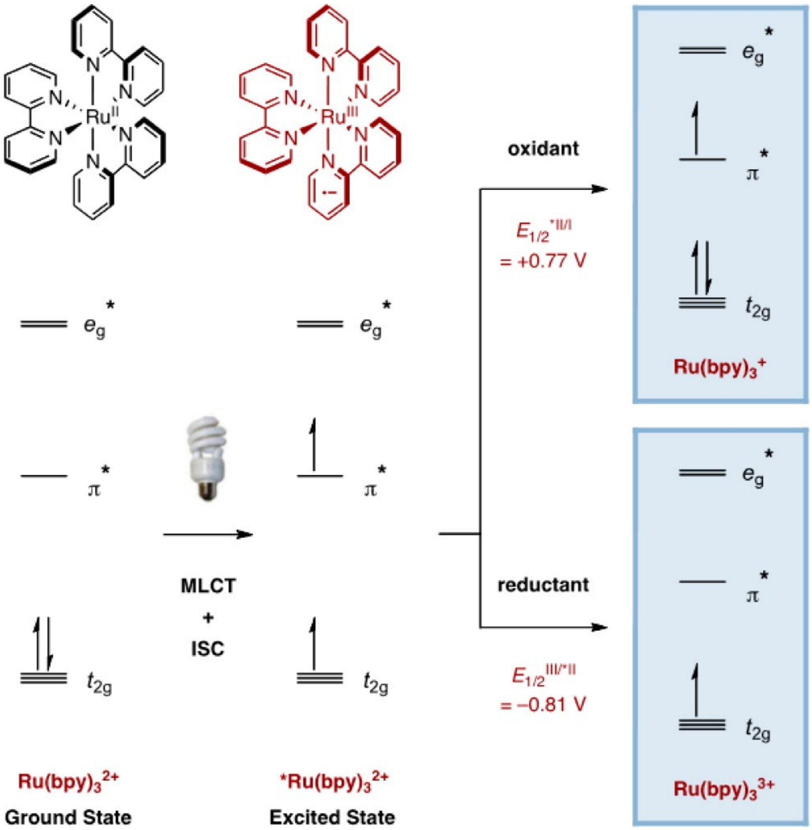

Figure 18: Simplified molecular orbital depiction of $[Ru(bpy)_3]^{2+}$ photochemistry. Reprinted with permission.[51] Copyright 2013 American Chemical Society.

2.3.4 Photoredox catalysis

Photoredox catalysis applies the enhanced oxidation and reduction of excited-state molecules in catalytic electron-transfer reactions.[51] In a typical photoredox mechanism, catalytic species, a redox photocatalyst (alternatively photoredox catalyst) is first excited, upon which it may be oxidatively or reductively quenched to yield a reduced or oxidized catalytic species, which reacts with a substrate to yield a product and recover the ground state catalyst in its former oxidation state (Figure 19).[51]

Both organic and inorganic photocatalysts have been widely reported in photoredox catalysis.[51, 53] One of the most thoroughly investigated organic photoredox catalysts is the xanthene dye eosin Y. Eosin Y was observed to be queneched both oxidatively and reductively. An illustrative example of perfluoroarylation of aryls photocatalysed by eosin Y is given in Figure 20.[54] Figure 21 depicts the proposed mechanism of the reaction, suggesting an interplay of both the oxidative and reductive quenching cycles.

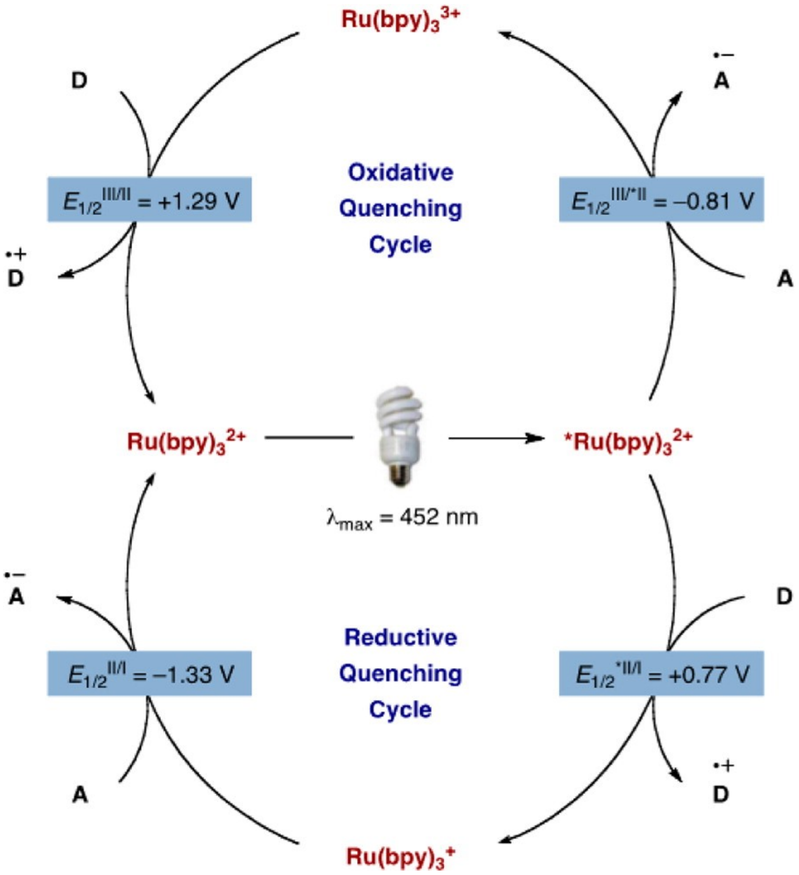

Figure 19: Oxidative and reductive quenching cycle of $[Ru(bpy)_3]^{2+}$. Reprinted with permission.[51] Copyright 2013 American Chemical Society.

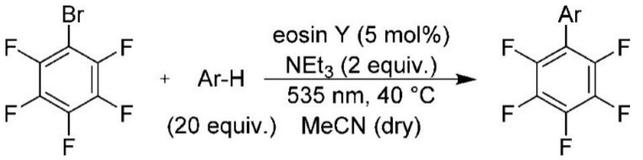

Figure 20: Perfluoroarylation of aryls photocatalyzed by eosin Y. Reprinted with permission from.[54] Copyright 2016 American Chemical Society.

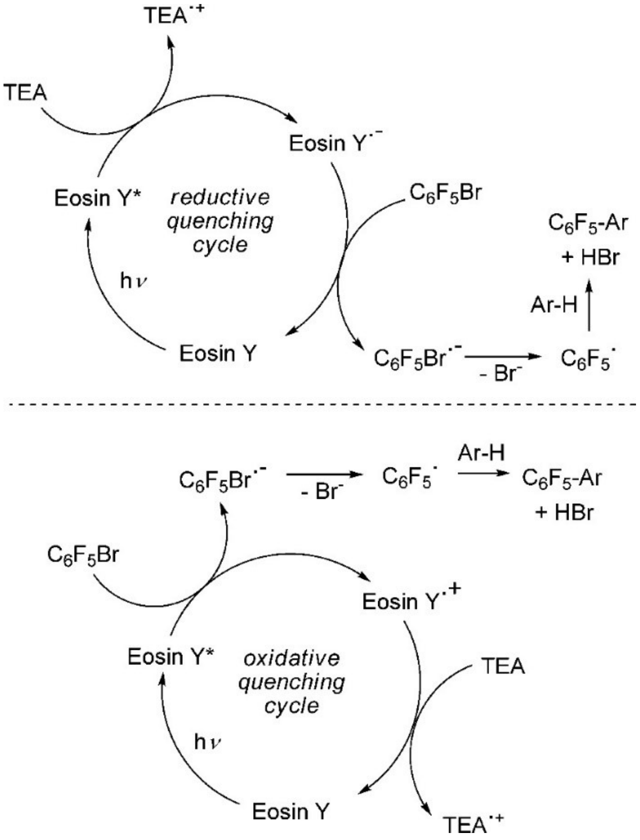

Figure 21: Proposed mechanisms of perfluoroarylation of aryls, suggesting an interplay of both reductive and oxidative quenching cycles of eosin Y. Reprinted with permission.[54] Copyright 2016 American Chemical Society.

Photoredox catalytic mechanisms which involve multiple catalytic cycles have been reported.[51, 53, 55] Two-component cascade cycles are the most common, typically featuring a photocatalytic cycle which initiates the ground state catalytic cycle which in turn transforms the substrate. However, more complex schemes do exist. A recent example of such mechanism is an interplay of $[Ir(dtbbpy)(ppy)_2]PF_6$ photocatalyst and $Co(dmgH)_2(DMAP)Cl$ cobaloxime ground-state catalyst (Figure 22), which were reported in a novel dehydrogenative strategy for synthesis of variously functionalized anilines, using cyclohexanones and secondary amines as reactants (Figure 23).[56]

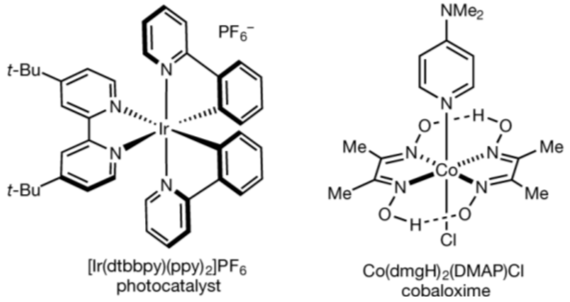

Figure 22: Molecular structures of $[Ir(dtbbpy)(ppy)_2]PF_6$ and $Co(dmgH)_2(DMAP)Cl$, used in dehydrogenative synthesis of anilines. Reprinted.[56]

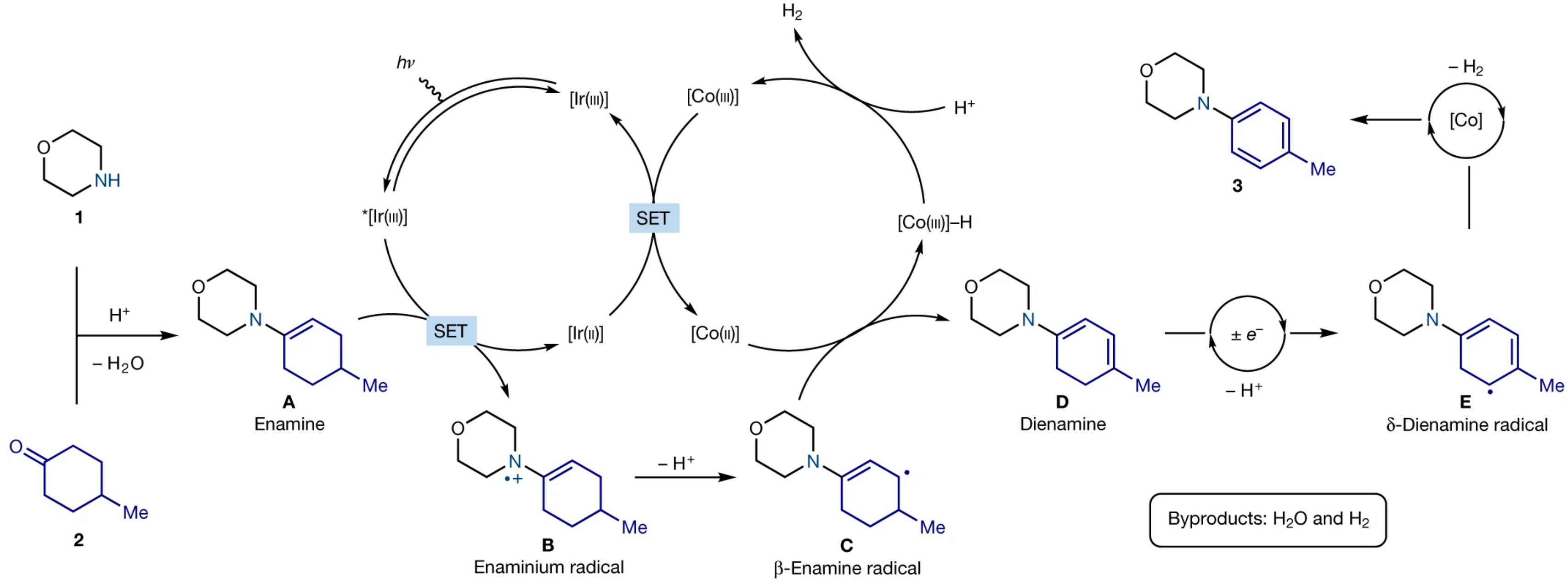

Figure 23: Proposed mechanism for the dual photoredox-cobalt dehydrogenative coupling between amine **1** and cyclohexanone **2**. Reprinted.[56]

Interestingly, some photocatalytic cycles (including those of perylene diimides and Rhodamine 6G) involve excitation of the already quenched photocatalytic species, a so called consecutive photoinduced electron-transfer mechanism.[57] This mechanism was first observed in perylene diimides. *N*,*N*-bis(2,6-diisopropylphenyl)perylene-3,4,9,10-bis(dicarboximide) (PDI, Figure 24) was reported to photocatalyze reduction of arylhalides and reductive coupling of aryl halides by conPET mechanism (Figure 25, Figure 26).[58]

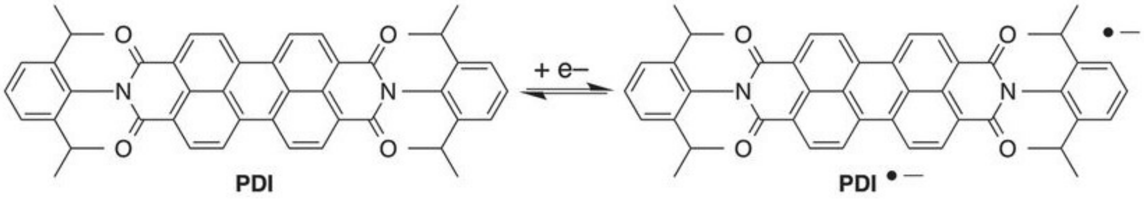

Figure 24: A depiction of PDI and its one-electron reduction. Reprinted.[54]

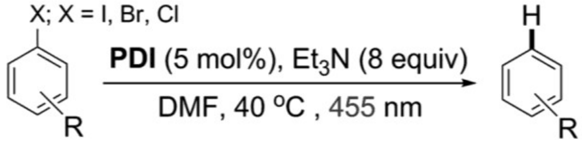

Figure 25: Reduction of arylhalides photocatalyzed by PDI. Reprinted.[54]

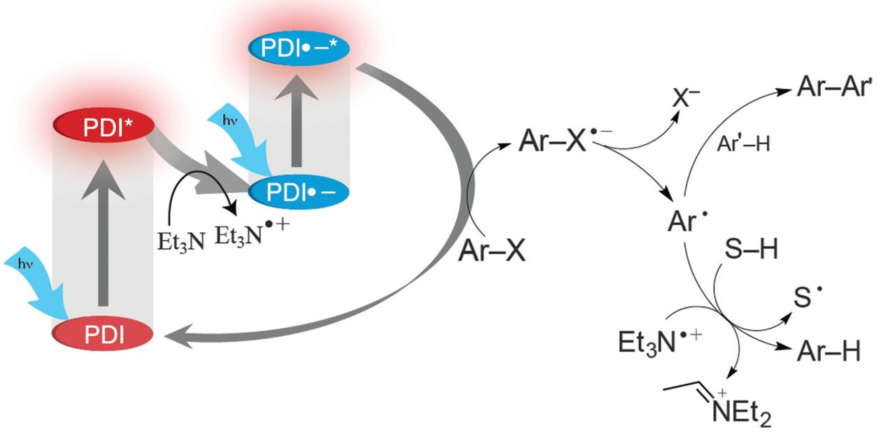

Figure 26: Proposed conPET mechanism of reduction of arylhalides and reductive coupling of arylhalides photocatalyzed by PDI. The scheme illustrates the colour change of PDI upon reduction (red → blue). Reprinted.[54]

2.4 Photoluminescence of transition metals complexes

Photoluminescent transition metal complexes have been extensively applied in (bio)imaging technologies.[59-62] Their long-lived excited states can also be utilized in photovoltaics,[63-64] photodynamic therapy[65] and photoredox catalysis.[51, 55] These complexes typically feature an electron rich central atom (Ru, Ir, Pt, Au but also Cu and Mn) in a low oxidation state and π-acceptor ligands (e.g. polypyridyl), which allow efficient metal-ligand charge-transfer (MLCT) transitions. Heavier transition metals feature more prominent spin-forbidden transitions induced by scalar-relativistic spin-orbit coupling.[66] Many of these complexes have been used in the construction of organic light-emitting diodes (OLED) (Figure 27). However, some of the lighter metal complexes may feature other interesting photophysical mechanisms, notably complexes thermally delayed fluorescence.[67]

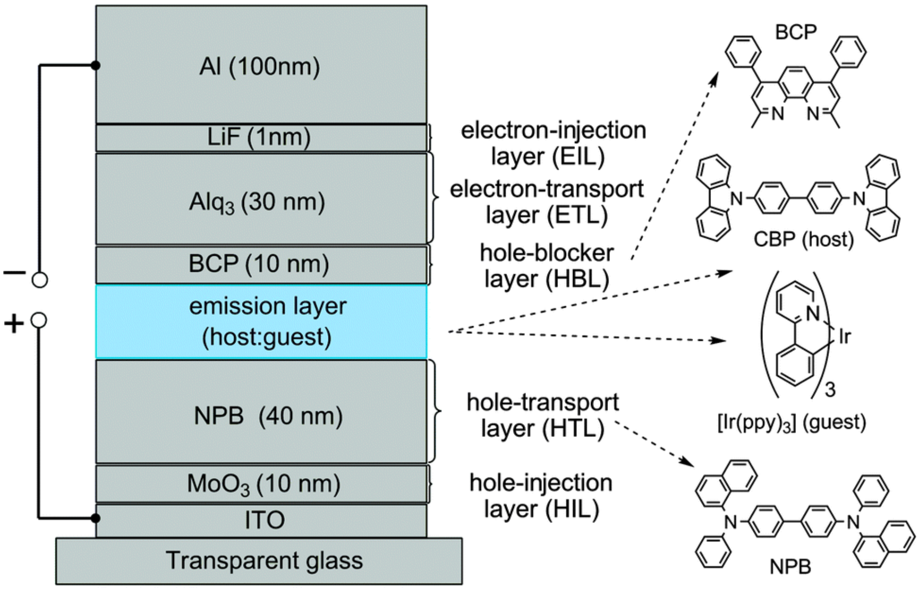

Figure 27: Principle scheme of an OLED device. Reprinted.[66]

2.4.1 Photoluminescent group 4 transition metal complexes

Group 4 metal complexes are most commonly found in oxidation state IV, corresponding to a d^0 electron configuration.[18] The central atoms are therefore electron poor, hard Lewis acids, which are rendered incapable of *d-d* transitions and strongly disfavour MLCT transitions. Thus, UV-VIS absorption spectra of group 4 transition metal complexes are dominated by ligand-metal charge transfer (LMCT) transitions, ligand-ligand charge-transfer transitions (LLCT) and ligand-centred (LC) transitions. Photoluminescence of group 4 transition metal complexes remains poorly described compared to e.g. late transition metal complexes, with only a handful of examples in literature, some of which are introduced herein.

2,6-bis(pyrroryl)pyridine (PDP) zirconium complexes are a recently studied group of complexes which were found to be photoluminescent (Figure 28).[68] The prepared complexes were used in photoredox catalysis of multiple model reactions. Their luminescence is attributed to their ^{3}LMCT states.[69] Analogous mesitylene substituted complexes exhibit thermally activated delayed fluorescence.[69]

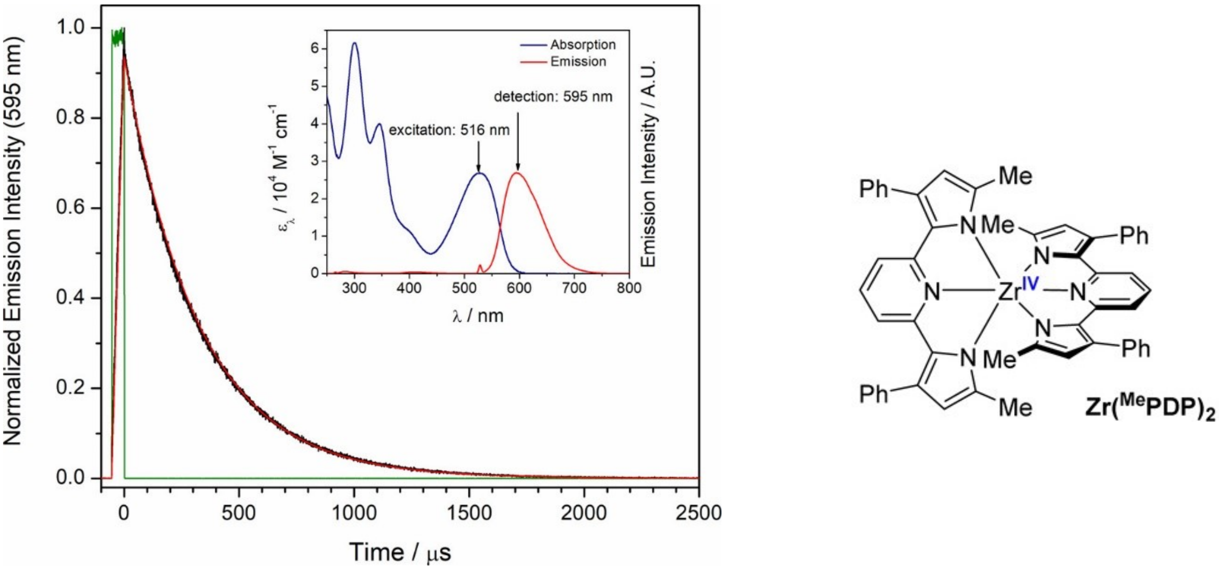

Figure 28: (Left) Time-resolved emission data for Zr(^{Me}PDP)$_2$ (^{Me}PDP = 2,6-bis(5-methyl-3-phenyl-1H-pyrrol-2-yl)pyridine) in THF at room temperature (black line) detected at 595 nm upon excitation at 516 nm (see inset). The red line shows the fit to a single-exponential decay with τ_0 = 325 μs and the green trace shows the excitation pulse (516 nm). (Right) Structure of Zr(^{Me}PDP)$_2$. Reprinted.[68]

Among other notable examples are tetra(8-chinolinolate) complexes of zirconium and hafnium which were used as a dopants in organic light-emitting diodes (OLED).[70] The study included a comparison of the constructed zirconium and hafnium-based OLED's with commonly used aluminium based OLED's. The novel designs resulted in higher quantum efficiency and lower working voltage compared to the control device. A later study was also conducted, probing analogous phenanthroline complexes of zirconium.[71]

2.4.2 Photoluminescence of group 4 metallocene-type complexes

Bis(cyclopentadienyl) early transition metal complexes (Cp_2MX_2) and related complexes (Figure 29), commonly referred to as metallocene-type complexes, metallocene derivatives or simply metallocenes (e.g. titanocene dichloride) may be generously described as a mere curiosity in photoluminescence research.

2.4.2.1 Photoluminescence of titanocene complexes

The first studied group 4 metallocene complexes were titanocene dihalogenides.[72] The studies were conducted at 77 K in glass matrices. Such conditions strongly inhibit non-radiative transitions and thus, intense emission can be experimentally observed, with a lifetime of 10^2–10^3 μs, in the red region of the electromagnetic spectrum (emission max. of Cp_2TiCl_2 at 672 nm). Both the halogenide ligands and the substituents of the cyclopentadienyl ligands modulated the electronic transitions. Luminescence was attributed to triplet excited states based on the experimental findings. Analogous luminescence of $Cp_2Ti(NCS)_2$ was also observed by the same group.[73] DFT calculations and time-resolved vibrational spectroscopy confirmed that the emission corresponds to ^{3}LMCT transitions from the π-bonding orbitals of cyclopentadienyl ligands to the central atom.

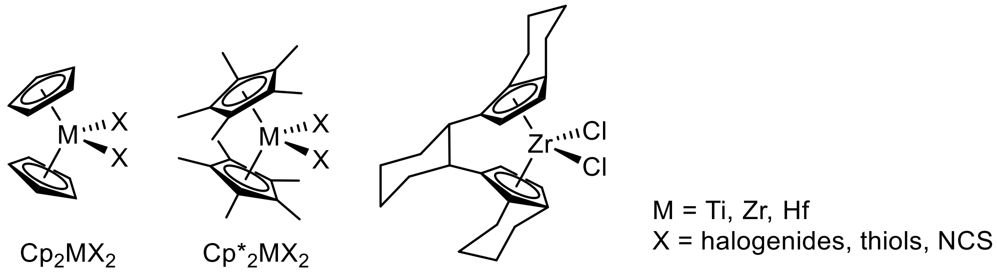

Figure 29: Molecular schemes of studied (from left) bent metallocene complexes, pentamethylcyclopentadienyl complexes and the ansa-bridged metallocene complex.

2.4.2.2 Photoluminescence of zirconocene and hafnocene complexes

Luminescence of second and third row group 4 metallocene derivatives was first reported in metallocene thiolates $Cp'_2M(SR)_2$ ($Cp' = C_5H_5, C_5Me_5$; M = Zr, Hf).[74-76]

A later study compares dihalogenides of all group 4 metals, which found that luminescence quantum yields of Zr a Hf metallocene dihalides is one order higher than of corresponding Ti complexes.[77] As a result, solid state luminescence of Zr a Hf metallocene dihalides could be observed at room temperature.

The finding that heavier central metals result in higher quantum yields (attributed to higher spin-orbit coupling) motivated the authors to further optimize the molecular structure.[78] As a result, a study was conducted on an ansa-bridged zirconocene complex (Figure 29). Although the cyclopentadienyl substituents appear quite flexible, it was found that even the limited restriction of vibrational motion by the ansa-bridge increases the quantum yield significantly (41% in 1,2-dichloromethane solution at 20 °C).

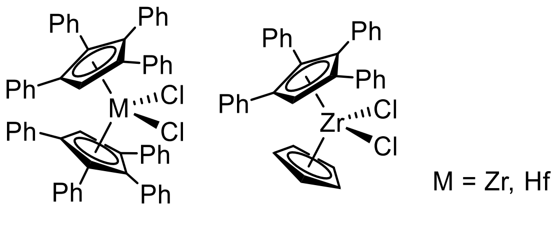

Figure 30: The studied tetraphenylcyclopentadienyl complexes.

Similarly, another group aimed to achieve the same result without bridging cyclopentadienyl ligands. Instead, they opted to restrict the vibrational motion by substituting one or both cyclopentadienyl ligands by four phenyl groups (Figure 30). Although the observed luminescence was less pronounced, at just 2,1 (Zr) and 3,1% (Hf) quantum yields under the experimental conditions, the luminescence is sufficient to be applied in fluorescence microscopy, which was demonstrated in MCF-7 cell cultures (human adenocarcinoma) (Figure 31).[79]

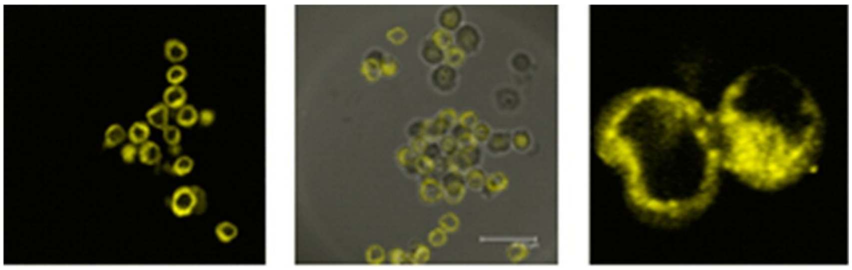

Figure 31: Imaging of MCF-7 human adenocarcenoma cells by $(C_5Ph_4H)CpZrCl_2$.

2.4.2.3 Photoredox catalysis by group 4 metallocene complexes

It was recently reported that bis(cyclopentadienyl)titanium(IV) dichloride (Cp_2TiCl_2) was utilized in photoredox catalysis as a single-electron reductant.[80] Photoexcited states (by green LED, 530 nm) of Cp_2TiCl_2 were shown to be efficiently quenched by *N,N*-diisopropylethylamine (DIPEA), yielding a Ti(III) radical. The reaction was used to facilitate epoxide-opening reactions and 5-exocyclization reactions.[81] It is of note that the reactions utilized a hydrogen-atom-transfer catalyst, methyl thioglycolate. The authors propose that the electron-transfer processes of Ti(IV)/Ti(III) follow an inner-sphere mechanism, as illustrated in Figure 32.

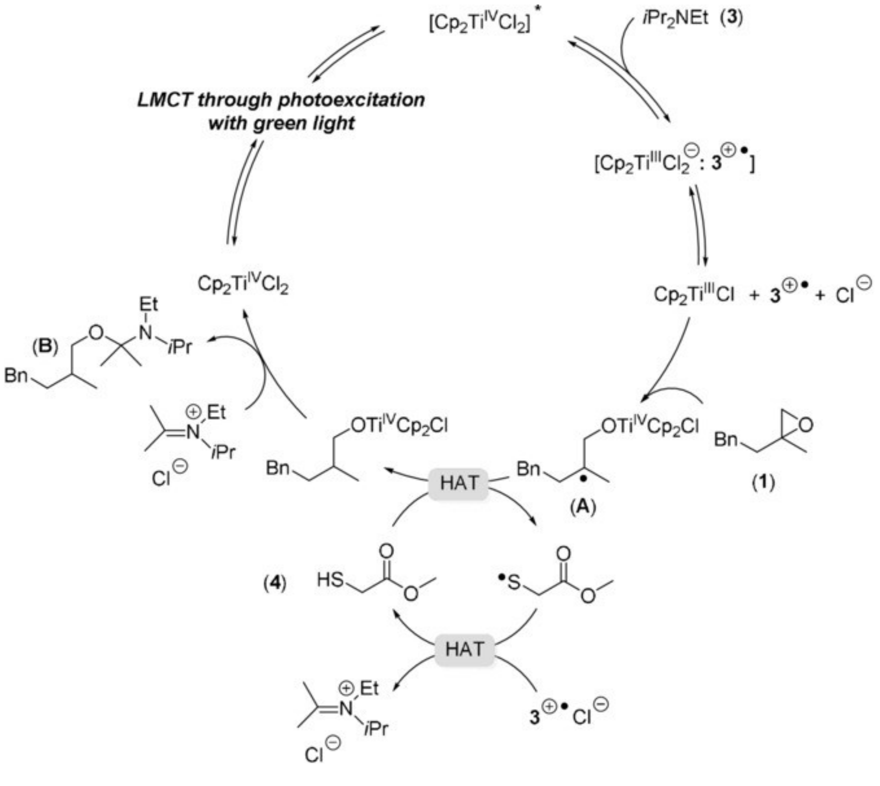

Figure 32: Proposed mechanism for epoxide reduction in the presence of photoexcited Cp_2TiCl_2. Reprinted.[81]

3 Aims of the thesis

The goals of the diploma project discussed herein are: (1) To characterize photophysical properties of previously prepared cationic group 4 metallocene complexes with pendant *N*-donor ligands, (2) to design novel luminescent cationic group 4 metallocene complexes based on the previous findings, (3) to provide a *proof-of-concept* for the use of the prepared complexes in photoredox catalysis.

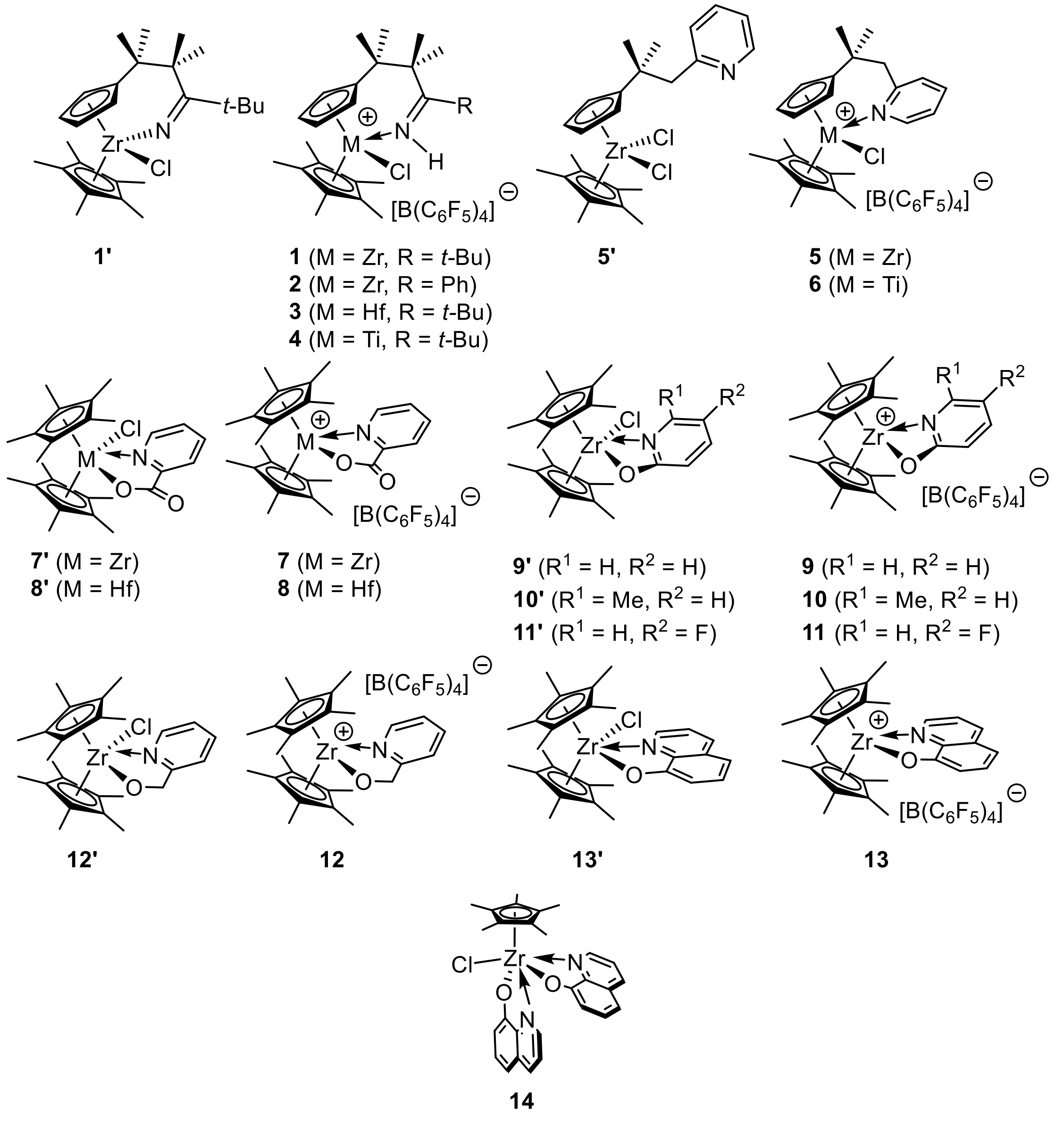

Figure 33: A list of all isolated and characterized products which are studied in the experimental section.

4 Discussion of the results

The discussion of the results is divided into 4 subchapters, 6.1–6.4. Subchapters 6.1–6.3 focus on preparation and characterization of pendant *N*-donor ligand, *N,O*-chelating ligand and 'half-sandwich' *N,O*-chelating ligand complexes, respectively (Figure 33). Subchapter 6.4 shortly discusses the first attempts at photoredox catalysis using some of the prepared compounds, which have been so far limited to a single *proof-of-concept* reaction.

4.1 Metallocene complexes with pendant *N*-donor ligands

The diploma project covered in this thesis has its roots in the works of a previous student, Miloš Večeřa, who prepared numerous metallocene complexes with pendant *N*-donor ligands, some of which are discussed herein (Figure 34). Večeřa left the group before completing the project, which was therefore inherited by the current author.

The complexes were designed to stabilize positive charge upon abstraction of chloride ligand or protonation of their neutral precursors. During their preparation, it was noticed that the cationic complexes exhibit intense, room-temperature luminescence under UV-light (TLC lamp, 365 nm). In contrast, the neutral complexes exhibited only weak luminescence (**5'**), or no luminescence at all (**1'**). These findings prompted an investigation of the observed photophysical behaviour.

Some of the discussed results have already been published,[82-83] whereas the remaining (e.g. singlet oxygen assay) are subjects of a prepared manuscript.

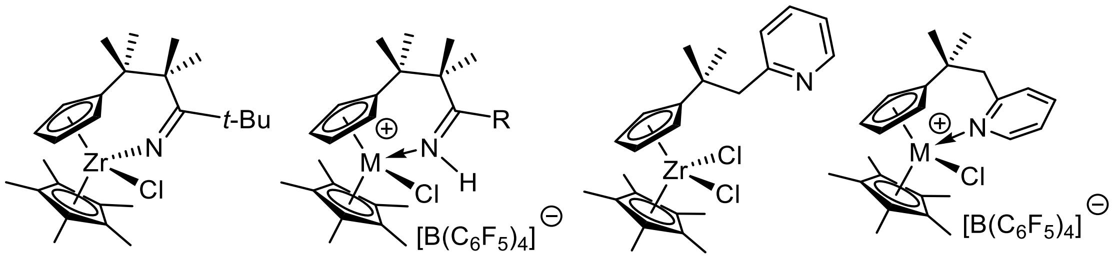

1'

1 (M = Zr, R = *t*-Bu)
2 (M = Zr, R = Ph)
3 (M = Hf, R = *t*-Bu)
4 (M = Ti, R = *t*-Bu)

5'

5 (M = Zr)
6 (M = Ti)

Figure 34: Studied metallocene complexes with pendant *N*-donor ligands.

4.1.1 Preparation of cationic complexes **1–6**

Cationic complexes **1–6** were prepared from corresponding neutral precursors **1'–6'**. Neutral metallocene complexes **1'–6'** were prepared by transmetallation of (di)lithium salts of the *N*-donor ligands by (pentamethyl)cyclopentadienylzirconium(IV) trichloride, (pentamethyl)cyclopentadienylhafnium(IV) trichloride or (pentamethyl)cyclopentadienyltitanium(IV) trichloride.

Dilitihium salts **a**, **b** were prepared in two steps (Figure 35). In the first step, 6,6'-dimethylfulvene was functionalized by lithium isobutyronitrile, which was generated *in situ* by reaction of isobutyronitrile with lithium diisopropylamide (LDA). In the second step, the prepared monolithium salts were functionalized by *tert*-butyllithium or phenyllithium, yielding the target dilithium salt.

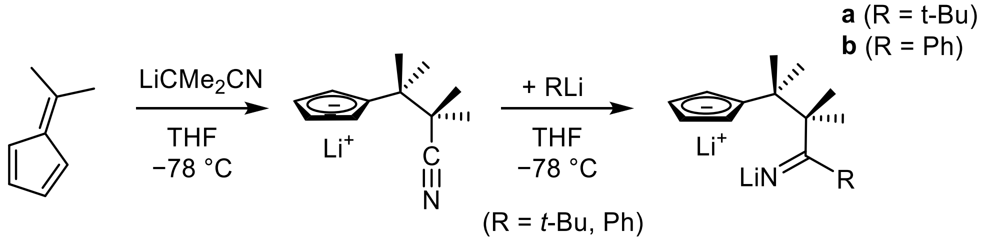

Figure 35: Preparation of dilithium salts **a** and **b**.

Lithium salt **c** was prepared similarly to **a** and **b**. Lithium 2-methylpyridinyl, generated *in situ* by reaction of 2-methylpyridine with butyllithium, was added onto 6,6'-dimethylfulvalene (Figure 36).

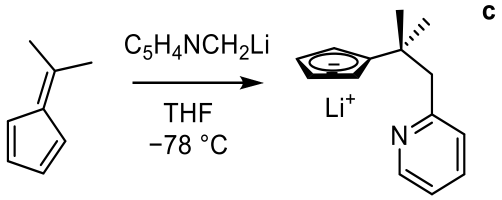

Figure 36: Preparation of lithium salt **c**.

The (di-)lithium salts **a–c** were transmetalated by a cyclopentadienyl metal trichloride (M = Zr, Ti, Hf) which led to the formation of **1–6** (Figure 37**,** Figure 38). Cationic complexes **1–6** were prepared either by (1) protonation of the ketimide moiety of **1'–4'** by $PhNMe_2H[B(C_6F_5)_4]$ (Figure 37) or by (2) abstraction of chloride ligand of **5',6'** by $Li[B(C_6F_5)_4]\cdot2.5Et_2O$ (Figure 38). Both precursor complexes **1'–6'** and target cationic complexes **1–6** were recrystalized by slow diffusion of two solvents (chlorobenzene/hexane).

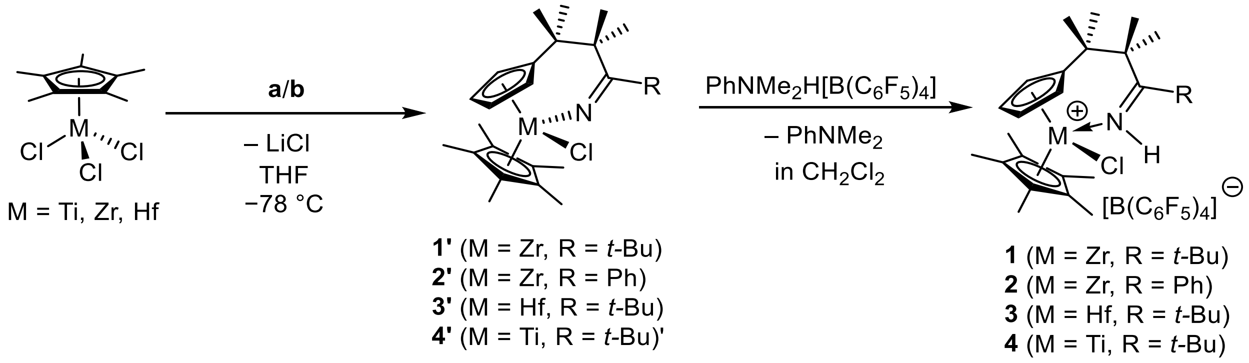

Figure 37: Preparation of cationic complexes **1**–**4**.

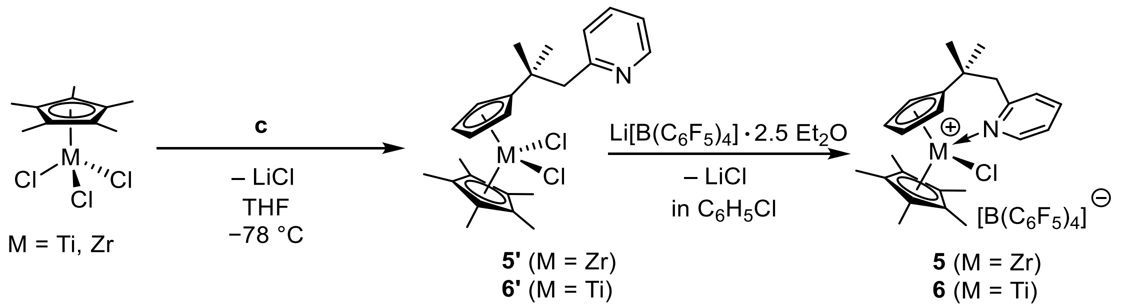

Figure 38: Preparation of cationic complexes **5** and **6**.

4.1.2 NMR spectra of compounds **1’**–**6’** and **1**–**6**

The primary method of characterization of the prepared compounds was ^{1}H a ^{13}C nuclear magnetic resonance (NMR) spectroscopy. The herein listed NMR signals were of corresponding integral intensity to the assigned group if not otherwise specified.

^{1}H NMR spectra of all complexes contained a characteristic singlet of the C_5*Me*$_5$ group (italics distinguish the group containing the observed signals) and two multiplets of the proximal and distal C-*H* groups of C_5*H*$_4$. The pendant ‘arms’ of complexes **1’**–**4’** and **1**–**4** were represented by four singlets of the C*Me*$_2$ groups and a singlet corresponding to the C*Me*$_3$ group in complexes **1’, 2**, **4’** and **1**, **2**, **4** or a multiplet corresponding to the *Ph* group in complexes **3’** and **3**. ^{1}H NMR spectra of **5’**, **6’**, **5**, **6** contained two singlets of C*Me*$_2$ groups and one singlet of the C*H*$_2$ group. The 2-pyridyl group of these complexes was represented by three multiplets of integral intensities 2H and 2× 1H. Cationic complexes **1**–**4** also contained a characteristic N-*H* singlet in the range of 8.97–9.96 ppm.

^{13}C spectra of the compounds contained all the corresponding *C*-H peaks, which were distinguished by APT, HMBC and HSQC. ^{13}C NMR spectra of the cationic complexes **1**–**6** also contained 3 broad doublets *C*-F corresponding to *ortho*, *meta* and *para* carbon atoms of $[B(C_6F_5)_4]^-$.

^{1}H and ^{13}C NMR spectra of the lithium salts **a**–**c** were analogous (although shifted) to those of the neutral complexes, with the obvious exception of C_5*Me*$_5$ peaks.

4.1.3 X-ray diffraction analysis of compounds **5’**, **1–6**

Compounds **5’**, **6’** and **1–6** were investigated by single-crystal X-ray diffraction analysis. Collected data for precursors **1’–4’** were previously published. Molecular structures of the studied compounds are in agreement with the expected products.

All cationic complexes crystallized as racemic mixtures. It is of note that the M-N bond length increases in cationic species **2–6** compared to their neutral precursors **2’–6’** (cf. 2.2552(13) Å for **1** vs 2.011(2) Å for **1′**, 2.230(2) Å for **3** vs 1.992(2) Å for **3′**, 2.1554(12) Å for **4** vs 1.891(2) Å for **4′**). The relationship is reversed in pair **1’** and **1**. M-N bond lengths between the isostructural cationic ketimide species **1**, **3**, **4** follow a relationship of Ti < Hf < Zr and are in all cases shorter than in **5** and **6** (2.317(2) and 2.238(2) Å). $[B(C_6F_5)_4]^-$ are present in the structures of ionic complexes **1–6**, but do not significantly interact with cationic species.

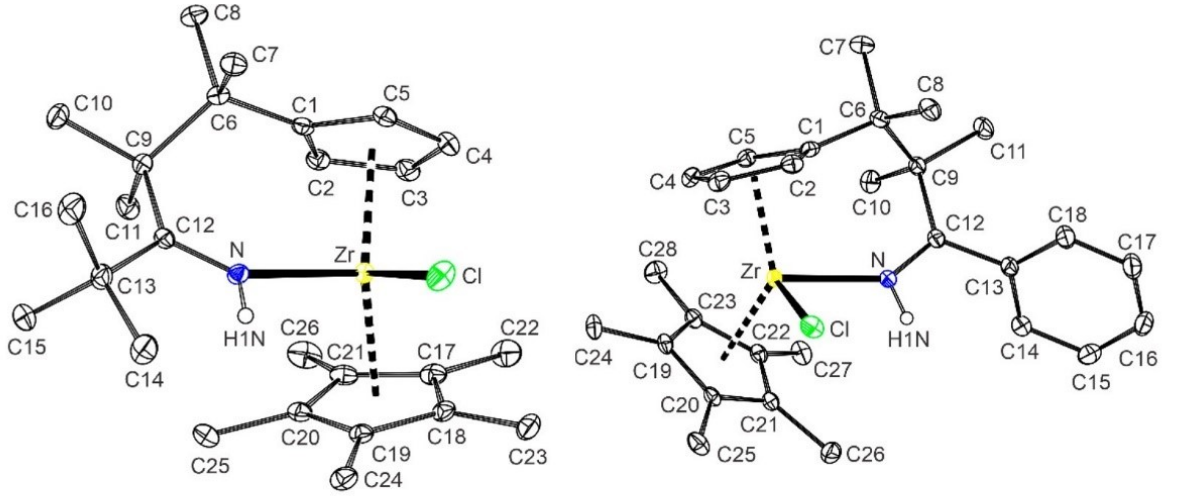

Figure 39: (Left) Molecular structure of **1.** Compounds **3** and **4** are isostructural.[82] (Right) Molecular structure of **2**; (only the cations are displayed, $[B(C_6F_5)_4]^-$ anion omitted) with thermal displacement ellipsoids at 30% probability level and hydrogen atoms omitted for clarity except for N-H of the imine moiety.

5’ has its pendant pyridyl twisted away from the metallocene moiety. Upon cation generation, the 2-pyridyl moiety is coordinated according to expectations, stabilizing the cationic Zr^+.

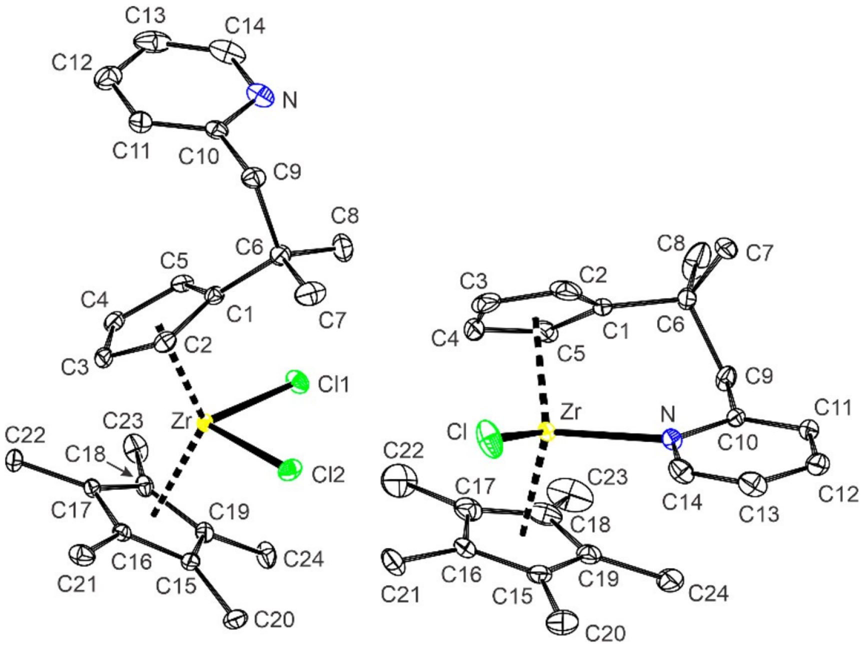

Figure 40: (Left) Molecular structures of **5’** (right) Molecular structure of **5** (only the cation is displayed, $[B(C_6F_5)_4]^-$ anion omitted) with thermal displacement ellipsoids at 30% probability level and hydrogen atoms omitted for clarity. Compound **6** is isostructural.[82]

4.1.4 Photophysical properties of complexes 1’, 5’, 1–6

Absorption and luminescence properties of compounds **1’**, **5’**, **1–6** were studied spectroscopically. In addition Cp_2ZrCl_2, Cp_2TiCl_2, $Cp^*_2ZrCl_2$ and lithium tetrakis(pentafluorophenylborate) ($Li[B(C_6F_5)_4]$) were used throughout the study to demonstrate the impact the studied ligands on the photophysical properties of group 4 metallocenes and to adjust for the photophysical properties of $[B(C_6F_5)_4]^-$. UV-VIS absorption spectra were measured in argon-saturated dichloromethane solutions. Luminescence spectra, decay kinetics and absolute quantum yield measurements were conducted both in solid state and in argon-saturated dichloromethane solutions. Singlet oxygen assay was performed in dichloromethane solution. Singlet oxygen $O_2(^1\Delta_g)$ quantum yield was measured directly by time-resolved measurement of its luminescence at 1270 nm. Full experimental details are found in 6.3.1, 6.3.2, 6.3.3.

All studied compounds exhibited absorption bands in the ultraviolet A (UV-A, 320–400 nm) region of the UV-VIS absorption spectra, which extend into the visible region, with the exception of Cp_2ZrCl_2 (Figure 42). Titanium complexes Cp_2TiCl_2, **4** and **6** had additional absorption bands in the visible spectrum, extending beyond 500 nm.

$[B(C_6F_5)_4]^-$ absorbs weakly in the UV-A region. Therefore, it should have only negligible effect on primary photophysical properties of metallocenes excited by UV-A irradiation.

Only cationic Zr and Hf complexes exhibited strong luminesce in solution ($\Phi_L \geq 0.05$), were attributed to long-lived ^{3}LMCT in the range of 520–585 nm (Figure 41). Samples in dichloromethane solutions have bathochromically shifted luminescence maxima by ~25 nm compared to solid-state samples and also exhibit a lower quantum yield of luminescence Φ_L. These findings were interpreted to indicate a less confined geometrical relaxation of emissive excited states in solution and their increased nonradiative deactivation by surrounding solvent molecules.

Upon exposure of the dichloromethane solutions to air, the ^{3}LMCT states of **1**–**3** and **5** were efficiently quenched. These findings contrast the lack of quenching in solid-state samples, as demonstrated in Figure 43. The fraction F_T^{air} of the excited triplet states quenched by molecular oxygen ranged from 0.43 (for **3**) to 0.97 (for **1**) (Table 1).

Singlet oxygen assay in air-saturated dichloromethane solution revealed that metallocene dichlorides Cp_2TiCl_2, Cp_2ZrCl_2 and $Cp^*_2ZrCl_2$, cationic titanium complexes **4**, **6** and neutral ketimide complex **1'** did not generate detectable yields of singlet oxygen ($\Phi_\Delta < 0.05$). $[B(C_6F_5)_4]^-$ interestingly did generate singlet oxygen (Φ_Δ ~0.15) upon irradiation. However, the molar absorption coefficient at the excitation wavelengths was too low (Figure 43) to account for observed photogenerated singlet oxygen when accompanied by a strongly absorbing cation (e.g. **4**, **6**).

Neutral zirconocene complex **5'** generated a singlet oxygen at a low quantum yield ($\Phi_\Delta = 0.09$). In contrast, cationic complexes **1**–**3** and **5** photogenerated singlet oxygen at significant yield ($\Phi_\Delta > 0.2$), ranging up to $\Phi_\Delta = 0.77$ for complex **1**. The high Φ_Δ values of **1**–**3** and **5** correlate with the fraction of the excited triplet states quenched by oxygen, F_T^{air}, indicating an efficient inter-system crossing of the metallocene complexes.

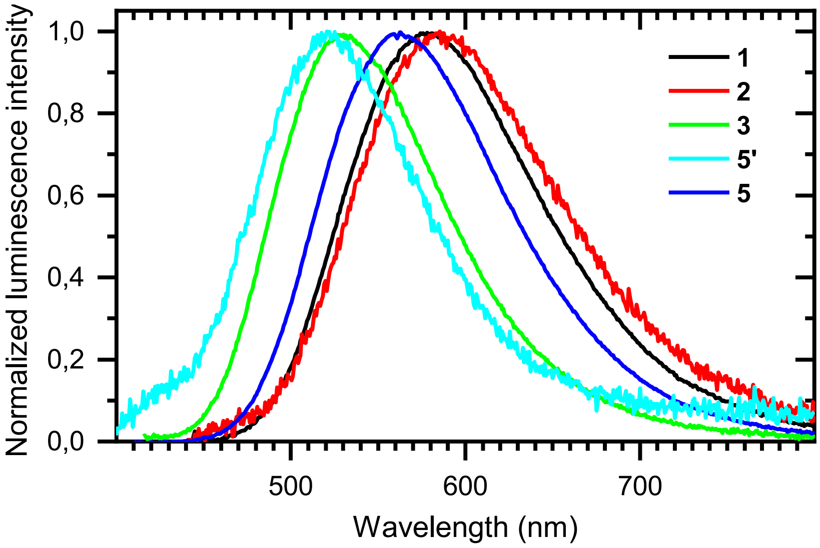

Figure 41: Overlaid normalized emission spectra of **1**–**3**, **5'** and **5** measured in argon-saturated dichloromethane solutions.

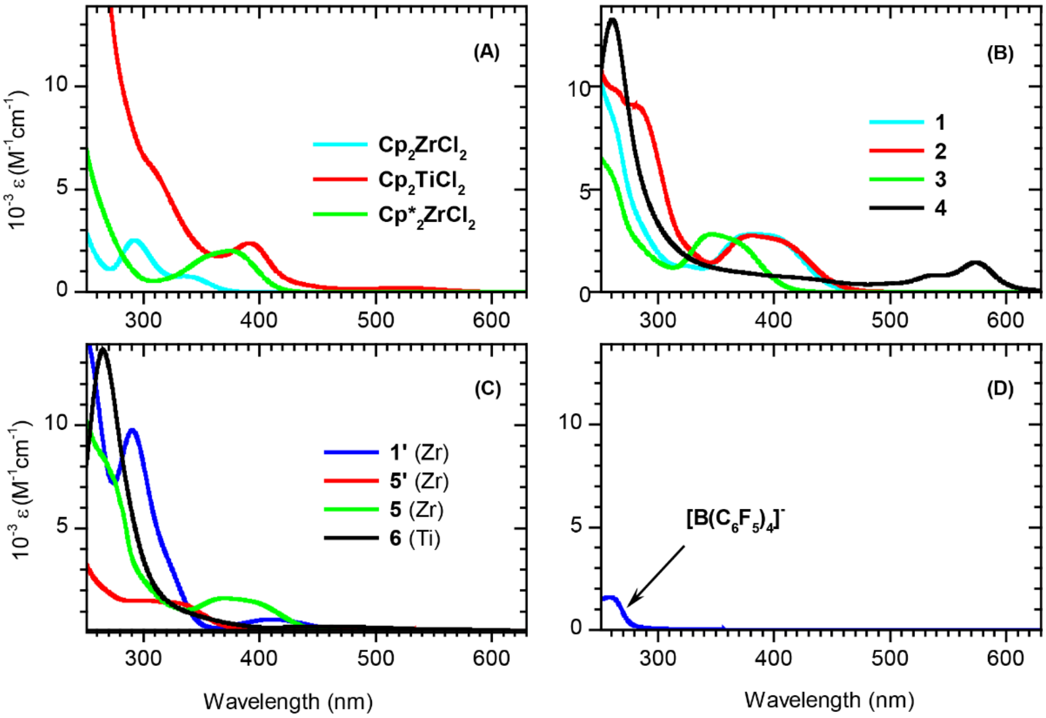

Figure 42: Overlaid UV-VIS absorption spectra of A) Cp_2ZrCl_2, Cp_2TiCl_2, $Cp^*_2ZrCl_2$, B) cationic complexes **1**–**4**, C) neutral complexes **1'**, **5'** and cationic complexes **5**, **6**, and D) absorption spectrum of $[B(C_6F_5)_4]^-$, measured in dichloromethane.

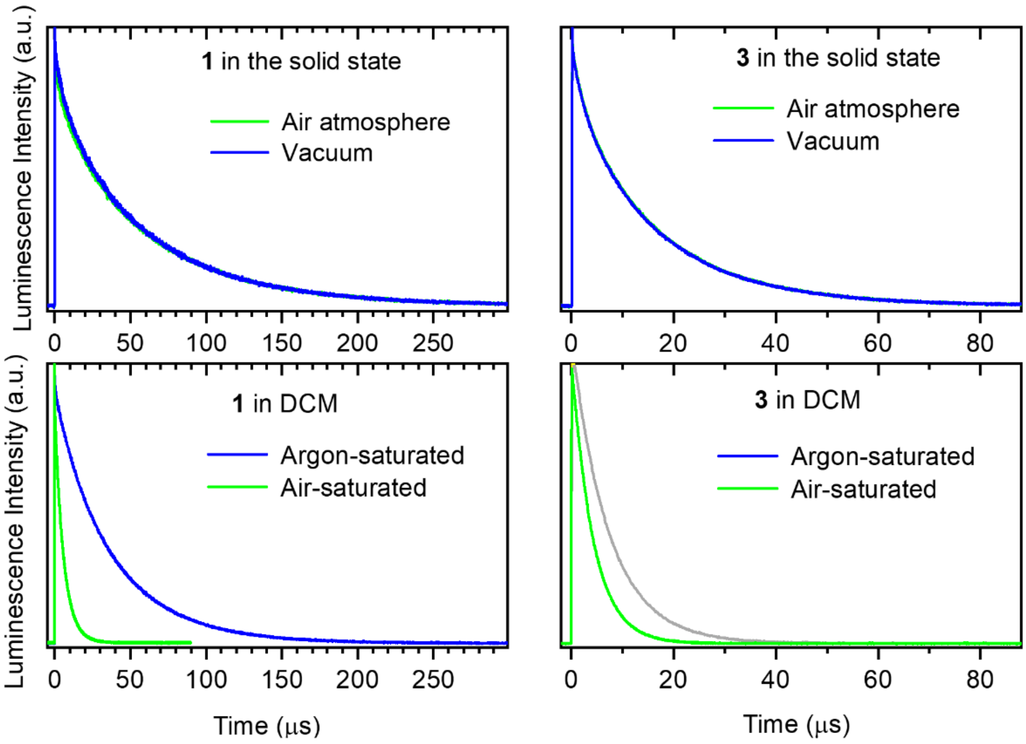

Figure 43: Luminescence quenching of **1** and **3** in the solid state in air atmosphere and vacuum (upper panels), and corresponding argon- and air-saturated dichloromethane solutions (bottom panels).

Table 1: Photophysical data of metallocenes **1 – 6**, **1’**, **5’** and control metallocene dichlorides Cp_2TiCl_2, Cp_2ZrCl_2 and $Cp^*{}_2ZrCl_2$ in dichloromethane solutions at room temperature: Φ_L is the luminescence quantum yield, λ_L is the maximum of the luminescence band in argon-saturated solutions τ_L is the luminescence lifetime in oxygen-, air- and argon-saturated solutions, k_{O2} is the bimolecular rate constant for luminescence quenching by oxygen, F_T^{air} is the fraction of the triplet states quenched by oxygen in air-saturated solutions, Φ_Δ and τ_Δ are the quantum yield of the $O_2(^1\Delta_g)$ formation and its lifetime, respectively.

	Φ_L	λ_L (nm)	τ_L(μs)			$10^{-7}k_{O2}$ ($M^{-1}s^{-1}$)	F_T^{air}	Φ_Δ	τ_Δ (μs)
			oxygen	air	argon				
Cp_2ZrCl_2	<0.01 (0.70)[b]	~440 (433)[b]	-	-	-	-	-	<0.05	-
Cp_2TiCl_2	-	-	-	-	-	-	-	<0.05	-
$Cp^*{}_2ZrCl_2$	(<0.01)[b]	(~475)[b]	-	-	-	-	-	<0.05	-
1’	-	-	-	-	-	-	-	<0.05	-
5’	0.02 (0.15)[b]	520 (501)[b]	0.40	1.07	2.21	18.2±0.7	0.80	0.09	92
1	0.30 (0.58)[b]	578 (546)[b]	1.05	5.70	37.0	8.5±0.3	0.97	0.77	95
2	0.07 (0.40)[b]	585 (558)[b]	0.73[c]	2.54[c]	7.03[c]	11.0±0.1	0.64	0.33	90
3	0.17 (0.35)[b]	530 (507)[b]	1.48	4.23	7.33	4.9±0.7	0.43	0.29	92
4	-	-	-	-	-	-	-	<0.05	-
5	0.40 (0.48)[b]	563 (535)[b]	1.78	10.1	49.8	5.0±0.3	0.96	0.53	92
6	-	-	-	-	-	-	-	<0.05	-
$Li[B(C_6F_5)_4]$	~0.04[d]	~410	<0.01[d]	<0.01[d]	<0.01[d]	-	-	~0.14	100
Phenalenone[a]	-	-	-	-	-	-	-	0.96[a]	101

[a] Standard (Φ_Δ= 0.96)[84]; [b] Microcrystaline samples, excited at 350 and 400 nm, except of 1 (330 nm in DCM, 350 nm in the solid phase); [c] Double exponential decay; [d] Short-lived fluorescence independent on oxygen concentration.

4.1.5 Computational investigation of the observed phenomena

Kohn-Sham DFT computational methods were applied to aid in the interpretation of the observed experimental properties of compounds **1–6**, **1’** and **5’**. All optimized molecular geometries (**1’, 5’**) and geometries of lone cations (**1**–**6**) are in agreement with the determined solid-state structures. Cationic species were investigated as lone cations with implicit solvent models applied to optimization and TD-DFT calculations. Second-order Douglas-Kroll-Hess Hamiltonian was applied to evaluate scalar-relativistic spin-orbit coupling. Calculated singlet-singlet transitions approximating the ionic compounds as lone cations sufficed in assignment of the measured UV-VIS absorption spectra (Figure 44).

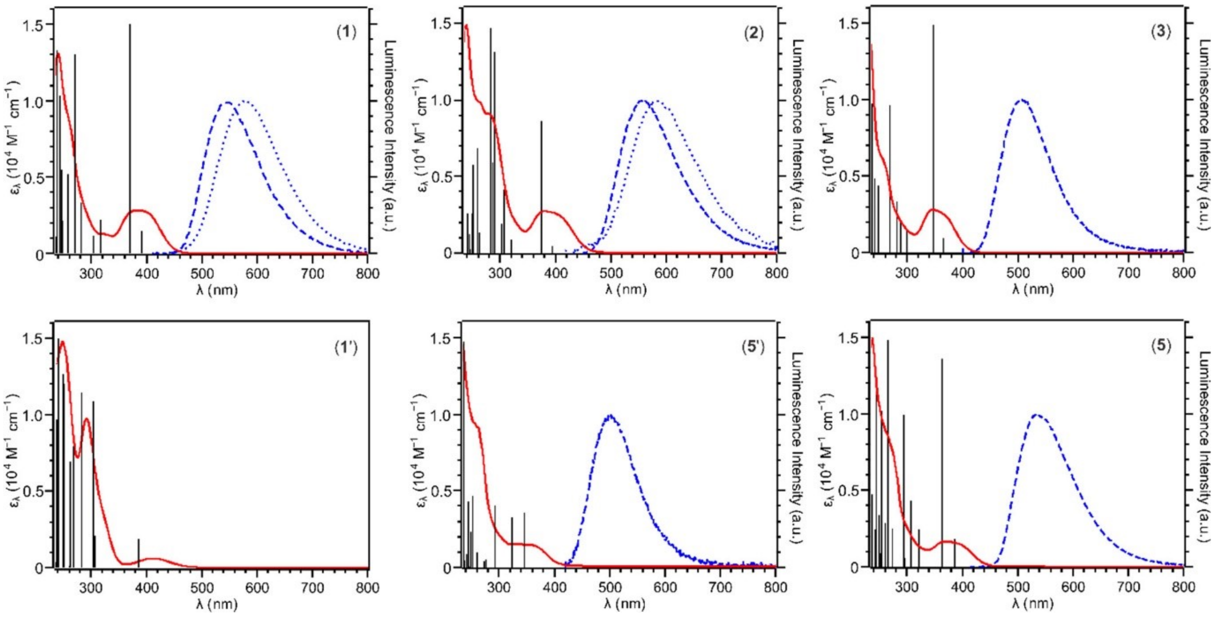

Figure 44: Electronic absorption (solid red line) of complexes **1**–**3**, **5**, **1′**, and **5′** measured in dichloromethane solutions overlaid by the calculated electronic transitions obtained from TD-DFT calculations (stick-plot indicating positions and relative intensities) for title complexes. Normalized luminescence spectra (solid blue line–in the solid state, dotted blue line–in dichloromethane solutions) were obtained upon excitation at 380 nm. Reprinted with permission.[82] Copyright 2021 American Chemical Society.

Both qualitative and quantitative analysis of the Kohn-Sham orbitals which partake in the electronic transition indicate that the lowest-lying excited states of both neutral and cationic species are dominated by LMCT transitions (Table 2). These transitions originate from π–orbitals of Cp*, with the exception of complex **1’**, in which transition orbitals are localized on the coordinated ketimide moiety.

The energy of the first singlet-singlet transition of the cationic complexes is dominated by periodic (table) trends of *d*-orbital energy, which results in a hypsochromic shift in order of Ti < Zr < Hf in structurally analogous species. Higher excited states involve electronic transitions from lower occupied orbitals, e.g. HOMO–1, HOMO–2, to the LUMO. The afore-mentioned periodic table trend, while more subtle, applies to these transitions as well. Only 5th transition in ketimide cationic complexes **1**–**4** and 4th transition of pyridine cationic complexes **5**, **6**, and some higher transitions involve significant contributions of LUMO+1, LUMO+2, etc.

Transitions from π-orbitals of the Cp* ligand constitute HOMO and HOMO–1, followed by π-orbitals of the monosubstituted cyclopentadienyl ligand HOMO–2 and HOMO–3. HOMO–4 are assigned to π-orbitals of the aromatic moiety of the pendant ligand in **2**, **5**, **6**, or orbitals of the Cl^- in **1, 3, 4**. LUMO to LUMO+4 most strongly resemble *d*-orbitals of the central atom with mixed π-orbitals of either the aromatic (in **5**, **6**) or the ketimide (in **1**–**4**) moiety. LUMO+1 of **5**, **6** has a majority 2-pyridinyl character. Any lower and higher molecular orbitals contribute by negligible (weight < 0.01) contributions to the observed photophysical phenomena (in the considered UV-VIS region).

By comparing neutral complexes **1’** and **5’** to their corresponding cationic complexes **1** and **5**, it was found that parent neutral complex **1’** exhibits a contrasting, primarily ketimide-localized HOMO-LUMO transition, followed by series of analogous transitions to **1**. In contrast, **5’** and **5** follow the same orbital assignment scheme, with shifted energy levels of LUMO.

The assignment of calculated triplet-singlet emission of the cationic species (**1**–**6**) at their optimized lowest-energy triplet state geometry is complementary to the first singlet-singlet transition (Table 3). It can be concluded that triplet-singlet emission wavelengths of cationic species (**1**–**6**) are most significantly governed by the central atom, decreasing in the order Ti > Zr > Hf. Calculated emission wavelength of titanocenes **4** and **6** corresponds to infra-red region of the electromagnetic spectrum, which is in agreement with the lack of experimentally observed luminescence.

Upon attempting to extend this interpretation to the neutral species, an interesting difference was spotted when comparing orbitals involved in emission of **1** and **1’** vs. **5** and **5’** **(**which suggest that the absence of observed luminescence in the neutral ketimide species **1’** (in contrast to **1**, **5’** and **5**) is attributed to a LMCT transition with significant contribution of ketimide ligand. The ligand-centred LUMO results in a significantly lower energy lowest lying triplet state. Thus, the calculated triplet-singlet emission of **1’** is not observed under experimental conditions similarly to titanocenes **4** and **6**, due to its low energy (corresponding to IR wavelengths) as opposed to luminescent neutral complex **5’** which exhibits luminescence corresponding to the calculated triplet-singlet transition. It can therefore be concluded that in complexes **1**–**3**, **1’**–**3’**, the generation of cationic species is required to achieve luminescence, whereas in **5’**, **5** the neutral complex already is luminescent and cation generation enhances the quantum yield.

Including implicit solvation mimics the bathochromic solvent shift of **5’**. The same does not hold for the cationic complexes **1**–**5**. This result suggests that the polarizability of the ionic solid phase modulates the emission wavelength similarly to a solvent.

Table 2: Selected calculated singlet-singlet ($S_0 \rightarrow S_n$, n = 1,2,3) transition energies *E* and corresponding wavelength *λ*, oscillator strength *f*, molecular orbital assignment and assigned charge-transfer character, at ground state singlet geometry, optimized and calculated in implicit solvent model of dichloromethane.

	S_n	*E* cm^{-1}	*λ* nm	$f\times10^4$	MO assignment			CT character			
1	1	25387	394	270	129	→	130	Cp*	→	M, L	(LMCT, LLCT)
	2	26426	378	540	128	→	130	Cp*	→	M, L	(LMCT, LLCT)
	3	31278	320	230	127	→	130	C_5H_4	→	M, L	(LMCT, LLCT)
2	1	24893	402	240	133	→	134	Cp*	→	M, L	(LMCT, LLCT)
	2	26020	384	520	132	→	134	Cp*	→	M, L	(LMCT, LLCT)
	3	30817	325	210	131	→	134	C_5H_4	→	M, L	(LMCT, LLCT)
3	1	27170	368	190	145	→	146	Cp*	→	M, L	(LMCT, LLCT)
	2	28497	351	540	144	→	146	Cp*	→	M, L	(LMCT, LLCT)
	3	33147	302	240	143	→	146	C_5H_4	→	M, L	(LMCT, LLCT)
4	1	19503	513	210	120	→	121	Cp*, C_5H_4, Cl	→	M	(LMCT)
	2	21620	463	540	119	→	121	Cp*	→	M	(LMCT)
	3	25576	391	530	118	→	121	C_5H_4	→	M	(LMCT)
5	1	25797	388	210	118	→	119	Cp*	→	M	(LMCT)
	2	27089	369	480	117	→	119	Cp*	→	M	(LMCT)
	3	31122	321	120	116	→	119	C_5H_4	→	M	(LMCT)
6	1	19237	520	170	109	→	110	Cp*, C_5H_4, Cl	→	M	(LMCT)
	2	21481	466	400	108	→	110	Cp*	→	M	(LMCT)
	3	24628	406	430	107	→	110	C_5H_4	→	M	(LMCT)
1’	1	25555	391	120	129	→	130	L	→	M	(LMCT)
	2	32499	308	56	127,128[a]	→	130	Cp*	→	M, L	(LMCT, LLCT)
	3	33049	303	170	127,128[b]	→	130	Cp*	→	M, L	(LMCT, LLCT)
5’	1	28003	357	30	127	→	128	Cp*, C_5H_4	→	M	(LMCT)
	2	29671	337	410	126	→	128	Cp*	→	M	(LMCT)
	3	33979	294	410	125	→	128	C_5H_4	→	M	(LMCT)

[a]Weight 127 (0.3) 128 (0.6), [b]Weight 127 (0.6) 128 (0.3)

Table 3: Calculated first singlet-triplet transition energy E and corresponding wavelength λ of lowest-energy triplet optimized geometries of **1’**, **5’**, **1–6**, optimized and calculated under vacuum conditions (E_{vac}, λ_{vac}) and an implicit solvent model of dichloromethane (E_{DCM}, λ_{DCM}).

	E_{vac}	λ_{vac}	E_{DCM}	λ_{DCM}
	cm^{-1}	nm	cm^{-1}	nm
1’	11864	843	11346	881
5’	21075	475	19655	509
1	17962	557	18277	547
2	17768	563	18041	554
3	19131	523	19736	507
4	12147	823	11810	847
5	18301	547	18215	549
6	11308	884	11081	902

4.2 Metallocene complexes with *N,O*-chelating ligands

The findings of subchapter 6.1 prompted further interest in photophysical properties of cationic metallocene complexes. Thus, a series of novel complexes was devised. The positive charge of the proposed complexes was to be stabilized by *N,O*-chelating ligands (Figure 45). The complexes were to be prepared by chloride ligand abstraction, similarly to **5** and **6**. The main advantage of this choice of ligands is commercial availability of precursors to the *N,O*-chelating ligands which allows increasing their scope o to assess structure-property relationship of the photophysical properties. The synthesis described in this subchapter was conducted now solely by the author of the thesis.

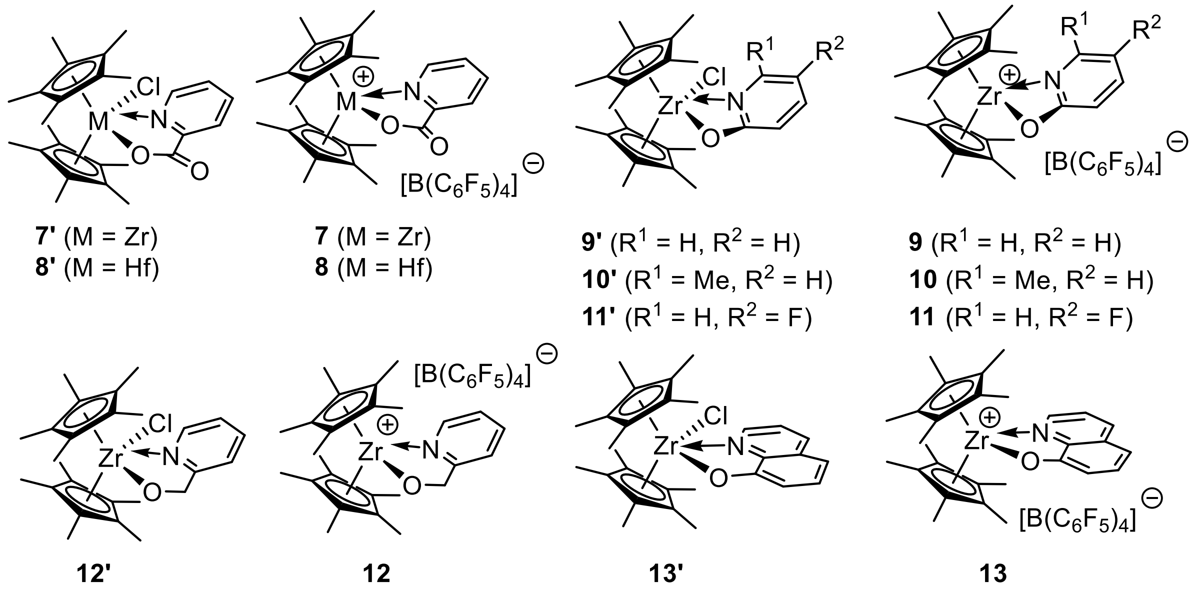

Figure 45: Prepared neutral and cationic complexes with *N,O*-chelating ligands **7’–13’**, **7–13**.

4.2.1 Preparation of neutral metallocene complexes **7’–13’**

Based on the computational results of section 4.1.5, namely the finding that the first two lowest occupied molecular orbitals correspond to the π-bonding orbitals of the Cp* ligand, Cp*$_2$ZrCl$_2$ was selected as the starting material for the synthesis of target neutral complexes. A single hafnium complex **8’** was prepared from Cp*$_2$HfCl$_2$ to replicate previously observed periodic table trends of photophysical properties.

Neutral precursors **7’–13’** were prepared by a two-step procedure (Figure 46). In the first step, sodium salts of the *N,O*-chelating ligands are prepared by reaction of their protonated forms with sodium hydride, isolated and used in a subsequent reaction of the salts with Cp$_2$*MCl$_2$ (M = Zr, Hf) yielding **7’–13’**.

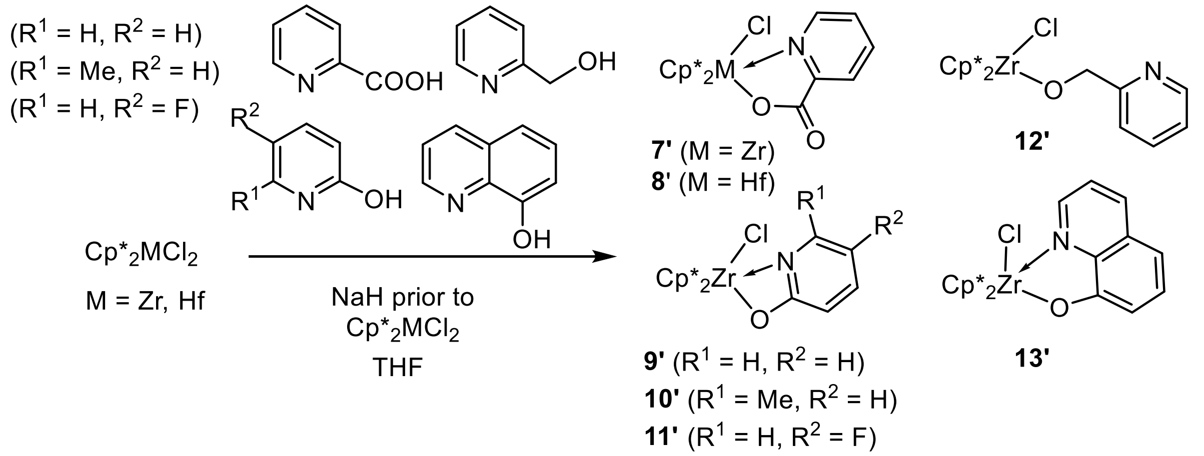

Figure 46: Preparation of neutral precursor metallocene complexes with *N,O*-chelating ligands, **7'–13’**.

The reactions were conducted in tetrahydrofuran at room temperature. The reaction times were extended to a week after initially observed low yields, which were thusly improved. Products were isolated by distilling the solvent from the reaction mixture *in vacuo*, repeated extraction of the crude solid into toluene, distilling the toluene from the toluene phase *in vacuo* and recrystallization of the solid residue by slow diffusion of two solvents: dichloromethane (holding the saturated solution) and excess hexane. The procedure yielded colourless (**8’–11’**), faint-yellow (**7’**, **12’**) and yellow crystals (**13’**).

4.2.2 Preparation of cationic metallocene complexes **7–13**

Cationic complexes were prepared by reaction of the neutral metallocene complexes **7’–13’** with a pre-mixed mixture of Ph$_3$C[B(C$_6$F$_5$)$_4$] and 2 equivalents of triethylsilane (Et$_3$SiH). The reaction of Ph$_3$C[B(C$_6$F$_5$)$_4$] and triethylsilane yields triphenylmethane and a solvent-triethylsilylium complex, which liberates the [B(C$_6$F$_5$)$_4$]$^-$. Upon addition of neutral metallocene complexes **7’–13’**, Et$_3$SiCl is formed by the abstraction of a chloride ligand from the complex, yielding cationic complexes **7–13**.

The reaction is rapid, as indicated by immediate colouring of the colourless mixture of $PhC_3[B(C_6F_5)_4]/2$ eq. Et_3SiH upon adding the neutral metallocene complex. All liquid content in the reaction mixture was distilled *in vacuo* and re-dissolved in a minimal amount of chlorobenzene. Cationic metallocene complexes crystallized from their concentrated chlorobenzene solutions in a matter of days when covered by excess of hexane, yielding yellow (**7**–**12**) and yellow-orange (**13**) crystals which were luminescent under UV–light.

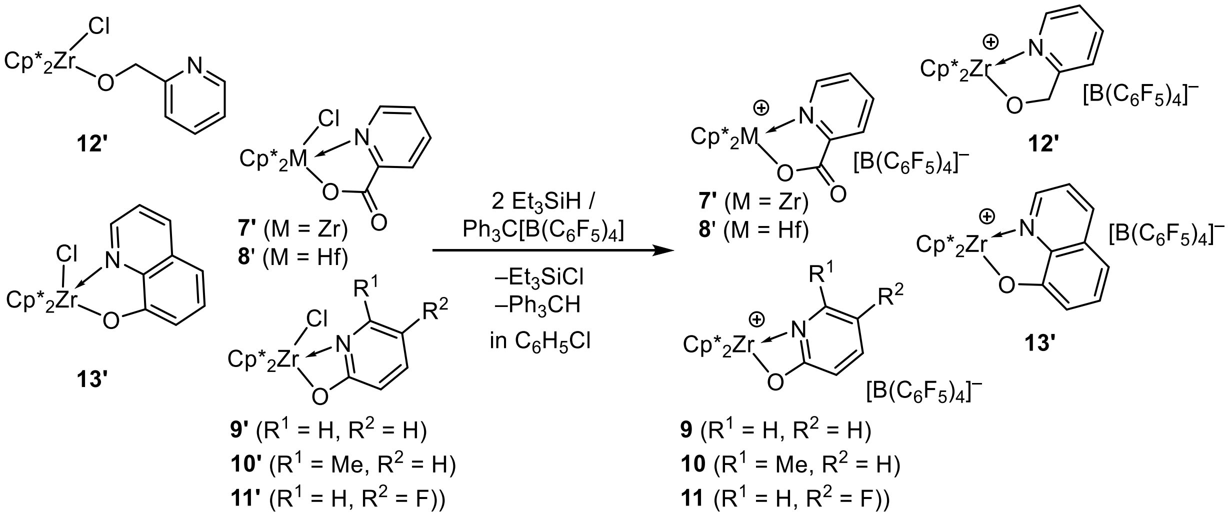

Figure 47: Preparation of cationic metallocene complexes with *N,O*-chelating ligands, **7**–**13**.

The most well characterized reaction of the cationic species is their reaction with water, initiated by exposure of the compounds to air moisture both in solid state and in solution, or to poorly dehydrated solvents. Hydrolysis was the main source of failures when preparing the cationic complexes, despite taking high precautions to avoid exposing the products to moisture. To better understand the underlying process, one of the hydrolysed species was prepared by intentional exposure of **9** to air, isolated by the same crystallization procedure as other cationic complexes and fully characterized.

Based on the collected X-ray data (4.2.4, Figure 57), it was hypothesised that hydrolysis occurs by nucleophilic addition of water to the cationic zirconium and subsequent hydrogen-transfer to the N atom of the heterocyclic ligand, resulting in a newly formed cationic complex which now carries a hydroxide ligand (Figure 48). Interestingly, although the observed complexes lose colour, they do remain luminescent. The observed luminescence shifts from various shades of yellow to various shades of green (with the exception of **13**, of which hydrolysis was not observed). The photophysical properties of these products are described more rigorously in section (4.2.5).

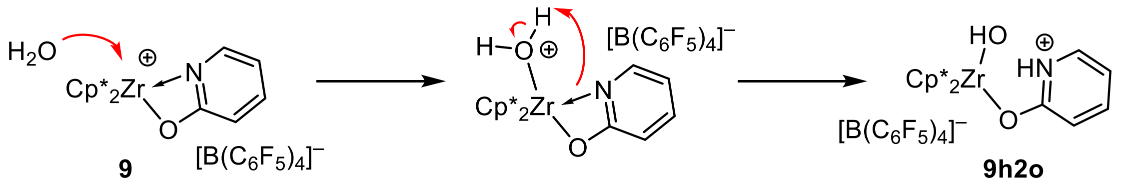

Figure 48: Proposed mechanism of hydrolytic decomposition of **9** to **9h2o**.

This predictable behaviour was quite fortunate. Applying this knowledge, hydrolysis of the cationic complexes was qualitatively indicated under UV-light.

Nevertheless, the reactivity of the compounds posed a challenge to the aims of the project. Firstly, cationic complexes **7**–**13** are unsuitable for photosensitization or photoredox catalysis since introduction to a complex reaction mixture would most likely result in their rapid degradation. Secondly, the technical challenges introduced by the air-sensitivity of the compounds disallowed some of the measurements in liquid solutions which were conducted by third parties who didn't have the necessary equipment to handle such sensitive materials.

4.2.3 NMR spectra of compounds **7'**–**13'**, **7**–**13** and **9h2o**

The primary method of characterization of the prepared compounds was ^{1}H, ^{13}C and ^{19}F NMR spectroscopy. The herein listed ^{1}H NMR peaks were of corresponding integral intensity to the assigned group if not otherwise specified.

^{1}H NMR spectra of all discussed compounds contained a singlet corresponding to ten *Me* groups of the Cp* ligands in range of 1.7–1.9 ppm. Thereafter, the spectra contained a number of multiplets corresponding to C-*H* groups of the respective *N,O*-chelating ligands, scattered in the range of 5.4–9.6 ppm. These signals were multiplets exhibiting second-order splitting patterns. ^{13}C NMR spectra contained the corresponding ^{13}C signals of *Me* groups of Cp* in range 10.8–11.8 ppm and *C* atoms of Cp* in range of 120.3–126.2 ppm. *C* and *C*-H groups of the *N,O*-chelating ligands were scattered in the aromatic region of the ^{13}C NMR spectra and assigned by 1D-NOESY, gCOSY, gHSQC, and gHMBC. ^{13}C NMR spectra of cationic **7**–**13** and also **9h2o** contained three broad doublets of $[B(C_6F_5)_4]^-$ at 149.0, 139.3 and 137.3 ppm, which were accompanied by signals in ^{19}F NMR spectra at −133.7, −163.9, −168.3 ppm.

7' and **8'** exhibited additional ^{13}C NMR signals of the *C*OO groups in range at 166.5 and 166.8 ppm, and corresponding C_{ipso} at 152.5 and 152.1 ppm, respectively.

9'-11' exhibited ^{13}C NMR signals of the *C*O group of 2-pyridinolate at 171.0, 170.6 and 168.2 ppm, respectively. **10'** contained signals of the *Me* group, ^{1}H NMR at 2.65 ppm and ^{13}C NMR at 24.1 ppm, followed by a corresponding C_{ipso} at 139.5 ppm. **11'** exhibited a *C*F ^{13}C NMR signal at 153.4 ppm and a corresponding ^{19}F signal at −144.3 ppm. ^{1}H spectra of **10** contained signals of the *Me* group at

2.42 ppm. In ^{13}C NMR, the *Me* group manifested at 19.0 ppm. ^{13}C NMR spectra of **11** did contain the signal of the *C*F group at 155.4 ppm and a corresponding ^{19}F NMR signal at −142.8 ppm. **9h2o** exhibited analogous spectral pattern to **9**, with two additional broad singlets in ^{1}H NMR at 12.57 ppm, corresponding to the N*H* group and at 5.16 ppm, corresponding to O*H* group.

12' and **12** exhibited signals of the CH_2 group of 2-pyridinemethanolate at 5.36 and 5.45 ppm in ^{1}H NMR spectra and at 73.3 and 76.1 ppm in ^{13}C NMR spectra, respectively. ^{13}C NMR spectra of **12'** also contained a C_{ipso} signal at 163.2 ppm.

^{13}C NMR of **13'** and **13** contained the *C*O of 8-quinolinolate at 163.8 and 163.6 ppm, respectively.

4.2.4 X-ray diffraction analysis of compounds **7'–13'**, **7–13** and **9h2o**

Compounds **7'–13', 7–13** and **9h2o** were investigated by single-crystal X-ray diffraction analysis. Determined molecular structures of the studied compounds are in agreement with the expected products, with the exception of **12'** which will be commented on herein. Compounds **12** and **13'** were investigated, but the obtained data was insufficient for refinement of their solid-state structure. However, the incomplete data did suggest coordination of the pyridine moiety in compound **12,** unlike its precursor **12'** discussed herein. The molecular packing is discussed more thoroughly than previously, as only solid-state luminescence of **7–13** was measured.

Neutral compounds **7'**, **8'** (Figure 49) of the 2-picolinate family are structurally analogous, as are their cations **7**, **8** (Figure 50). Both the neutral and the cationic complexes interact with a second metallocene complex by a weak C-H···O interaction (Figure 51).

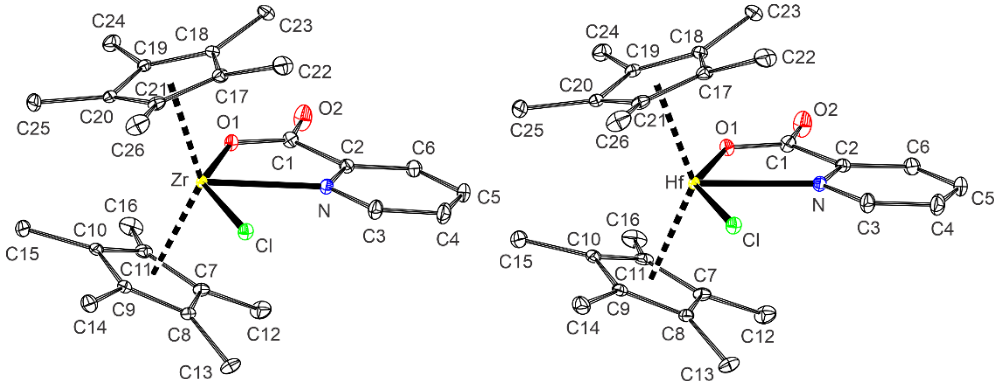

Figure 49: (Left) Molecular structure of **7',** (Right) molecular structure of **8'** with thermal displacement ellipsoids at 30% probability level and hydrogen atoms omitted for clarity.

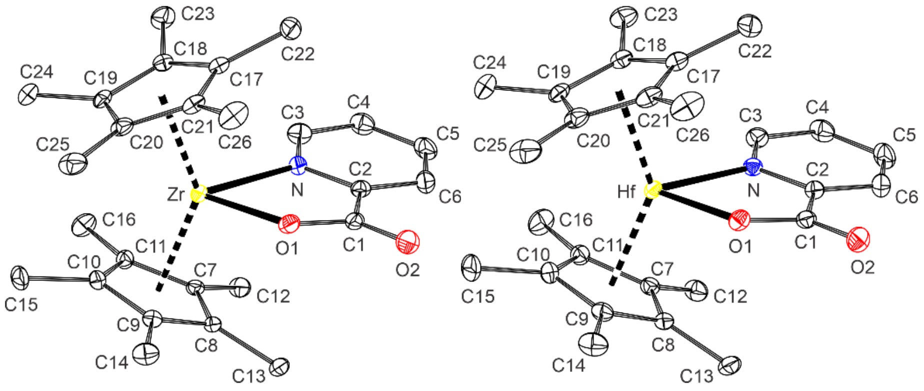

Figure 50: (Left) Molecular structure of **7**, (Right) molecular structure of **8** (only the cation is displayed, $[B(C_6F_5)_4]^-$ anion omitted) with thermal displacement ellipsoids at 30% probability level and hydrogen atoms omitted for clarity.

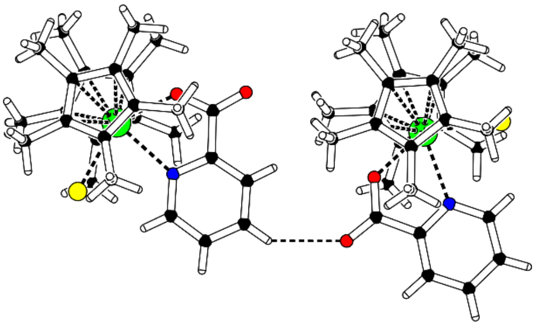

Figure 51: Solid state dimer of **7’** with thermal displacement ellipsoids at 30% probability level. Parameters of displayed interaction: C-H 0.95 Å, H···O 2.55 Å, C···O 3.372(2) Å, C-H···O 145°.

2-pyridinolate complexes **9’–11’** and **9–11** (paired by corresponding parent neutral species and cations in Figure 52, Figure 53, Figure 54) can be also grouped into a single family of structurally analogous complexes. The neutral complexes are chained by weak $CH_3\cdots\pi(C_5Me_5)$ interactions which results in packing of the complexes into 2D matrices. Unlike the 2-picolinate family, cationic complexes 9 and 11 are isolated from other cations in their solid state by six surrounding $[B(C_6F_5)4]^-$, whereas 10 is surrounded by seven weakly interacting $[B(C_6F_5)_4]^-$ and a single weakly interacting cation. s

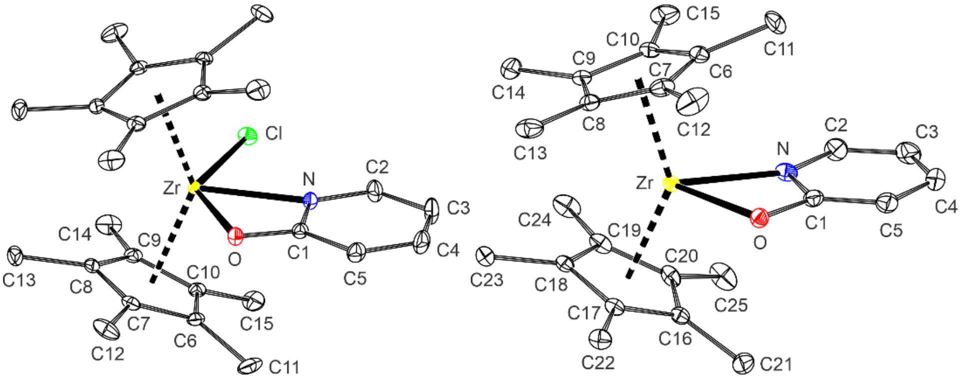

Figure 52: (Left) Molecular structure of **9’**, (Right) molecular structure of **9** (only the cation is displayed, $[B(C_6F_5)_4]^-$ anion omitted), with thermal displacement ellipsoids at 30% probability level and hydrogen atoms omitted for clarity.

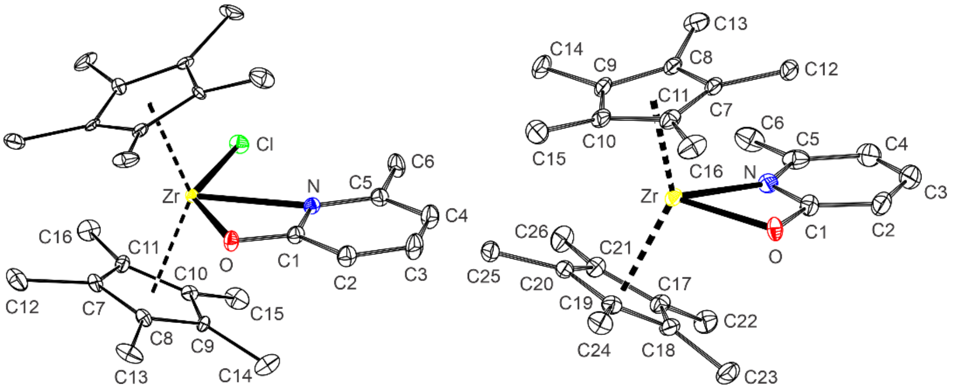

Figure 53: (Left) Molecular structure of **10’** (Right) molecular structure of **10** (only the cation is displayed, $[B(C_6F_5)_4]^-$ anion omitted) with thermal displacement ellipsoids at 30% probability level and hydrogen atoms omitted for clarity

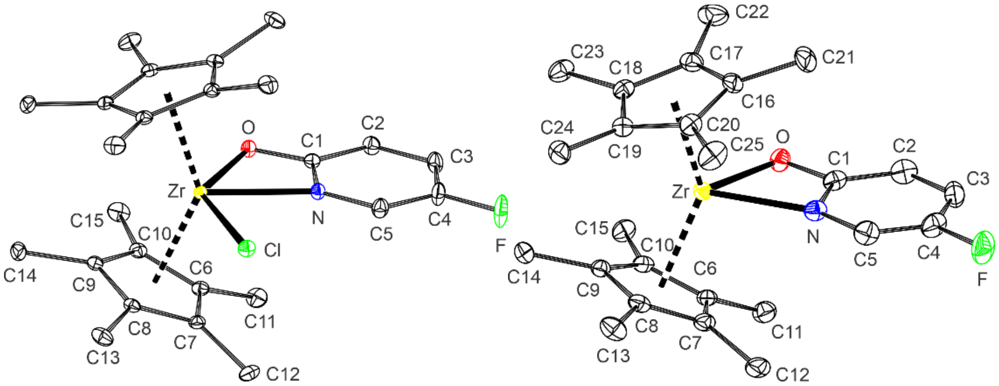

Figure 54: (Left) Molecular structure of **11’** (Right) Molecular structure of **11** (only the cation is displayed, $[B(C_6F_5)_4]^-$ anion omitted) with thermal displacement ellipsoids at 30% probability level and hydrogen atoms omitted for clarity.

12’ (Figure 55) surprisingly forms an of unexpected monodentate coordination isomer.

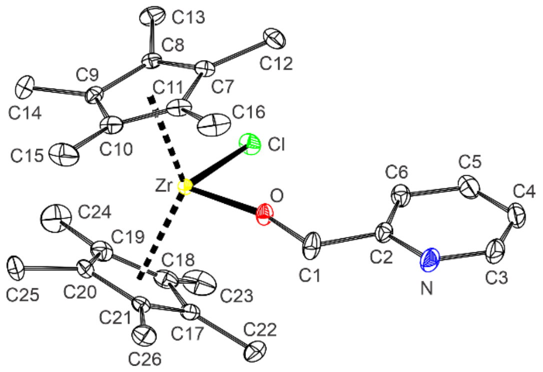

Figure 55: Molecular structure of **12’** with thermal displacement ellipsoids at 30% probability level and hydrogen atoms omitted for clarity.

The 8-oxoquinoline cationic complex 13 (Figure 56) corresponds to the expected product. Each cation is isolated by six weakly interacting $[B(C_6F_5)_4]^-$ in the solid state.

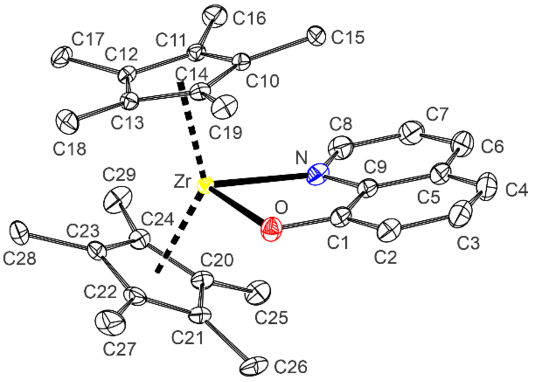

Figure 56: Molecular structure of **13’** with thermal displacement ellipsoids at 30% probability level and hydrogen atoms omitted for clarity.

Hydrolytically formed **9h2o (**Figure 57**)** was successfully characterized by X-ray diffraction analysis. The product remains ionic upon hydrolysis. In the solid state, each cation is surrounded by five $[B(C_6F_5)_4]^-$. A intramolecular hydrogen bond N-H···O was found in the molecular structure.

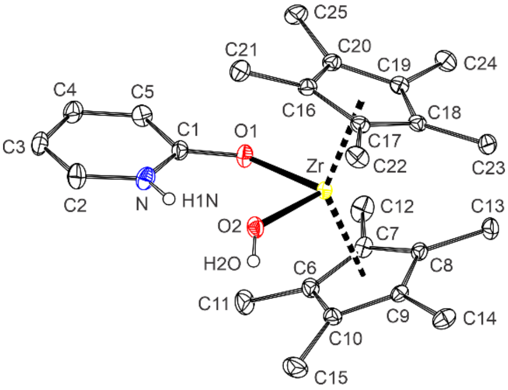

Figure 57: Molecular structure of **9h2o** with thermal displacement ellipsoids at 30% probability level and hydrogen atoms omitted for clarity, with the exception of OH and NH groups. Parameters of displayed interaction: N-H 0.85(3) Å, H···O 2.03(3) Å, N···O 2.821(3) Å, C-H···O 156(3)°.

4.2.5 Photophysical properties of metallocene complexes with *N,O*-chelating ligands

UV-VIS absorption spectra of **7'–13'**, **7–13** and **9h2o** were collected in dichloromethane solutions. Luminescence lifetimes and quantum yields of luminescence of **7–13** were determined in solid-state samples. Attempts to measure the luminescence properties in solution were made. However, the sensitive cationic species were incompatible with the experimental setups used for the measurements. Thus, these results are not presented herein.

The measurements focused on resolving transitions in the UV-A and visible region. The UV-B and higher energy regions exhibited similar intense absorption bands as **1–6** and were minimally impacted by the structure of the particular compounds. The bands responsible for the (near-)visible absorption exhibit a low absorption coefficient (order of 10^2-10^3 M cm^{-1} mol^{-1}) to the adjacent deep-UV band in all complexes with the exception of **13'** and **13** (order of 10^4 M cm^{-1} mol^{-1}) (Figure 58).

Generation of the cationic species **6–12** results in gain of absorption band in the visible region of the spectra (Figure 58, Figure 59). In contrast, the extinction coefficient of the absorption maximum of **13** decreases in respect to **13'** (Figure 58). Hydrolysis results in bleaching of the cationic species, as demonstrated by exposing **9** to air, yielding **9h2o (**Figure 60**)**. Although **9h2o** absorbs in the visible spectrum, the solution appeared colourless due to the low absorption coefficient (similarly to **9'–11'**).

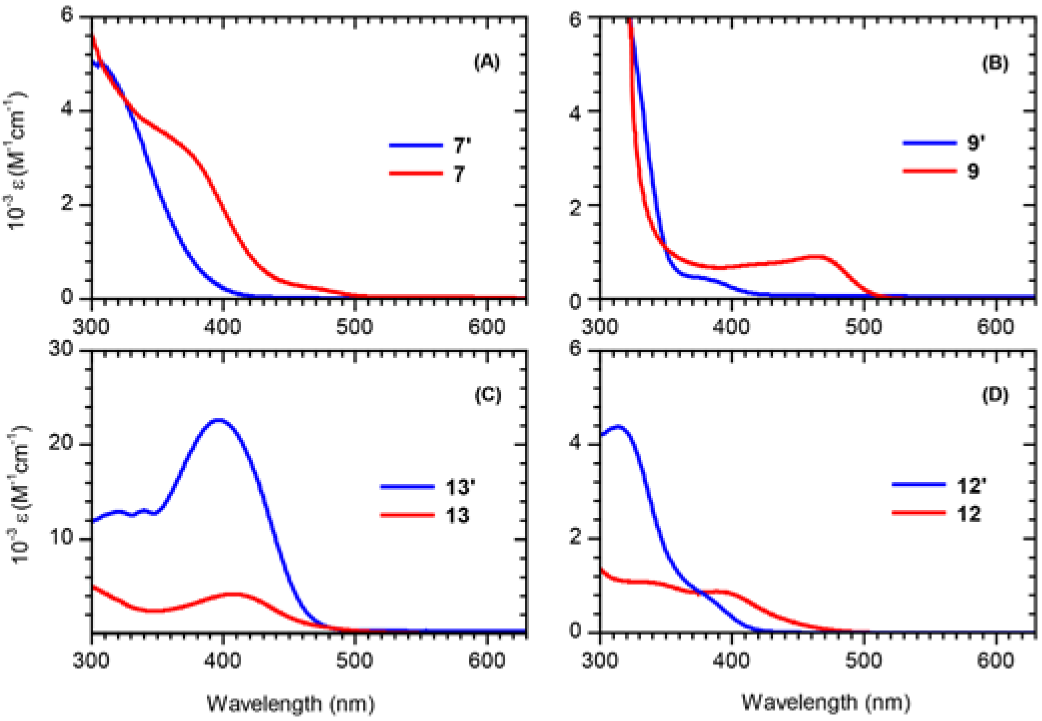

Figure 58: Overlaid UV-VIS absorption spectra of cationic metallocene complexes and their corresponding parent neutral metallocene complexes, A) **7’** and **7**, B) **9’** and **9**, C) **13’** and **13**, D) **12’** and **12,** measured in dichloromethane.

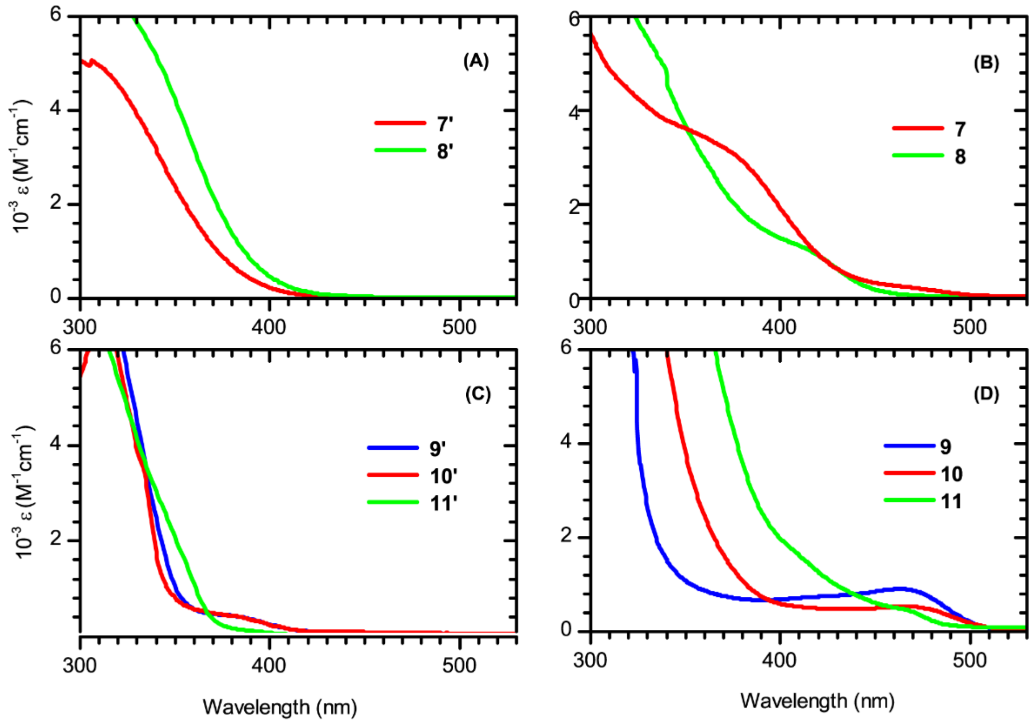

Figure 59: Overlaid UV-VIS absorption spectra of the A) neutral **7’**, **8’** and B) cationic **7**, **8** structurally related complexes of zirconium and hafnium, and overlaid UV-VIS spectra of C) neutral **9’**, **10’**, **11’**

and D) cationic **9**, **10**, **11** metallocene complexes with coordinated derivatives of 2-pyridinolate, measured in dichloromethane.

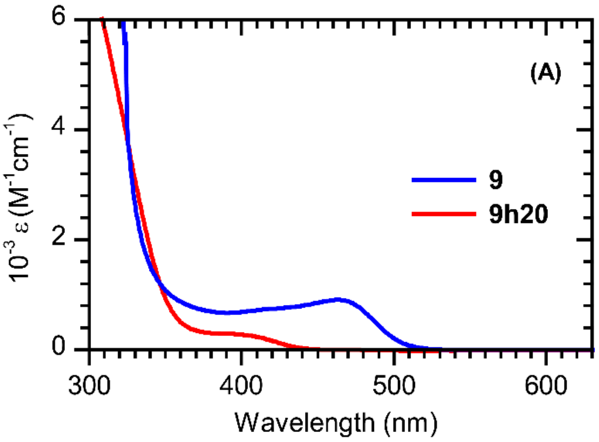

Figure 60: Overlaid UV-VIS absorption spectra of cationic metallocene complex **9** and its hydrolytic product **9h2o**, measured in dichloromethane.

Cationic metallocene complexes **7**–**13** exhibited room-temperature luminesce in both solid-state samples and in their respective reaction mixtures (in chlorobenzene, monitored qualitatively by a TLC lamp). Wavelengths of emission maxima of **7**–**13** in solid-state samples ranged from 520 nm to 616 nm, with lifetimes in the order of 10^1 μs (Table 4). As previously, emission wavelength of hafnium complex **8** (520 nm) were hypsochromically shifted in reference to the structurally related zirconium complex **7** (575 nm). The emission wavelength of zirconium complexes **7**, **10**–**12** exhibited only minor shifts by differing *N,O*-chelating ligands (560-580 nm). **9** produced two emission maxima (520 and 560 nm), which are attributed to partial hydrolysis in the solid state. Isolated hydrolytic product **9h2o** emitted at 510 nm. Luminescence of **13** is significantly bathochromically shifted, which is attributed to enhanced delocalization of the excited electron across the 8-quinolinolate ligand.

Table 4: Measured photophysical parameters of luminescence of metallocenes **7**–**13** and **9h2o** in solid-state samples excited by irradiation at 350 and 400 nm, at room temperature: Φ_L is the luminescence quantum yield, λ_L is the maximum of the luminescence band in argon-saturated solutions τ_L.

	λ_L nm	τ_L μs	Φ_L
7	575	23.2	0.25
8	520	10.0	0.35
9	520[a]	11.4[a]	0.35[a]
	560[b]	22.0[b]	0.52[b]
9h2o	510	17.6	*n.d.*
10	580	30.4	*n.d.*
11	588	41.0	*n.d.*
12	560	24.4	0.47
13	616	28.0	*n.d.*

[a]Collected when irradiated by 350 nm. [b]Collected when irradiated by 450 nm.

4.2.6 Computational investigation of photophysical properties of metallocene complexes with *N,O*-chelating ligands

7’–13’, 7–**13** and **9h2o** were investigated computationally, using the same methods as in 4.1.5. As previously, the cationic species were investigated as lone cations with implicit solvent models applied to optimization and TD-DFT calculations of ground state geometry transitions. Second-order Douglas-Kroll-Hess Hamiltonian was applied to evaluate scalar-relativistic spin-orbit coupling. Ground state optimized geometries were in all cases in good agreement with the X-ray determined geometries, with the exception of the O-H bond of **9h2o**, which is not unexpected given that its position was refined based on differential Fourier map analysis. For the purpose of discussion, the compounds can be divided by their *N,O*-chelating ligands into 2-pyridinolate (**7’**, **8’,** 7, **8**), 2-picolinate (**9’**–**11’**, **9**–**11**), 2-pyridinemethanolate (**12’**, **12**) and 8-quionolinolate families (**13’**, **13**).

The following discussion focuses on the interpretation of the observed photophysical. Assignment of the absorption spectra is limited to transitions in the visible and the UV-A region of the electromagnetic spectrum, as later transitions are typically heavily crowded and mixed. For compounds which exhibit transitions only beyond the UV-A region, a threshold of 300 nm was chosen for the sake of discussion.

Interestingly, in contrast to **1**–**6**, **1’** and **5’**, spin-forbidden singlet-triplet transitions significantly contribute to the shape of the measured absorption spectra. These will be discussed herein in further detail. However, the discussion shall only focus on those which are directly observed in the measured spectra (e.g. not overshadowed by singlet-singlet transitions). Given that the calculated transitions have three substates, the energy listed for each of these transitions corresponds to the median energy of the three transitions and the oscillator strength were summed over all substates.

4.2.6.1 Photophysical properties of 2-pyridinolate family

TD-DFT calculations of the neutral species are consistent with the measured absorption spectrum (Table 5). **7’** in ground state geometry exhibits a first calculated singlet-singlet transition at 379 nm, followed by transitions at 361 nm and 351 nm, which all correspond to the first experimentally observed peak in the absorption spectra. Latter transitions, starting by 318 nm, become highly crowded.

The transitions are assigned (in listed order) to HOMO → LUMO, HOMO−1 → LUMO… HOMO−3 → LUMO, only then followed by a HOMO → LUMO+1 transition. This behaviour was explained by a higher separation of LUMO and LUMO+1, compared to HOMO,… HOMO−3. As was the case of **1**–**6**, the first 4 lowest occupied orbitals are highly delocalized across the Cp* ligands and partially zirconium (e.g. 6% of HOMO) and chloride (11% HOMO−1). In contrast to **1**–**6**, and also **1’** and **5’**, the two lowest unoccupied orbitals are well localized on the 2-picolinate ligand, only then followed by a metal-centred LUMO+2.

Orbital assignment of transitions of **8’** is analogous to **7’**. Interestingly, contrary to the expected periodic table trend, the isostructural **8’** exhibited only minor shift in its absorption spectrum relative to **7’**. This was explained by the limited role of the central atom in the lowest electronic transitions.

Upon formation of cation **7**, the complex gained singlet-singlet transitions in the visible region of the electromagnetic spectrum, at 427 nm and 421 nm. The calculated shift of **8** is less pronounced (first singlet-singlet transition at 396 nm). This behaviour can be explained by a decrease of orbital energy of the metal-centred orbital (LUMO+1 in **7’**), which becomes LUMO in **7**. Accordingly, this results in a bathochromic shift of the entire spectrum, which is more pronounced in **7** than **8**, now according to the expected periodic table trend.

In **7**, the ordering of the transitions does not change, although the contribution of HOMO and HOMO−1 to the first two electronic transitions becomes near degenerate. LUMO of **8** remains delocalized across the 2-picolinate ligand. Surprisingly, according to the calculated results, the lowest energy transition now corresponds to a HOMO → LUMO+1 transition, followed by HOMO−1 → LUMO+1 and only then by the HOMO → LUMO transition. This behaviour, although puzzling at first glance, can be rationalized by the differences between DFT (by which the Kohn-Sham molecular orbitals are calculated) and TD-DFT (by which the electronic transitions are calculated) approaches. The latter considers the response of the electronic structure to the change of electron density upon excitation, accounting for the reorganization energy necessary to accommodate the excited electron.

This reorganization energy would be presumably higher in a LLCT transition to the electron-rich 2-picolinate ligand compared to the observed LMCT transition to the electron-poor Hf^+.

Inclusion of scalar-relativistic spin-orbit coupling by the DKH approach reveals the impact of spin-forbidden singlet-triplet transitions on the shape of the measured absorption spectra. Based on the calculated results, the observed low-intensity band of **7** can be assigned to the first two singlet-triplet transitions at 474 nm and 466 nm. Both the calculated and the experimentally observed transitions are significantly separated from both the calculated spin-allowed transitions and the experimentally observed high-intensity band. The transitions are assigned to HOMO → LUMO and HOMO−1 → LUMO, respectively. An analogous result was obtained for **8**, with two singlet-triplet transitions at 433 nm and 429 nm.

Table 5: Selected calculated transition energies E and corresponding wavelength λ, oscillator strength f, molecular orbital assignment and assigned charge-transfer character, at ground state singlet geometry of **7'**, **8'** and **7**, **8**, optimized and calculated in implicit solvent model of dichloromethane.

	State	E cm^{-1}	λ nm	$f \times 10^4$	MO assignment			CT character			
7'	S1	26366	379	21	134	→	135	2× Cp*	→	L	(LLCT)
	S2	27686	361	37	133	→	135	2× Cp*	→	L	(LLCT)
	S3	28490	351	510	132	→	135	2× Cp*	→	L	(LLCT)
	S4	31448	318	74	131	→	135	2× Cp*	→	L	(LLCT)
8'	S1	25880	386	21	150	→	151	2× Cp*	→	L	(LLCT)
	S2	26904	372	39	149	→	151	2× Cp*	→	L	(LLCT)
	S3	27804	360	520	148	→	151	2× Cp*	→	L	(LLCT)
	S4	31160	321	100	147	→	151	2× Cp*	→	L	(LLCT)
7	T1	21103	474	0.24	124,125[a]	→	126	2× Cp*	→	M	(LMCT)
	T2	21461	466	0.033	124,125[b]	→	126	2× Cp*	→	M	(LMCT)
	S1	23424	427	16	124,125[c]	→	126	2× Cp*	→	M	(LMCT)
	S2	23702	422	190	124,125[d]	→	126	2× Cp*	→	M	(LMCT)
	S3	26057	384	13	123	→	126	2× Cp*	→	M	(LMCT)
	S4	27389	365	27	122	→	126	2× Cp*	→	M	(LMCT)
	S5	28238	354	22	125	→	127	2× Cp*	→	M	(LMCT)
	S6	28434	352	460	124	→	127	2× Cp*	→	M	(LMCT)
8	T1	23093	433	0.41	141	→	143	2× Cp*	→	M	(LMCT)
	T2	23294	429	2.8	140	→	143	2× Cp*	→	M	(LMCT)
	S1	25199	397	11	141	→	143	2× Cp*	→	M	(LMCT)
	S2	25780	388	110	140	→	143	2× Cp*	→	M	(LMCT)
	S3	26316	380	18	141	→	142	2× Cp*	→	L	(LLCT)
	S4	26774	374	83	140	→	142	2× Cp*	→	L	(LLCT)
	S5	27701	361	440	139	→	143	2× Cp*	→	M	(LMCT)
	S6	28265	354	33	138	→	143	2× Cp*	→	M	(LMCT)

Weight ratios [a]0.31:0.67, [b]0.67:0.31, [c]0.56:0.43, [d]0.43:0.56

4.2.6.2 Photophysical properties of 2-picolinate family

Neutral complexes **9'–11'** exhibit somewhat different properties from **7'** and **8'** (Table 6). The complexes have only high-energy, heavily crowded singlet-singlet transitions, of which first transitions correspond to 311 nm, 309 nm and 326 nm, respectively.

Inclusion of spin-orbit coupling yields singlet-triplet transitions which correspond to the experimentally observed shoulders of the dominant bands (Figure 59). These transitions are well defined due to their strong bathochromic shift in respect to singlet-singlet transitions, as previously observed in absorption spectra of **8** and **9**. Such transition can be found at 389 nm for **9'**, 390 nm in **10'** and 428 nm in **11'**. In **11'**, the energy of the first singlet-triplet absorption is somewhat underestimated, resulting in a bathochromic shift of the calculated transition in respect to the experimentally observed shoulder.

The first singlet-singlet transition of **9'** can be assigned to a HOMO−1 → LUMO transition, which corresponds to a LLCT transition of the highly delocalized π-orbitals of Cp* ligands to the 2-picolinate ligand. The transition is followed by a HOMO → LUMO transition, which has the same LLCT character. The unexpected ordering of transitions cannot be rationalized as easily as in **8**. The following HOMO−1 → LUMO+1 transition can be characterized as a LMCT transition. Transitions thereafter exhibit strong mixing. Nevertheless, all are found beyond the threshold of 300 nm. Singlet-triplet transitions of **9'** exhibit high mixing. The first transition which is responsible for the observed low-intensity peak corresponds to a HOMO−1 (w = 0.27), HOMO−2 (w = 0.32), HOMO−4 (w = 0.31) → LUMO transition.

Singlet-singlet transitions of **10'** also exhibit a high mixing, first of which can be attributed to HOMO (0.64), HOMO−1 (0.29) → LUMO transition and second to HOMO (0.25), HOMO−1 (0.64) → LUMO transition. It is evident that the reason behind these mixed contributions is separation of the calculated MO's into individual Cp* ligands, as opposed to a delocalized contribution of both Cp*. The LUMO is delocalized across the 2-pyridinolate ligand. The orbital assignment should therefore be interpreted as that of **9'**. Nevertheless, the result is interesting, as it suggests that even upon numerical separation of the MO's, the transition originates from a delocalized orbital to which both Cp* significantly contribute. The significant first singlet-triplet transition is mixed, corresponding to a HOMO (w = 0.22), HOMO−1 (w = 0.29), HOMO−2 (w = 0.17), HOMO−4 (w = 0.23) → LUMO transition.

Singlet-singlet transitions of **11**' are well ordered. The first two transitions correspond to HOMO → LUMO and HOMO−1 → LUMO, which are assigned analogously to **10**' and **9**'. Later transitions are of mixed character and beyond the 300 nm threshold. The significant first singlet-triplet transition is mixed, corresponding to a HOMO ($w = 0.40$), HOMO−2 ($w = 0.26$), HOMO−4 ($w = 0.28$) → LUMO transition.

Cationic species **9**, **10** and **11** exhibit a bathochromic shift of singlet-singlet transition to their respective precursors. The visible and the UV-A region of the electromagnetic spectrum now includes five singlet-singlet transitions per each complex. The calculated first singlet-singlet transitions correspond to 432 nm, 440 nm and 436 nm respectively. The first two transitions are near-degenerate, as previously of **8** and **9**. The calculation suggests a possible contribution of singlet-triplet transitions to the final shape of the absorption spectra. However, the calculation does not account for their unusually high intensity.

Cationic formation decreases the orbital energy of the zirconium-localized unoccupied orbitals, which represent the LUMO in **9**–**11**. The first singlet-singlet transitions of **9**–**11** correspond to a HOMO → LUMO transition and are followed by HOMO−1 → LUMO,… HOMO−4 → LUMO, only thereafter followed by a HOMO → LUMO+1 transition. All 5 occupied orbitals were assigned to delocalized π-electrons of Cp* , in some cases with partial overlap across the 2-pyridinolate ligand. LUMO+1 of **9**–**11** is delocalized across the 2-pyridinolate ligand. The first calculated singlet-triplet transition is a HOMO → LUMO+1 transition in **10**, **11** and HOMO → LUMO in **9**. The second transition *vice versa*.

Table 6: Selected calculated transition energies *E* and corresponding wavelength *λ*, oscillator strength *f,* molecular orbital assignment and assigned charge-transfer character, at ground state singlet geometry of **9’–11’** and **9–11**, optimized and calculated in implicit solvent model of dichloromethane.

	State	E cm^{-1}	λ nm	$f\times10^4$	MO assignment			CT character			
9’	T1	25700	389	3.2×10^{-3}	123,125, 126	→	128	mixed			
	T2	29482	339	0.14	127 126, 125	→ →	129 128	2× Cp* 2× Cp	→ →	M L	(LMCT) (LLCT)
	S1	32206	311	91	126	→	128	2× Cp*	→	L	(LLCT)
	S2	32308	310	25	127	→	128	2× Cp*	→	L	(LLCT)
	S3	33384	300	110	126	→	129	2× Cp*	→	M	(LMCT)
10’	T1	25631	390	3.1×10^{-3}	127,129, 130,131	→	132	mixed			
	T2	29125	343	5.8×10^{-2}	130,131	→	133	2× Cp*	→	M	(LMCT)
	S1	32348	309	520	130,131	→	132	2× Cp*	→	L	(LMCT)
	S2	32761	305	57	130,131	→	132	2× Cp*	→	L	(LLCT)
	S3	33375	300	210	130,131	→	133	2× Cp*	→	M	(LMCT)
11’	T1	23369	428	3.1×10^{-3}	127,129, 131	→	132	mixed			
	T2	28929	346	6.0×10^{-2}	131 130	→ →	132 133	2× Cp* 2× Cp*	→ →	L M	(LLCT) (LMCT)
	S1	30748	325	89	131	→	132	2× Cp*	→	L	(LLCT)
	S2	31053	322	29	130	→	132	2× Cp*	→	L	(LLCT)
	S3	32738	306	530	130 129	→ →	133 132	2× Cp* 2× Cp*	→ →	M L	(LMCT) (LLCT)
9	T1	20602	485	0.28	118	→	119	2× Cp*, L	→	M	(LMCT)
	T2	21267	470	6.3×10^{-2}	117	→	119	2× Cp*	→	M	(LMCT)
	S1	23096	433	140	118	→	119	2× Cp*, L	→	M	(LMCT)
	S2	23234	430	62	117	→	119	2× Cp*, L	→	M	(LMCT)
	S3	25364	394	18	116	→	119	2× Cp*, L	→	M	(LMCT)
10	T1	20382	491	0.31	121	→	123	2× Cp*	→	M	(LMCT)
	T2	20948	477	5.2×10^{-2}	122	→	123	2× Cp*,L	→	M	(LMCT)
	T3	22975	435	80	118,120	→	123	2× Cp*, L	→	M	(LMCT)
	S1	22731	439	24	122	→	123	2× Cp*, L	→	M	(LMCT)
	S2	23030	434	120	121	→	123	2× Cp*	→	M	(LMCT)
	S3	24986	400	14	120	→	123	2× Cp*, L	→	M	(LMCT)
11	T1	20614	485	0.31	121	→	123	2× Cp*	→	M	(LMCT)
	T2	20933	478	2.1×10^{-2}	122	→	123	2× Cp*, L	→	M	(LMCT)
	T3	23433	427	18	118, 120	→	123	2× Cp*, L	→	M	(LMCT)
	S1	22906	437	127	122	→	123	2× Cp*, L	→	M	(LMCT)
	S2	22909	437	54	121	→	123	2× Cp*	→	M	(LMCT)
	S3	25032	400	15	120	→	123	2× Cp*, L	→	M	(LMCT)

4.2.6.3 Photophysical properties of 2-pyridinemethanolate complexes

Complexes **12’** and **12’** were computationally investigated as per the previous sections (Table 7). Complex **12’** has only one singlet-singlet transition above 300 nm, at 322 nm. The transition corresponds well to an experimentally observed band.

The less intense, broad shoulder band may be interpreted as 1) the calculated singlet-triplet transition, 2) singlet-triplet transitions of conformers/coordination isomer of **12’**.

First singlet-singlet transition of **12’** corresponds to a HOMO → LUMO transition and is followed by transitions which correspond to HOMO−1 → LUMO and HOMO−2 → LUMO. All of the aforementioned transitions can be assigned as LMCT transitions of Cp*. Later transitions are mixed and already beyond the 300 nm threshold. The significant first singlet-triplet transition corresponds to a HOMO → LUMO transition.

Table 7: Selected calculated transition energies *E* and corresponding wavelength λ, oscillator strength *f*, molecular orbital assignment and assigned charge-transfer character, at ground state singlet geometry of **12’** and **12**, optimized and calculated in implicit solvent model of dichloromethane.

	S_n	E cm^{-1}	λ nm	$f\times10^4$	MO assignment	CT character
12’	T1	28676	349	2.7×10^{-2}	131 → 132	2× Cp* → M (LMCT)
	S1	31078	322	59	131 → 132	→ M (LMCT)
	S2	33081	302	11	130 → 132	2× Cp* → M (LMCT)
	S3	33717	297	270	129 → 132	2× Cp* → M (LMCT)
12	T1	21266	470	2.2×10^{-2}	121 → 123	2× Cp* → M (LMCT)
	T2	22487	445	0.25	122 → 123	2× Cp* → M (LMCT)
	S1	23126	432	4.5	122 → 123	2× Cp* → M (LMCT)
	S2	25106	398	206	121 → 123	2× Cp* → M (LMCT)
	S3	27514	363	26	120 → 123	2× Cp* → M (LMCT)
	S4	28142	355	84	122 → 124	2× Cp* → L LLCT
	S5	28371	353	39	119 → 123	2× Cp* → M (LMCT)
	S6	30329	330	93	121 → 124	2× Cp* → L (LLCT)

Cation **12** has bathochromically shifted transitions in respect to the neutral **12’**. The first singlet-singlet transition lies at 432 nm, followed by a strong transition at 398 nm. These correspond to the first experimentally observed band. The second experimentally observed band is also in agreement with the calculated transitions at 364 nm, 355 nm, 352 nm and 330 nm. Starting by 304 nm, transitions become highly crowded. Calculated singlet-triplet transitions at 470 nm and 445 nm may contribute to the broadening of the first band. However, the assignment is not clear due to the adjacent singlet-singlet transition at 432 nm.

First three singlet-singlet transitions of **12** correspond to HOMO → LUMO, … HOMO−2 → LUMO, followed by a HOMO → LUMO+1 transition. Fifth and sixth transitions correspond to a HOMO−3 →

LUMO and HOMO−1 → LUMO+1 transitions. All four occupied orbitals correspond to π-orbitals of Cp*, partially delocalized across the 2-methanolate ligand. LUMO is well localized on the central atom, whereas LUMO+1 is a predominantly ligand-centred orbital with weak mixing of the central atom. First four calculated singlet-triplet transitions follow the assignment of the singlet-singlet transitions.

4.2.6.4 Photophysical properties of 8-quinolinolate complexes

Complexes **13’** and **13** were computationally investigated as per the previous sections (Table 8). Neutral complex **13’** differs from the previously discussed neutral species by a strong, calculated singlet-singlet transition in the visible region of the electromagnetic spectrum, at 438 nm. This transition is followed by three well separated transitions at 375 nm, 356 nm and 332 nm, only then followed by highly crowded transitions, starting by 319 nm. The calculated singlet-singlet transitions are bathochromically shifted off-centre of the measured absorption bands. They do however correspond to the observed spectral patterns. The calculated transitions contain a singlet-triplet transition at 602 nm, which is not observed in the measured spectrum.

First three singlet-singlet transitions of **13’** correspond HOMO → LUMO, HOMO−1 → LUMO and HOMO−2 → LUMO. The LUMO of **13’** is delocalized across the 8-quinolinolate ligand. The lowest occupied orbitals can be assigned to the delocalized π-orbitals of Cp* of which HOMO is also partially delocalized across the 8-quinolinolate ligand. The discussed first singlet-triplet transition corresponds to a HOMO → LUMO transition.

Calculated transitions of cationic complex **13** differ from **13’** by an additional weak transition at 478 nm, followed by an intense transition at 425 nm. These are followed by transitions at 410 nm, 377 nm, 363 nm, 354 nm, 350 nm and crowded high-energy transitions starting by 322 nm. The first of these transitions is well replicated in the experimentally obtained spectrum by a non-Gaussian shaped slope of the first experimentally observed band. The spectrum thereafter resembles the characteristics of the neutral **13’**, albeit exhibiting a much lower extinction coefficient, which is not accounted for in the calculated results. A well separated singlet-triplet transition was found, now at 590 nm, which was not found in the measured absorption spectrum.

The first five calculated singlet-singlet transitions of **13** are well-behaved and correspond to HOMO → LUMO, HOMO → LUMO+1, HOMO−1 → LUMO, HOMO−2 → LUMO and HOMO−3 → LUMO. The HOMO corresponds to a strongly delocalized orbital with mixed Cp* and 8-quinolinolate character. The remaining discussed occupied orbitals correspond to orbitals primarily localized on the Cp*. LUMO and LUMO+1 are well localized on zirconium and the 8-quinolinolate ligand, respectively. Discussed singlet-triplet transitions correspond to a predominantly HOMO → LUMO+1 transition and a HOMO → LUMO transition, respectively.

Table 8: Selected calculated transition energies E and corresponding wavelength λ, oscillator strength f, molecular orbital assignment and assigned charge-transfer character, at ground state singlet geometry of **13’** and **13**, optimized and calculated in implicit solvent model of dichloromethane.

	State	E cm^{-1}	λ nm	f	MO assignment			CT character			
13’	T1	16618	602	1.1×10^{-3}	140	→	141	2× Cp*, L	→	L	(LLCT)
	S1	22830	438	690	140	→	141	2× Cp*, L	→	L	(LLCT)
	S2	26607	376	16	139	→	141	2× Cp*	→	L	(LLCT)
	S3	28084	356	220	138	→	141	2× Cp*	→	L	(LLCT)
	S4	30134	332	77	140	→	143	2× Cp*, L	→	M, L	(LMCT, LLCT)
	S5	31611	316	110	136	→	141	2× Cp*, L	→	L	(LLCT)
13	T1	16925	591	8.9×10^{-4}	131	→	133	2× Cp*, L	→	L	(LLCT)
	S1	20878	479	7	131	→	132	2× Cp*, L	→	M	(LMCT)
	S2	23530	425	649	131	→	133	2× Cp*, L	→	L	(LLCT)
	S3	24314	411	195	130	→	132	2× Cp*	→	M	(LMCT)
	S4	24563	407	94	129	→	132	2× Cp*	→	M	(LMCT)
	S5	26502	377	17	128	→	132	2× Cp*	→	M	(LMCT)

4.2.6.5 Excited-state triplet emission of **7–13**

The measured triplet transition was modelled by investigating singlet-triplet transitions at lowest-energy triplet optimized geometry using methods discussed in 4.1.5. The method yields good estimates of emission wavelength for **8–12**. Significant deviation can be found in calculations of emission wavelength of **7** and **13**.

It can be hypothesised that the emission of **7** is perturbed by solid-state dimerization observed in structures of **7’** and **7** obtained by X-ray diffraction (Figure 51). These dimers may lead to formation of excimers which would result in a shift of the emission spectrum.

The deviation in **13** can be attributed to the localization of the calculated transition. Whereas the orbital assignment of emission of **7–12** is analogous to first singlet-singlet transitions, emission of **13** is localized on the 8-quinolinolate ligand. The second calculated singlet-triplet transition of **13** is a LMCT transition which corresponds to a wavelength of 558 nm. Based on this result, it may be hypothesised that intersystem-crossing may yield a light and a dark state triplet state, suggesting anti-Kasha behaviour. However, this hypothesis is yet to be investigated experimentally.

Table 9: Calculated first singlet-triplet transition energies *E* and corresponding wavelength *λ* of lowest-energy triplet optimized geometries of **7–13** and **9h2o**, optimized and calculated under vacuum conditions.

	E cm^{-1}	*λ* nm
7	19085	524
8	19131	523
9	18212	549
9h2o	19724	507
10	18102	552
11	17555	570
12	18298	547
13	10646	939
	17910[a]	558[a]

[a]Second calculated singlet-triplet transition.

4.3 'Half-sandwich' complex 14

The afore-mentioned air-sensitivity of cationic metallocene complexes **7–13** prompted the group to search for alternatives to their molecular design which would be more suitable for photophysical measurements and photoredox catalysis. One strategy of doing so involves substituting one of the Cp* for a second *N,O*-chelating ligand. 8-quinolinolate was the candidate ligand for the realization of this concept, yielding **14**. Such complex would presumably exhibit strong absorption in the visible region without the requirement of positive charge on the central atom, owing to the 8-quinolinolate ligand, as seen in **13'** and **13** (Figure 58).

4.3.1 Preparation of the 'half-sandwich' metallocene complex 14

Complex **14** was prepared by a reaction of 2.5 equivalents of sodium 8-oxoquinoline with (pentamethylcyclopentadienyl)zirconium(IV) trichloride, using the same procedure and reaction conditions as for preparation of neutral metallocene complexes discussed in (4.2.1). A full discussion of the NMR spectra is not warranted, as the spectra followed a very similar pattern to **13** and **13'**.

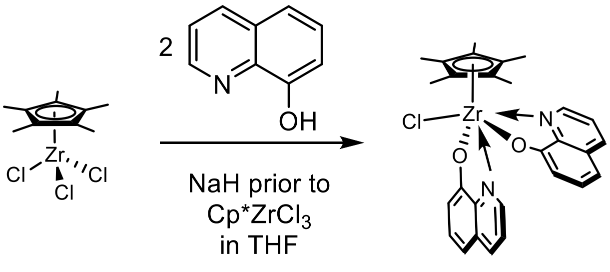

Figure 61: Preparation of 'half-sandwich' complex **14**.

4.3.2 X-ray diffraction analysis of **14**

Complex **14** was investigated by single-crystal X-ray diffraction analysis. Determined molecular structure of the studied compound is in agreement with the expected product.

Molecular geometry of **14** exhibits a pseudo-octahedron geometry around the central atom (if one were to interpret C_5Me_5 as a single ligand). The two 8-oxoquinoline ligands are oriented near-perpendicular. Molecular packing is facilitated by parallel-displaced π-stacking of the quinoline ligands and T-shape stacking.

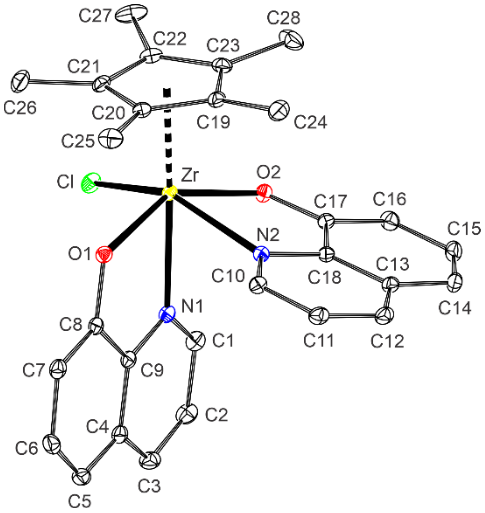

Figure 62: Molecular structure of **14** with thermal displacement ellipsoids at 30% probability level and hydrogen atoms omitted for clarity.

4.3.3 Photophysical properties of **14**

Absorption spectra of **14** were measured in dichloromethane solution. An intense (10^4) absorption band was found bordering the visible region of the spectra. Spectra are analogous to **13**. Interestingly, **14** exhibits significant luminescence in dichloromethane solution at 540 nm. The luminesce is short lived, suggesting emission from a singlet excited state. The luminescence lifetime did not allow for a time-resolved measurement by the available experimental setup.

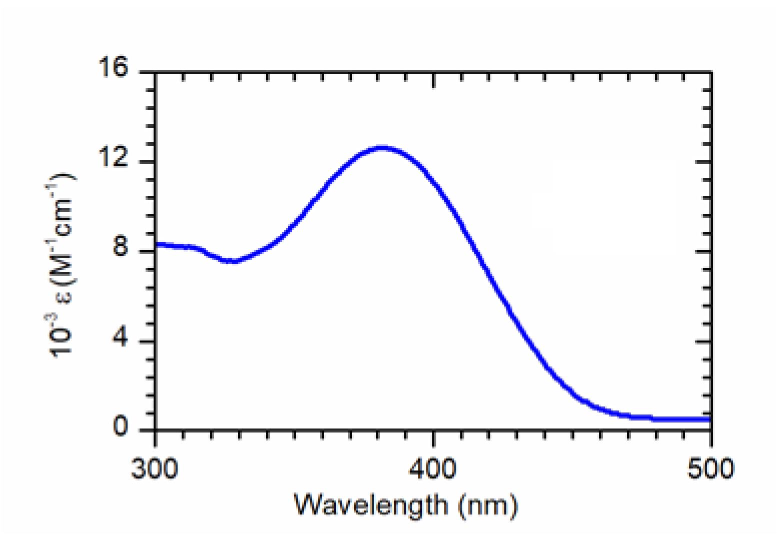

Figure 63: UV-VIS absorption spectra of **14**, measured in dichloromethane solution.

4.3.4 Computational investigation of photophysical phenomena of **14**.

Interestingly, **14** exhibits somewhat different transitions from the previously discussed compounds. The border of the visible spectrum is populated by calculated singlet-singlet transitions. The calculated transitions are bathochromically shifted off-centre of the measured absorption maxima in solution. Transitions are well characterized, following in order HOMO → LUMO, HOMO−1 → LUMO, HOMO−2 → LUMO and then only HOMO → LUMO+1.

Interestingly, unlike in previous compounds, only LUMO+3 and higher exhibit significant metal character. All experimentally observed transitions correspond to transitions between a molecular orbital delocalized across Cp* and the equatorial 8-quinolinolate, whereas LUMO and LUMO+1 are delocalized across both equatorial and axial 8-quinolinolate. It appears that LMCT is unfavourable in **14**, supporting the hypothesis that the observed luminescence originates from a ^{1}LLCT excited state.

Table 10: Selected calculated transition energies *E* and corresponding wavelength *λ*, oscillator strength *f*, molecular orbital assignment and assigned charge-transfer character, at ground state singlet geometry of **14**, optimized and calculated in implicit solvent model of dichloromethane.

	State	*E* cm^{-1}	*λ* nm	*f*	MO assignment			CT character			
14	S1	23308	429	540	140	→	141	Cp*, L	→	L,L’	(LLCT)
	S2	25346	395	470	139	→	141	L’	→	L,L’	(LLCT)
	S3	26439	378	220	138	→	141	Cp*	→	L,L’	(LLCT)
	S4	27024	370	69	140	→	142	Cp*, L	→	L,L’	(LLCT)
	S5	28511	351	29	137	→	141	Cp*, L	→	L,L’	(LLCT)
	S6	28650	349	380	139	→	142	Cp*, L	→	L,L’	(LLCT)
	S7	30085	332	57	138	→	142	Cp*, L	→	L,L’	(LLCT)

L = equatorial 8-quinolinolate, L’ = axial 8-quinolinolate

4.4 Photoredox catalysis

A photocatalytic study was conducted in a limited scope as a *proof-of-concept* of the photocatalytic properties of studied metallocene complexes. **1** and **14** were selected as representatives of their respective structure types, since they exhibited the most promising stability upon exposure to various solvents and air (in solid form) and also luminescence, indicating a possible productive excited state. Unfortunately, none of the complexes with *N,O*-chelating ligands were suitable for applications in photoredox catalysis due to their high sensitivity.

The catalysts were probed by a single model reaction, reduction of bromopentafluorobenzene. The reaction is convenient as it typically does not proceed without the presence of a photocatalyst and the observed yields match the conversion of the reaction in literature.[54] The catalyst was used in a 0.1 molar ratio. 3 equivalents of DIPEA (to substrate) were added as a sacrificial electron donor (DIPEA was previously reported in photocatalytic reactions of titanocene dichloride). The reactions were carried out in dichloromethane and the reaction mixture was irradiated by a 4W 400 nm LED. Both reactions were performed in duplicates and resulted in a 100% conversion after 8 hours of irradiation, determined by ^{19}F NMR.

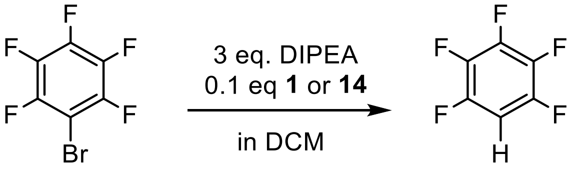

Figure 64: Reaction scheme of photocatalyzed reduction of bromopentafluorobenzene by **1** and **14**.

To conclude that the reaction was truly photocatalyzed by the proposed photocatalysts, three control experiments were carried out: without 1) DIPEA, 2) catalyst, 3) light. In all cases, product was not detected by ^{19}F NMR.

Table 11: Conversion of catalytic experiments by components included.

Catalyst	DIPEA	Light	Conversion
yes	yes	yes	~100%[a]
yes	yes	no	~0%[b]
yes	no	yes	~0%[b]
no	yes	yes	~0%[b]

[a] ^{19}F NMR Signals of reactant not observed, [b] ^{19}F NMR signals of product not observed.

5 Conclusions

In summary, target neutral and cationic group 4 metallocene complexes were prepared by the proposed methods (Figure 33). All compounds were characterized by ^{1}H and ^{13}C NMR spectroscopy. ^{19}F NMR spectra were measured where adequate (**1–13**, **11’**). Solid-state structures of compounds **1’**, **5’**, **7’–12’**, **1–11**, **13** and **14** were determined by X-ray diffraction analysis. Collected data revealed formation of an unexpected coordination isomer **12’**.

UV-VIS spectra of compounds **1’**, **5’**, **1’–13’** and **1–14** were measured in solution and revealed enhanced absorption of the cationic species in the visible region in comparison to their neutral precursors, with the exception of **13**’ and **13**. The behavior of the **13’**, **13** pair will be further investigated, as it is in this respect anomalous. TD-DFT calculations were applied to assign the measured electronic spectra. The transitions followed the periodic table trends in structurally related compounds with different central atoms in cases where LMCT was involved (in **1**, **3**, **4** and **7**, **8**), which manifested as a bathochromic shift of the first absorption bands in order of Hf < Zr < Ti. In addition, hydrolytic product **9h2o** was prepared and characterized. It was demonstrated that hydrolysis of **9** results in a significant hypsochromic shift of the visible absorption band and emission wavelength, which was empirically observed for **7**–**12** as well.

Emission of **1’**, **5’**, **1**–**14** was investigated in dichloromethane solutions (**1’**, **5’**, **1**–**6**, **14**) and in solid-state samples (**7**–**13**). It was found that the cationic species **1**–**13** and neutral complex **5’** exhibit solid-state room-temperature luminescence in the range of 510-616 nm. The same behavior was observed in dichloromethane solutions in which the emission wavelengths were shifted by ~20 nm. Same periodic table trends were observed for emission wavelengths of structurally analogous Ti, Zr, Hf species as in absorption spectra. Quantum yields of luminescence of **5’**, **1**–**9** and **12** were measured in solid state, yielding up to 58% (**1**) and for **5’**, **1–6** also in dichloromethane solution, yielding up to 40% (**5**). The quantum yields were in all cases lower in dichloromethane solutions

Luminescence kinetics of **1’**, **5’**, **1–6** were measured in dichloromethane solutions. The determined luminescence life-times in argon-saturated solutions were in all cases in order of 10 μs. Luminescence was efficiently quenched by oxygen, with quantum yield of singlet oxygen reaching up to 77% (**1**). Luminescence kinetics of **7–13** were measured in solid-state samples. Luminescence lifetimes were in all cases also in order of 10 μs. **9** exhibited two emission maxima, which suggests partial hydrolysis in the solid state. The compound should therefore be remeasured in the future. Emission of compounds **1**–**13** and **5’** was attributed to emission from ^{3}LMCT excited states.

‘Half-sandwich’ complex **14** was prepared with the aim of mitigating the moisture-sensitivity of cationic complexes. **14** exhibited similar absorption properties to **13’**, which was attributed to ^{1}LLCT transitions. **14** also exhibited room-temperature luminescence in dichloromethane solution at 542 nm.

Compounds **1** and **14** were screened as photoredox catalysts in a model reaction of reduction of bromopentafluorophenylbenzene. Both photocatalysts catalyzed the reaction with a conversion rate ~100%. Product was not observed in control experiments.

Some of the research done on **1’**, **5’**, **1**–**6** was published as an article in a peer-reviewed journal.[82] Remaining data is a subject of a prepared manuscript. Results obtained for compounds **7’**–**13’** and **7**–**13** require reinvestigation of the X-ray structures of **12** and possibly **13’**, as well as reinvestigation of emission kinetics of **9**. Efforts will be made to solve the technical difficulties of measuring luminescence kinetics in solution. Photocatalytic properties of **1** and **14** will be further investigated on a wider range of substrates.

6 Experimental section

6.1 Applied techniques, chemicals and materials

All operations were carried out with the exclusion of air and moisture under an argon atmosphere using Schlenk techniques or in a glovebox Labmaster 130 (mBraun) under purified nitrogen, unless otherwise described. All solvents (including deuterated) were appropriately dried: tetrahydrofuran (THF), diethyl ether, *n*-pentane, *n*-hexane, and dichloromethane were purified by a solvent purification system (PureSolv MD 7; Innovative Technology, Inc.). Chlorobenzene, dichloromethane-d_2, bromobenzene-d_5 and MeCN-d_3 were refluxed with CaH_2, then distilled under argon and stored over 4 Å molecular sieves. Other chemicals were used as received from commercial vendors.

^{1}H (300.0 MHz), ^{13}C (75.4 MHz), and ^{19}F (282.2 MHz) NMR spectra were measured on a Varian Unity 300 spectrometer at 293 K. Chemical shifts (δ/ppm) are given relative to solvent signals (C_6D_5Br: δH 7.30, δC 122.54; $CDCl_3$: δH 7.26, δC 77.16; CD_3CN: δH 1.94, δC 1.32), ^{19}F NMR spectra were referenced to an external reference ($C_6H_5CF_3$ at −63.72 ppm). The assignment of NMR signals is based on 1D-NOESY, gCOSY, gHSQC, and gHMBC experiments, wherever possible. Elemental analyses were performed on a FLASH 2000 CHN elemental analyzer (Thermo Scientific). Melting points were determined on a Kofler apparatus, samples were sealed in glass capillaries under nitrogen.

6.2 Synthesis

Complexes **1'–6', 1–6** were prepared according to previously reported procedures.[82-83] Remaining synthesis are reported herein.

6.2.1 Preparation of neutral complexes

6.2.1.1 General procedure for preparation of neutral metallocene complexes **7'–13'**

Neutral metallocene complexes were prepared by adding bis(pentamethyl)zirconium(IV) dichloride and 1.2 molar equivalents of sodium salt of *N,O*-chelating ligand (solids) to a dried 250 ml Schlenk flask equipped with a magnetic stir bar, in glovebox. The flask was then transported to a Schlenk line, where its contents were flushed by argon. 60 mL of THF were added under argon atmosphere, resulting in a colourless (**8'–11'**), faint-yellow (**7'**, **12'**), yellow (**13'**) solution with solid, off-white participate, which was left stirring for a week.

All complexes were isolated by distilling the solvent *in vacuo* and extracting the solid residue by 3× 25 mL of toluene into a long, 50 mL Schlenk flask. Toluene was distilled from the isolated toluene phase *in vacuo.* The solid residue was dissolved in minimal amount of dichloromethane and carefully covered by an excess of *n*-hexane. The mixture was left to crystalize for one week, at room temperature and thereafter one week at −24 °C, yielding colourless (**8'–11'**), faint-yellow (**7'**, **12'**) and yellow (**13'**) crystals.

6.2.1.2 Preparation of **7’**

This compound was prepared from $Cp^*{}_2ZrCl_2$ (445 mg, 1.03 mmol) and sodium 2-picolinate (182 mg, 1.25 mmol). The product was obtained as faint-yellow crystals. Yield: 342 mg (64%).

M.p decomposed at 266 °C. ^{1}H NMR (300 MHz, $CDCl_3$): δ 9.50, 8.27, 7.99, 7.49 (4× m, 1H, C_5H_4N C*H*), 1.72 (s, 30H, $C_5\mathit{Me}_5$) ppm. $^{13}C\{^1H\}$ NMR (75 MHz, $CDCl_3$): δ 166.5 (*C*OO), 152.5 ($C_5\mathit{H}_4N$ C_{ipso}), 152.4, 140.4, 126.5, 125.5 (4× C_5H_4N *C*H), 121.9 (C_5Me_5), 11.7 ($C_5\mathit{Me}_5$) ppm. Anal. Calcd. for $C_{26}H_{34}ZrClO_2N$ (M_r = 519.23): C 60.14, H 6.60, N 2.70%. Found: C 60.08, H 6.64, N 2.77%.

6.2.1.3 Preparation of **8’**

This compound was prepared from $Cp^*{}_2HfCl_2$ (330 mg, 0.63 mmol) and sodium 2-picolinate (118 mg, 0.81 mmol) The product was obtained as colourless crystals. Yield: 312 mg (81%).

M.p. 227 °C. ^{1}H NMR (300 MHz, $CDCl_3$): δ 9.59, 8.30, 8.03, 7.55 (4× m, 1H, C_5H_4N C*H*), 1.82 (s, 30H, $C_5\mathit{Me}_5$) ppm. $^{13}C\{^1H\}$ NMR (75 MHz, $CDCl_3$): δ 166.8 (*C*OO), 152.3 (C_5H_4N *C*H), 152.1 (C_5H_4N C_{ipso}), 140.4, 126.7, 125.4 (3× C_5H_4N *C*H), 120.3 (C_5Me_5), 11.8 ($C_5\mathit{Me}_5$) ppm. Anal. Calcd. for $C_{26}H_{34}HfClO_2N$ (M_r = 606.49): C 51.49, H 5.65, N 2.31%. Found: C 51.57, H 5.73, N 2.36%.

6.2.1.4 Preparation of **9’**

This compound was prepared from $Cp^*{}_2ZrCl_2$ (294 mg, 0.68 mmol) and sodium 2-pyridinolate (95 mg, 0.81 mmol). The product was obtained as colourless crystals. Yield: 230 mg (69%).

M.p. 138 °C. ^{1}H NMR (300 MHz, $CDCl_3$): δ 7.98, 7.44, 6.39, 6.25 (4× m, 1H, C_5H_4N C*H*), 1.79 (s, 30H, $C_5\mathit{Me}_5$) ppm. $^{13}C\{^1H\}$ NMR (75 MHz, $CDCl_3$): δ 171.0 (*C*O), 145.0, 141.6 (2× C_5H_4N *C*H), 120.8 (C_5Me_5), 111.6, 110.5 (2× C_5H_4N *C*H), 11.6 ($C_5\mathit{Me}_5$) ppm. Anal. Calcd. for $C_{25}H_{34}ZrClON$ (M_r = 491.22): C 61.13, H 6.98, N 2.85%. Found: C 61.18, H 6.94, N 2.84%.

6.2.1.5 Preparation of **10’**

This compound was prepared from $Cp^*{}_2ZrCl_2$ (516 mg, 1.19 mmol) and sodium 5-methyl-2-pyridinolate (194 mg, 1.48 mmol).The product was obtained as colourless crystals. Yield: 373 mg (62%).

M.p. 165−167 °C. ^{1}H NMR (300 MHz, $CDCl_3$): δ 7.26, 6.19, 6.12 (3× m, 1H, C_5H_4N C*H*), 2.65 (s, 3H, $C_5H_3N\mathit{Me}$), 1.83 (s, 30H, $C_5\mathit{Me}_5$) ppm. $^{13}C\{^1H\}$ NMR (75 MHz, $CDCl_3$): δ 170.6 (*C*O), 158.1 (C_5H_3NMe *C*Me), 139.4 ($C_5\mathit{H}_3NMe$ *C*H), 121.2 (C_5Me_5), 111.5, 108.7 (2× C_5H_3N *C*H), 24.1 ($C_5H_3N\mathit{Me}$), 11.6 ($C_5\mathit{Me}_5$) ppm. Anal. Calcd. for $C_{26}H_{36}ZrClON$ (M_r = 505.25): C 61.81, H 7.18, N 2.77%. Found: C 61.77, H 7.13, N 2.78%.

6.2.1.6 Preparation of **11’**

This compound was prepared from $Cp^*{}_2ZrCl_2$ (207 mg, 0.48 mmol) and sodium 5-fluoro-2-pyridinolate (82 mg, 0.61 mmol). The product was obtained as colourless crystals. Yield: 180 mg (74%).

M.p. 227 °C. ^{1}H NMR (300 MHz, $CDCl_3$): δ 8.13, 6.72, 5.86 (3× m, 1H, C_5H_4N C*H*), 1.73 (s, 30H, C_5*Me*$_5$) ppm. $^{13}C\{^1H\}$ NMR (75 MHz, $CDCl_3$): δ 168.2 (*C*O), 153.4 (C_5H_3NF *C*F), 130.9, 130.8 (2× C_5H_3N *C*H), 120.7 (*C*$_5$Me$_5$), 111.8 (*C*$_5$Me$_5$), 11.6 (C_5*Me*$_5$) ppm. ^{19}F NMR (282 MHz, $CDCl_3$): δ −144.3 (C_5H_3NF) ppm. Anal. Calcd. for $C_{25}H_{33}ZrClONF$ (M_r = 509.21): C 58.97, H 6.53, N 2.75%. Found: C 58.98, H 6.44, N 2.74%.

6.2.1.7 Preparation of **12’**

This compound was prepared from $Cp^*{}_2ZrCl_2$ (361 mg, 0.83 mmol) and sodium 2-pyridinemethanolate (141 mg, 1.08 mmol). The product was obtained as faint-yellow crystals. Yield: 177 mg (42%).

M.p. 185–186 °C. ^{1}H NMR (300 MHz, $CDCl_3$): δ 8.45, 7.69, 7.47, 7.10 (4× m, 1H, C_5H_4N C*H*), 5.36 (s, 2H, C*H*$_2$O), 1.94 (s, 30H, C_5*Me*$_5$) ppm. $^{13}C\{^1H\}$ NMR (75 MHz, $CDCl_3$): δ 163.2 (C_5H_4N C_{ipso}), 148.3, 136.8 (2× C_5H_3N *C*H), 121.5 (*C*$_5$Me$_5$), 121.2 (C_5H_3N *C*H), 73.3 (*C*H$_2$O), 11.6 (C_5*Me*$_5$) ppm. Anal. Calcd. for $C_{26}H_{36}ZrClON$ (M_r = 505.25): C 61.81, H 7.18, N 2.77%. Found: C 61.84, H 7.19, N 2.81%.

6.2.1.8 Preparation of **13’**

This compound was prepared from $Cp^*{}_2ZrCl_2$ (388 mg, 0.90 mmol) and 8-hydroxyquinoline (180 mg, 1.08 mmol). The product was obtained as yellow crystals. Yield: 281 mg (58%).

M.p. 206–208 °C. ^{1}H NMR (300 MHz, $CDCl_3$): δ 9.54, 8.16, 7.40, 7.36, 6.93, 6.87 (6× m, 1H, C_9H_6N C*H*), 1.74 (s, 30H, C_5*Me*$_5$) ppm. $^{13}C\{^1H\}$ NMR (75 MHz, $CDCl_3$): δ 163.8 (*C*O), 151.5 (C_9H_6N *C*H), 145.0 (C_9H_6N *C*), 138.8 (C_9H_6N *C*H), 130.3 (C_9H_6N *C*), 129.9 (C_9H_6N *C*H), 121.6 (C_9H_6N *C*H), 121.5 (*C*$_5$Me$_5$), 113.9 (C_9H_6N *C*), 110.4 (2× C_9H_6N *C*H), 11.8 (C_5*Me*$_5$) ppm. Anal. Calcd. for $C_{29}H_{36}ZrClON$ (M_r = 541.28): C 64.35, H 6.70, N 2.59%. Found: C 64.37, H 6.69, N 2.59%.

6.2.2 Preparation of cationic complexes **7–13**

6.2.2.1 General procedure for preparation of cationic metallocene complexes

Precautions: Both $Ph_3C[B(C_6F_5)_4]$ and the neutral metallocene precursor (solids) were added to a thoroughly dried 50 ml Schlenk flask (without magnetic stir bar), The flask was repeatedly and thoroughly degassed and flushed by argon after transporting back to the Schlenk line, as well as after adding each component as described later. All liquid components were added by a thoroughly dried Teflon cannula, with the exception of Et_3SiH, which was added by a thoroughly dried syringe, of which neither was reused. 5 mL of chlorobenzene were added to each flask. The flasks with the mixtures were stirred by hand until complete dissolvement.

Cationic complexes were prepared by adding 2 molar equivalents of Et_3SiH to a chlorobenzene solution of $Ph_3C[B(C_6F_5)_4]$, which was accompanied by loss of its original, orange-red colour, followed by adding 1 molar equivalent of neutral metallocene precursor, also as chlorobenzene solution, which in turn resulted in transient blood-red colour, eventually turned bright yellow upon stirring the flask by hand. The mixture was left to react for 15 minutes and occasionally stirred by hand.

The solvent was distilled from the reaction mixture *in vacuo*, after which the dry contents were dissolved again in minimal amount of chlorobenzene. The chlorobenzene solution was carefully covered by *n*-hexane and the mixture was left to crystallize for one week. Product was isolated as yellow (**7**–1**2**) or yellow-orange (**13**) crystals, by carefully removing all solvent by a thin Teflon cannula without a filter (to avoid introducing adsorbed moisture).

Note that upon formation of crystals, irradiation by UV-light can be used to monitor potential hydrolytic products, which typically exhibit bright green luminescence, which strongly contrasts the typically yellow luminescence of the cations (with the exception of **8**).

6.2.2.2 Preparation of **7**

This compound was prepared from **7'** (59 mg, 0.11 mmol), $Ph_3C[B(C_6F_5)_4]$ (109 mg, 0.12 mmol) and Et_3SiH (38 µL, 0.24 mmol). The product was obtained as yellow crystals. Yield: 122 mg (92%).

M.p. 335 °C. ^{1}H NMR (300 MHz, MeCN-d_3): δ 8.70 (m, 1H, C_5H_4N C*H*), 8.40-8.20 (m, 2H, C_5H_4N C*H*), 7.84 (m, 1H, C_5H_4N C*H*), 1.74 (s, 30H, C_5Me_5) ppm. $^{13}C\{^1H\}$ NMR (75 MHz, MeCN-d_3): 151.6, 143.5, 129.8, 127.6 (4× C_5H_4N *C*H), 124.2 (*C*$_5$Me$_5$), 11.6 (C_5Me_5) ppm. Signals of $B(C_6F_5)_4^-$: δ 149.0 (br d, J_{CF} = 236 Hz, *o*-C_6F_5), 139.3 (br d, J_{CF} = 247 Hz, *p*-C_6F_5), 137.3 (br d, J_{CF} = 243 Hz, *m*-C_6F_5) ppm. C_{ipso} of C_6F_5 and C_5H_4N and *C*OO were not observed. ^{19}F NMR (282 MHz, MeCN-d_3): δ −133.7 (*o*-C_6F_5), −163.9 (*p*-C_6F_5), −168.3 (*m*-C_6F_5) ppm. Anal. Calcd. for $C_{50}H_{34}F_{20}ZrO_2NB$ (M_r = 1162.81): C 51.64, H 2.95, N 1.20%. Found: C 51.62, H 2.96, N 1.22%.

6.2.2.3 Preparation of **8**

This compound was prepared from **8'** (44 mg, 0.073 mmol), $Ph_3C[B(C_6F_5)_4]$ (67 mg, 0.073 mmol) and Et_3SiH (23 µL, 0.15 mmol). The product was obtained as colourless crystals. Yield: 80 mg (88%).

M.p. 343 °C. ^{1}H NMR (300 MHz, MeCN-d_3): δ 8.72 (m, 1H, C_5H_4N C*H*), 8.31 (m, 2H, C_5H_4N C*H*), 7.87 (m, 1H, C_5H_4N C*H*), 1.80 (s, 30H, C_5Me_5) ppm. $^{13}C\{^1H\}$ NMR (75 MHz, MeCN-d_3): δ 151.6, 143.6, 130.0, 127.6 (4× C_5H_4N *C*H), 122.2 (*C*$_5$Me$_5$), 11.6 (C_5Me_5) ppm. C_{ipso} of C_5H_4N and *C*OO were not observed. Signals of $B(C_6F_5)_4^-$ in ^{13}C and ^{19}F spectra were the same as for compound **7.** Anal. Calcd. for $C_{50}H_{34}F_{20}HfO_2NB$ (M_r = 1250.08): C 48.04, H 2.74, N 1.12%. Found: C 48.01, H 2.72, N 1.12%.

6.2.2.4 Preparation of **9**

This compound was prepared from **9'** (51 mg, 0.10 mmol), $Ph_3C[B(C_6F_5)_4]$ (97 mg, 0.10 mmol) and Et_3SiH (33 µL, 0.21 mmol). The product was obtained as yellow crystals. Yield: 100 mg (85%).

M.p. 235 °C. ^{1}H NMR (300 MHz, MeCN-d_3): δ 7.70, 7.67, 6.71, 6.42 (4× m, 1H, C_5H_4N C*H*), 1.78 (s, 30H, C_5Me_5) ppm. $^{13}C\{^1H\}$ NMR (75 MHz, MeCN-d_3): δ 144.2, 143.7 (2× C_5H_4N *C*H), 123.1

(*C_5*Me$_5$), 113.8, 113.3 (2× C_5H_4N *C*H), 11.3 (C_5*Me*$_5$) ppm. *C$_{ipso}$* of C_5H_4N was not observed. Signals of $B(C_6F_5)_4^-$ in ^{13}C and ^{19}F spectra were the same as for compound **7**. Anal. Calcd. for $C_{49}H_{34}F_{20}ZrONB$ (*M*$_r$ = 1134.15): C 51.86, H 3.02, N 1.23%. Found: C 51.87, H 3.06, N 1.21%.

6.2.2.5 Preparation of **9h2o**

This compound was prepared by dissolving **9** (25 mg, 0.22 mmol) in 5mL of chlorobenzene in a 50 ml Schlenk flask, degassing the contents and flushing the flask with air. The product was isolated following the procedure of **7**–**13**, as colourless crystals. Yield: 22 mg (87 %).

M.p. 206–208 °C. ^1H NMR (300 MHz, $CDCl_3$): δ 12.57 (br s, 1H, N*H*), 7.95, 7.56, 6.96, 6.92 (4×m, 1H, C_5H_4N *C*H), 5.16 (br s, 1H, O*H*), 1.88 (s, 30H, C_5*Me*$_5$) ppm. $^{13}C\{^1H\}$ NMR (75 MHz, $CDCl_3$): δ 162.9 (*C$_{ipso}$*), 146.1, 134.8, 129.5 (2× C_5H_4N *C*H), 126.3 (*C_5*Me$_5$), 114.2 (C_5H_4N *C*H), 10.8 (C_5*Me*$_5$) ppm. Signals of $B(C_6F_5)_4^-$: δ 148.4 (br d, J_{CF} = 237 Hz, *o*-C_6F_5), 138.3 (br d, J_{CF} = 246 Hz, *p*-C_6F_5), 136.4 (br d, J_{CF} = 257 Hz, *m*-C_6F_5) ppm. *C$_{ipso}$* of C_6F_5 was not observed. Signals of $B(C_6F_5)_4^-$ in ^{13}C and ^{19}F spectra were the same as for compound **7**. Anal. Calcd. for $C_{49}H_{36}F_{20}ZrO_2NB$ (*M*$_r$ = 1152.82): C 51.05, H 3.15, N 1.21%. Found: C 51.14, H 3.13, N 1.20%.

6.2.2.6 Preparation of **10**

This compound was prepared from **10'** (50 mg, 0.10 mmol), $Ph_3C[B(C_6F_5)_4]$ (90 mg, 0.10 mmol) and Et_3SiH (31 µL, 0.20 mmol). The product was obtained as yellow crystals. Yield: 103 mg (90%).

M.p. 212 °C. ^1H NMR (300 MHz, MeCN-*d*$_3$): δ 7.83 (m, 1H, C_5H_3N C*H*), 6.74 (m, 2H, C_5H_3N C*H*) 2.42 (br s, 3H, C_5H_3N*Me*), 1.81 (s, 30H, C_5*Me*$_5$) ppm. $^{13}C\{^1H\}$ NMR (75 MHz, MeCN-*d*$_3$): δ 146.2 (C_5H_3N *C*H), 123.7 (*C_5*Me$_5$), 116.6, 113.6 (2× C_5H_3N *C*H), 19.0 (C_5H_3N*Me*), 10.8 (C_5*Me*$_5$) ppm. *C$_{ipso}$* and *C*O of C_5H_4N was not observed. Signals of $B(C_6F_5)_4^-$ in ^{13}C and ^{19}F spectra were the same as for compound **7.** Anal. Calcd. for $C_{50}H_{36}F_{20}ZrONB$ (*M*$_r$ = 1148.83): C 52.27, H 3.16, N 1.22%. Found: C 52.22, H 3.17, N 1.24%.

6.2.2.7 Preparation of **11**

This compound was prepared from **11'** (51 mg, 0.10 mmol), $Ph_3C[B(C_6F_5)_4]$ (92 mg, 0.10 mmol) and Et_3SiH (32 µL, 0.20 mmol). The product was obtained as yellow crystals. Yield: 84 mg (73%).

M.p. 202–203. ^1H NMR (300 MHz, MeCN-*d*$_3$): δ 7.58, 7.38, 6.45 (3× m, 1H, C_5H_4N C*H*), 1.79 (s, 30H, C_5*Me*$_5$) ppm. $^{13}C\{^1H\}$ NMR (75 MHz, MeCN-*d*$_3$): δ 155.4 (*C*F), 131.1, 129.4, 127.8 (3× C_5H_3N *C*H), 123.4 (*C_5*Me$_5$), 11.4 (C_5*Me*$_5$) ppm. *C*O was not observed. ^{19}F NMR (282 MHz, MeCN-*d*$_3$): δ −142.8 (C_5H_3NF) ppm. Signals of $B(C_6F_5)_4^-$ in ^{13}C and ^{19}F spectra were the same as for compound **7.** Anal. Calcd. for $C_{49}H_{33}F_{21}ZrONB$ (*M*$_r$ = 1152.79): C 51.05, H 2.89, N 1.22%. Found: C 51.06, H 2.97, N 1.24%.

6.2.2.8 Preparation of **12**

This compound was prepared from **12'** (64 mg, 0.13 mmol), $Ph_3C[B(C_6F_5)_4]$ (125 mg, 0.14 mmol) and Et_3SiH (43 µL, 0.27 mmol). The product was obtained as yellow crystals. Yield: 119 mg (82%).

M.p. 295−300 °C. ^{1}H NMR (300 MHz, MeCN-d_3): δ 8.39, 7.97, 7.54, 7.41 (4× m, 1H, C_5H_4N C*H*), 5.45 (s, 2H, CH_2O), 1.74 (s, 30H, C_5Me_5) ppm. ^{13}C{^{1}H} NMR (75 MHz, MeCN-d_3): δ 150.0, 140.3, 124.3 (3× C_9H_6N *C*H), 122.9 (*C*$_5$Me$_5$), 121.9 (C_9H_6N *C*H), 76.1 (*C*H_2O), 11.8 (C_5Me_5) ppm. C_{ipso} of C_5H_4N was not observed. Signals of $B(C_6F_5)_4^-$ in ^{13}C and ^{19}F spectra were the same as for compound **7.** Anal. Calcd. for $C_{50}H_{36}F_{20}ZrONB$ (M_r = 1148.83): C 52.27, H 3.16, N 1.22%. Found: C 52.33, H 3.11, N 1.24%.

6.2.2.9 Preparation of **13**

This compound was prepared from **13'** (102 mg, 0.19 mmol), $Ph_3C[B(C_6F_5)_4]$ (162 mg, 0.18 mmol) and Et_3SiH (56 µL, 0.35 mmol). The product was obtained as yellow-orange crystals. Yield: 169 mg (76%).

M.p. 198 °C. ^{1}H NMR (300 MHz, MeCN-d_3): δ 8.78, 8.50, 7.66, 7.52, 7.18, 7.02 (6× m, 1H, C_9H_6N C*H*), 1.74 (s, 30H, C_5Me_5) ppm. ^{13}C{^{1}H} NMR (75 MHz, MeCN-d_3): δ 163.6 (*C*O), 151.1 (C_9H_6N *C*H), 146.1 (C_9H_6N *C*), 141.7 (C_9H_6N *C*H), 131.8 (C_9H_6N *C*), 131.7 (C_9H_6N *C*), 131.1, 123.7 (2× C_9H_6N *C*H), 123.6 (*C*$_5$Me$_5$), 116.3, 113.4 (2× C_9H_6N *C*H), 11.7 (C_5Me_5) ppm. Signals of $B(C_6F_5)_4^-$ in ^{13}C and ^{19}F spectra were the same as for compound **7.** Anal. Calcd. for $C_{53}H_{36}F_{20}ZrONB$ (M_r = 1183.16): C 53.72, H 3.06, N 1.18%. Found: C 53.67, H 3.01, N 1.22%.

6.2.3 Preparation of 'half-sandwich' complex **14**

6.2.3.1 Preparation of **14**

14 was prepared by dissolving Cp*$ZrCl_3$ (600 mg, 1.8 mmol) and sodium 8-quinolinolate (722 mg, 4.3 mmol) in 80 ml tetrahydrofuran, in a single Schlenk flask. Thereafter, the procedure follows as 7.2.1.1. The product was obtained as yellow crystals. Yield: 753 mg (76%).

M.p. 280 °C. ^{1}H NMR (300 MHz, $CDCl_3$): δ 8.53, 8.10, 7.96, 7.88, 7.46, 7.41, 7.14 (7× m, 1H, C_9H_6N *C*H) 7.05, 7. 03, 7.02 (3× m, 1H, C_9H_6N *C*H), 6.81, 6.65 (2× m, 1H, C_9H_6N *C*H), 1.92 (s, 15H, C_5Me_5) ppm. ^{13}C{^{1}H} NMR (75 MHz, $CDCl_3$): δ 161.7 (^{a}C_5H_4N *C*O), 161.2 (^{b}C_5H_4N *C*O), 146.0, 145.9 (2× C_9H_6N *C*H), 142.1, 141.3 (2× C_9H_6N *C*), 138.6, 137.5 (2× C_9H_6N *C*H), 130.4 (C_9H_6N *C*H), 129.9, 129.6 (2× C_9H_6N *C*), 129.4 (C_9H_6N *C*H), 123.3 (*C*$_5$Me$_5$), 121.6, 121.2, 115.6, 114.6, 113.6, 113.3 (6× C_9H_6N *C*H), 11.5 (C_5Me_5) ppm. Anal. Calcd. for $C_{28}H_{27}ZrClO_2N_2$ (M_r = 550.20): C 61.12, H 4.95, N 5.09%. Found: C 61.14, H 4.93, N 5.08%.

6.3 Applied methods of characterization

6.3.1 Absorption spectra

UV–VIS absorption spectra were recorded on a Shimadzu UV-1800 spectrometer in argon-saturated dichloromethane solutions.

6.3.2 Emission spectra in solid-state samples and solutions, determination of quantum yields and luminescence lifetimes

Time-resolved luminescence spectra and luminescence kinetics in powdered samples were measured after excitation by a Lambda Physik COMPEX 102 excimer laser (308 nm, pulse width 28 ns), and in DCM solutions after excitation by a Quantel Q Smart 450 Nd YAG laser (355 nm, pulse width ~5 ns) using an LKS 20 laser kinetic spectrometer (Applied Photophysics, UK) equipped with a R928 photomultiplier (Hamamatsu).

Luminescence kinetics were fitted by double (powdered samples) or single (dichloromethane solutions) exponential decay functions. Average lifetimes τ_L were calculated as $\tau_L = \Sigma A_i\tau_i/\Sigma A_i$, where A_i and τ_i are amplitudes and lifetimes of individual processes. Absolute luminescence quantum yields were measured using a Quantaurus C11347 spectrometer (Hamamatsu).

To perform measurements under different concentrations of dissolved oxygen, dichloromethane solutions were saturated with oxygen or argon. Absolute luminescence quantum yields and luminescence spectra were measured using a Quantaurus C11347 spectrometer (Hamamatsu).

Where necessary, a double exponential was used and the average luminescence lifetime was calculated as $\tau_L = (A_1\tau_1 + A_2\tau_2)/(A_1+A_2)$, where A_i and τ_i are the amplitudes and lifetimes of individual processes, respectively.

The rate constants of luminescence quenching by oxygen k_{O2} were estimated using the Stern−Volmer plot: $1/\tau_L = 1/\tau_L(\text{argon}) + k_{O2}\,[O_2]$, where τ_L and $\tau_L(\text{argon})$ are the luminescence lifetimes at a given concentration of oxygen and in argon-saturated solution, respectively. The corresponding concentrations of molecular oxygen $[O_2]$ (1.1×10^{-2} mol L^{-1}) in oxygen-saturated DCM were recalculated using literature data[85]. The fractions of the triplet states quenched by oxygen in air-saturated DCM, F_T^{air}, were calculated as $F_T^{air} = 1 - \tau_L(\text{air})/\tau_L(\text{argon})$.

6.3.3 Singlet oxygen assay

Time-resolved near-infrared luminescence of $O_2(^1\Delta_g)$ at ~1270 nm after excitation by Nd-YAG laser (excitation wavelength of 355 nm) was observed at the right angle to excitation light using a custom-made detector unit (Ge diode Judson J16-8SP-R05M-HS with amplifier) and averaged by 200 times to increase the signal-to-noise ratio. A long-pass filter ($\lambda > 1000$ nm) and bandpass interference filters ($\lambda \sim 1270$ nm) were placed between the sample and detector. The temporal profiles of the singlet oxygen luminescence after excitation of samples (with absorbance at excitation wavelength 0.080±0.001) were fitted to a single-exponential decay function with the exclusion of the initial portion of the plot, which was affected by the formation of singlet oxygen from the triplet states of the sensitizers. The quantum yield of singlet oxygen, Φ_Δ, was estimated by the comparative method using phenalenone (PH, $\Phi_\Delta = 0.96$ in DCM) as a standard.[84]

6.3.4 X-ray diffraction analysis

Diffraction data of **8'**, **10'** ,**12'**, were collected on a Nonius KappaCCD diffractometer equipped with a Bruker APEX II detector (Mo Kα radiation, λ = 0.71073 Å) at 150 K by using an Oxford Cryostream cooler. Collected data were processed by the diffractometer software. The phase problem was solved by intrinsic phasing (SHELXT), and structure models were refined by full matrix least-squares on F2 (SHELX).[86]

The data of **1'–6'**, **1–6**, **7'**, **7, 8, 9', 9** were collected at 150(2) K and **9h2o**, **10**, **11'**, **11**, **13**, **14** at 120(2) K on a Bruker D8 VENTURE Kappa Duo diffractometer with a PHOTON100 detector equipped with a Cryostream Cooler (Oxford Cryosystems), using Mo Kα radiation (λ= 0.71073 Å).

All non-hydrogen atoms were refined anisotropically. All hydrogen atoms were placed in idealized positions and were refined isotropically, except for the NH protons in structures **1–4** and **9h2o**, which were localized on difference Fourier maps and refined isotropically with no constraints imposed. Molecular drawings and geometric parameters were obtained using a recent version of the PLATON program.[87]

6.3.5 Quantum-chemical study

For the examination of structural and photophysical properties, Kohn-Sham DFT calculations were applied. Molecular geometries of the studied neutral complexes and lone cation geometries of the cationic complexes were optimized both in their singlet and triplet states, using the B3LYP exchange-correlation functional,[88] and def2-TZVP basis set,[89-90] as implemented in ORCA 4.2.1.[91-92] Calculations also utilized Grimme's D3 dispersion correction with Becke-Johnson damping (D3BJ),[93-94] and RIJCOSX[95-96] fitting scheme (corresponding def2/J auxiliary basis set was applied).[90] Convergence criteria were tightened and integration grids were expanded significantly above their default values. XRD-determined structures were used as starting geometries for the singlet state optimization procedures. The triplet state optimization procedures utilized the optimized singlet state geometries as starting geometries. Additional optimization procedures were carried out, using the optimized ground state singlet geometries as starting geometries, under the SMD implicit solvent model[97-101] of dichloromethane, later used to model experimental UV-VIS absorption wavelengths and oscillator strengths. All minima were verified by vibrational frequency calculations and utilized an analytical hessian.[102] No imaginary frequencies were found. Using the geometries of both vacuum and dichloromethane optimized ground state singlet, and optimized triplet state geometries, spin-orbit coupling (SOC) corrected TD-DFT[40, 103-105] calculations were carried out, applying 2nd order Douglas-Kroll-Hess (DKH2) Hamiltonian[106-107] and utilizing CAM-B3LYP[108] and PBE0[109] exchange-correlation functionals. PBE0 functional gave the best results for S_0-S_n transitions, whereas CAM-B3LYP for the evolved (S1, T1) geometries. Doing so required using the DKH-def2-TZVP[89] basis set for all non-zirconium/hafnium atoms (the basis set doesn't include these transition metals) and Sapporo-DKH3-

TZP-2012[110] basis set exclusively for metal atoms. RIJCOSX fitting scheme and RI-SOMF(1X)[111] approximation were utilized (corresponding SARC/J auxiliary basis set was applied)[90, 112]. Convergence criteria were tightened, integration grids were expanded significantly above their default values (GRID6,GRIDX6,VERYTIGHT), DKH picture-change effects were included[113] and finite nucleus model was applied[114].

6.4 Photoredox catalysis

Photocatalytic experiments were carried out in 10mL crimp vials with magnetic stir bars. Photocatalyst (**1**, **14)** was added as solid (5,0 ± 0.2 mg each). Vials were sealed and repeatedly degassed and flushed by argon. 4mL of dichloromethane, bromopentafluorophenylbenzene (scaled to 1:0.1) and triethylamine (scaled to 3:0.1) were added to the vial under argon atmosphere, in the listed order. Vials were positioned above a 4W 400 nm LED (Luxeon STAR/0 4×1030 mW@700 mA) placed on a magnetic stirrer and left for 8 hours. The experiments were conducted in duplicates. Control experiments followed the same procedure, with the exception of one of the listed components or light. Conversion was determined by ^{19}F NMR.

^{19}F NMR (282 MHz, $CDCl_3$ + residual DCM 4:1): δ Signals of C_6F_5Br: −132.2, −154.1, −160.1 ppm observed in all control experiments after 8 hours, no product detected. Signals of C_6F_5H: −138.5, −153.5, −161.9 ppm observed in all 'yielding' experiments after 8 hours, no reactant detected.

7 References

1. Kopp, G.; Lean, J. L., A new, lower value of total solar irradiance: Evidence and climate significance. *Geophysical Research Letters* **2011,** *38* (1), n/a-n/a.
2. Cardona, T.; Sedoud, A.; Cox, N.; Rutherford, A. W., Charge separation in Photosystem II: A comparative and evolutionary overview. *Biochimica et Biophysica Acta (BBA) - Bioenergetics* **2012,** *1817* (1), 26-43.
3. Wang, W.; Geiger, J. H.; Borhan, B., The photochemical determinants of color vision. *BioEssays* **2014,** *36* (1), 65-74.
4. Wacker, M.; Holick, M. F., Sunlight and Vitamin D. *Dermato-Endocrinology* **2014,** *5* (1), 51-108.
5. Barbir, F.; Veziroglu, T.; Plassjr, H., Environmental damage due to fossil fuels use. *International Journal of Hydrogen Energy* **1990,** *15* (10), 739-749.
6. Ahearne, J. F., Intergenerational Issues Regarding Nuclear Power, Nuclear Waste, and Nuclear Weapons. *Risk Analysis* **2000,** *20* (6), 763-770.
7. VIII. A dynamical theory of the electromagnetic field. *Philosophical Transactions of the Royal Society of London* **1997,** *155*, 459-512.
8. Halliday, D.; Resnick, R.; Walker, J., *Fundamentals of Physics Extended, 10th Edition*. John Wiley & Sons, Incorporated: 2013.
9. Trabesinger, A., The quantum leap. *Nature Materials* **2010,** *9* (S1), S7-S7.
10. Einstein, A., Über einen die Erzeugung und Verwandlung des Lichtes betreffenden heuristischen Gesichtspunkt. *Annalen der Physik* **1905,** *322* (6), 132-148.
11. Wheaton, B. R., Wave-Particle Duality: A Modern View. In *Compendium of Quantum Physics*, 2009; pp 835-840.
12. Kln, P.; Wirz, J., *Photochemistry of Organic Compounds*. 2009.
13. Sankaran, S.; Ehsani, R., Introduction to the Electromagnetic Spectrum. In *Imaging with Electromagnetic Spectrum*, 2014; pp 1-15.
14. Pawlicki, M.; Collins, H. A.; Denning, R. G.; Anderson, H. L., Two-Photon Absorption and the Design of Two-Photon Dyes. *Angewandte Chemie International Edition* **2009,** *48* (18), 3244-3266.
15. Lavocat, J.-C. Active photonic devices based on liquid crystal elastomers. 2014.
16. Adamo, C.; Jacquemin, D., The calculations of excited-state properties with Time-Dependent Density Functional Theory. *Chem. Soc. Rev.* **2013,** *42* (3), 845-856.
17. Bings, N. H.; Bogaerts, A.; Broekaert, J. A. C., Atomic Spectroscopy: A Review. *Analytical Chemistry* **2010,** *82* (12), 4653-4681.
18. Lever, A. P., Inorganic electronic spectroscopy. *Studies in physical and theoretical chemistry* **1984,** *33*.
19. Marini, A.; Muñoz-Losa, A.; Biancardi, A.; Mennucci, B., What is Solvatochromism? *The Journal of Physical Chemistry B* **2010,** *114* (51), 17128-17135.
20. Fantacci, S.; De Angelis, F.; Selloni, A., Absorption Spectrum and Solvatochromism of the [Ru(4,4‘-COOH-2,2‘-bpy)2(NCS)2] Molecular Dye by Time Dependent Density Functional Theory. *Journal of the American Chemical Society* **2003,** *125* (14), 4381-4387.
21. Born, M.; Oppenheimer, R., Zur Quantentheorie der Molekeln. *Annalen der Physik* **1927,** *389* (20), 457-484.
22. Bernardi, F.; Olivucci, M.; Robb, M. A., Potential energy surface crossings in organic photochemistry. *Chemical Society Reviews* **1996,** *25* (5).
23. Yin, T.-T.; Zhao, Z.-X.; Zhang, H.-X., Theoretical study of the cis–trans isomerization mechanism of a pendant metal-bound azobenzene. *RSC Advances* **2016,** *6* (83), 79879-79889.
24. Schlegel, H. B., Exploring potential energy surfaces for chemical reactions: An overview of some practical methods. *Journal of Computational Chemistry* **2003,** *24* (12), 1514-1527.
25. Atkins, P. W.; Friedman, R. S., *Molecular Quantum Mechanics*. OUP Oxford: 2011.
26. Pianowski, Z. L., Recent Implementations of Molecular Photoswitches into Smart Materials and Biological Systems. *Chemistry – A European Journal* **2019,** *25* (20), 5128-5144.
27. Weinstain, R.; Slanina, T.; Kand, D.; Klán, P., Visible-to-NIR-Light Activated Release: From Small Molecules to Nanomaterials. *Chemical Reviews* **2020,** *120* (24), 13135-13272.

28. Becker, R. S.; Dolan, E.; Balke, D. E., Vibronic Effects in Photochemistry—Competition between Internal Conversion and Photochemistry. *The Journal of Chemical Physics* **1969,** *50* (1), 239-245.

29. Valeur, B.; Berberan-Santos, M. N., A Brief History of Fluorescence and Phosphorescence before the Emergence of Quantum Theory. *Journal of Chemical Education* **2011,** *88* (6), 731-738.

30. Ishikawa-Ankerhold, H. C.; Ankerhold, R.; Drummen, G. P. C., Advanced Fluorescence Microscopy Techniques—FRAP, FLIP, FLAP, FRET and FLIM. *Molecules* **2012,** *17* (4), 4047-4132.

31. del Valle, J. C.; Catalán, J., Kasha's rule: a reappraisal. *Physical Chemistry Chemical Physics* **2019,** *21* (19), 10061-10069.

32. Demchenko, A. P.; Tomin, V. I.; Chou, P.-T., Breaking the Kasha Rule for More Efficient Photochemistry. *Chemical Reviews* **2017,** *117* (21), 13353-13381.

33. Schweitzer, C.; Schmidt, R., Physical Mechanisms of Generation and Deactivation of Singlet Oxygen. *Chemical Reviews* **2003,** *103* (5), 1685-1758.

34. Yarkony, D. R., Nonadiabatic Quantum Chemistry—Past, Present, and Future. *Chemical Reviews* **2011,** *112* (1), 481-498.

35. Baryshnikov, G.; Minaev, B.; Ågren, H., Theory and Calculation of the Phosphorescence Phenomenon. *Chemical Reviews* **2017,** *117* (9), 6500-6537.

36. Liu, Y.; Zhao, J.; Iagatti, A.; Bussotti, L.; Foggi, P.; Castellucci, E.; Di Donato, M.; Han, K.-L., A Revisit to the Orthogonal Bodipy Dimers: Experimental Evidence for the Symmetry Breaking Charge Transfer-Induced Intersystem Crossing. *The Journal of Physical Chemistry C* **2018,** *122* (5), 2502-2511.

37. Giussani, A.; Farahani, P.; Martínez-Muñoz, D.; Lundberg, M.; Lindh, R.; Roca-Sanjuán, D., Molecular Basis of the Chemiluminescence Mechanism of Luminol. *Chemistry – A European Journal* **2019,** *25* (20), 5202-5213.

38. Cravcenco, A.; Hertzog, M.; Ye, C.; Iqbal, M. N.; Mueller, U.; Eriksson, L.; Börjesson, K., Multiplicity conversion based on intramolecular triplet-to-singlet energy transfer. *Science Advances* **2019,** *5* (9).

39. Bridgeman, A. J., Modeling the Vibronic Spectra of Transition Metal Complexes: The Ligand-Field Spectrum of [PtCl4]2−. *Inorganic Chemistry* **2008,** *47* (11), 4817-4825.

40. de Souza, B.; Farias, G.; Neese, F.; Izsák, R., Predicting Phosphorescence Rates of Light Organic Molecules Using Time-Dependent Density Functional Theory and the Path Integral Approach to Dynamics. *Journal of Chemical Theory and Computation* **2019,** *15* (3), 1896-1904.

41. Huenerbein, R.; Grimme, S., Time-dependent density functional study of excimers and exciplexes of organic molecules. *Chemical Physics* **2008,** *343* (2-3), 362-371.

42. Thorning, F.; Strunge, K.; Jensen, F.; Ogilby, P. R., The complex between molecular oxygen and an organic molecule: modeling optical transitions to the intermolecular charge-transfer state. *Physical Chemistry Chemical Physics* **2021,** *23* (28), 15038-15048.

43. Gias Uddin, M.; Zafrul Aza, A. T. M., A Novel Oligo-DNA Probe Carrying Non-nucleosidic Silylated Pyrene Derivatives: Synthesis and Excimer Forming Ability. *American Journal of Biochemistry and Molecular Biology* **2012,** *3* (1), 175-181.

44. Mikhnenko, O. V.; Blom, P. W. M.; Nguyen, T.-Q., Exciton diffusion in organic semiconductors. *Energy & Environmental Science* **2015,** *8* (7), 1867-1888.

45. Dexter, D. L., A Theory of Sensitized Luminescence in Solids. *The Journal of Chemical Physics* **1953,** *21* (5), 836-850.

46. Monro, S.; Colón, K. L.; Yin, H.; Roque, J.; Konda, P.; Gujar, S.; Thummel, R. P.; Lilge, L.; Cameron, C. G.; McFarland, S. A., Transition Metal Complexes and Photodynamic Therapy from a Tumor-Centered Approach: Challenges, Opportunities, and Highlights from the Development of TLD1433. *Chemical Reviews* **2018,** *119* (2), 797-828.

47. García-Fresnadillo, D., Singlet Oxygen Photosensitizing Materials for Point-of-Use Water Disinfection with Solar Reactors. *ChemPhotoChem* **2018,** *2* (7), 512-534.

48. Ghogare, A. A.; Greer, A., Using Singlet Oxygen to Synthesize Natural Products and Drugs. *Chemical Reviews* **2016,** *116* (17), 9994-10034.

49. Niculescu, A.-G.; Grumezescu, A. M., Photodynamic Therapy—An Up-to-Date Review. *Applied Sciences* **2021,** *11* (8).

50. Padmanabhan, N. T.; John, H., Titanium dioxide based self-cleaning smart surfaces: A short review. *Journal of Environmental Chemical Engineering* **2020,** *8* (5).

51. Prier, C. K.; Rankic, D. A.; MacMillan, D. W. C., Visible Light Photoredox Catalysis with Transition Metal Complexes: Applications in Organic Synthesis. *Chemical Reviews* **2013,** *113* (7), 5322-5363.

52. Kalyanasundaram, K., Photophysics, photochemistry and solar energy conversion with tris(bipyridyl)ruthenium(II) and its analogues. *Coordination Chemistry Reviews* **1982,** *46*, 159-244.

53. Romero, N. A.; Nicewicz, D. A., Organic Photoredox Catalysis. *Chemical Reviews* **2016,** *116* (17), 10075-10166.

54. Meyer, A. U.; Slanina, T.; Yao, C.-J.; König, B., Metal-Free Perfluoroarylation by Visible Light Photoredox Catalysis. *ACS Catalysis* **2015,** *6* (1), 369-375.

55. Twilton, J.; Le, C.; Zhang, P.; Shaw, M. H.; Evans, R. W.; MacMillan, D. W. C., The merger of transition metal and photocatalysis. *Nature Reviews Chemistry* **2017,** *1* (7).

56. U. Dighe, S.; Juliá, F.; Luridiana, A.; Douglas, J. J.; Leonori, D., A photochemical dehydrogenative strategy for aniline synthesis. *Nature* **2020,** *584* (7819), 75-81.

57. Brandl, F.; Bergwinkl, S.; Allacher, C.; Dick, B., Consecutive Photoinduced Electron Transfer (conPET): The Mechanism of the Photocatalyst Rhodamine 6G. *Chemistry – A European Journal* **2020,** *26* (35), 7946-7954.

58. Ghosh, I.; Ghosh, T.; Bardagi, J. I.; Konig, B., Reduction of aryl halides by consecutive visible light-induced electron transfer processes. *Science* **2014,** *346* (6210), 725-728.

59. Zhang, Q.-C.; Xiao, H.; Zhang, X.; Xu, L.-J.; Chen, Z.-N., Luminescent oligonuclear metal complexes and the use in organic light-emitting diodes. *Coordination Chemistry Reviews* **2019,** *378*, 121-133.

60. Pashaei, B.; Karimi, S.; Shahroosvand, H.; Abbasi, P.; Pilkington, M.; Bartolotta, A.; Fresta, E.; Fernandez-Cestau, J.; Costa, R. D.; Bonaccorso, F., Polypyridyl ligands as a versatile platform for solid-state light-emitting devices. *Chemical Society Reviews* **2019,** *48* (19), 5033-5139.

61. Bizzarri, C.; Spuling, E.; Knoll, D. M.; Volz, D.; Bräse, S., Sustainable metal complexes for organic light-emitting diodes (OLEDs). *Coordination Chemistry Reviews* **2018,** *373*, 49-82.

62. Zhang, K. Y.; Yu, Q.; Wei, H.; Liu, S.; Zhao, Q.; Huang, W., Long-Lived Emissive Probes for Time-Resolved Photoluminescence Bioimaging and Biosensing. *Chemical Reviews* **2018,** *118* (4), 1770-1839.

63. Hagfeldt, A.; Boschloo, G.; Sun, L.; Kloo, L.; Pettersson, H., Dye-Sensitized Solar Cells. *Chemical Reviews* **2010,** *110* (11), 6595-6663.

64. Pashaei, B.; Shahroosvand, H.; Graetzel, M.; Nazeeruddin, M. K., Influence of Ancillary Ligands in Dye-Sensitized Solar Cells. *Chemical Reviews* **2016,** *116* (16), 9485-9564.

65. Niculescu, A.-G.; Grumezescu, A. M., Photodynamic Therapy—An Up-to-Date Review. *Applied Sciences* **2021,** *11* (8), 3626.

66. Minaev, B.; Baryshnikov, G.; Agren, H., Principles of phosphorescent organic light emitting devices. *Phys. Chem. Chem. Phys.* **2014,** *16* (5), 1719-1758.

67. Czerwieniec, R.; Leitl, M. J.; Homeier, H. H. H.; Yersin, H., Cu(I) complexes – Thermally activated delayed fluorescence. Photophysical approach and material design. *Coordination Chemistry Reviews* **2016,** *325*, 2-28.

68. Zhang, Y.; Petersen, J. L.; Milsmann, C., A Luminescent Zirconium(IV) Complex as a Molecular Photosensitizer for Visible Light Photoredox Catalysis. *Journal of the American Chemical Society* **2016,** *138* (40), 13115-13118.

69. Zhang, Y.; Lee, T. S.; Petersen, J. L.; Milsmann, C., A Zirconium Photosensitizer with a Long-Lived Excited State: Mechanistic Insight into Photoinduced Single-Electron Transfer. *Journal of the American Chemical Society* **2018,** *140* (18), 5934-5947.

70. Garon, S.; Lau, E. K. C.; Chew, S.-L.; Lee, S. T.; Thompson, M. E., Metal (IV) tetras (8-hydroxyquinoline) (M = Zr, Hf) used as electroluminescent material and electron-transport layer in OLEDs. *Journal of the Society for Information Display* **2005,** *13* (5).

71. Shahroosvand, H.; Nasouti, F.; Mohajerani, E.; Khabbazi, A., Synthesis, characterization and optical properties of novel N donor ligands-chelated zirconium(IV) complexes. *Optical Materials* **2012,** *35* (1), 79-84.

72. Kenney, J. W.; Boone, D. R.; Striplin, D. R.; Chen, Y. H.; Hamar, K. B., Electronic luminescence spectra of charge transfer states of titanium(IV) metallocenes. *Organometallics* **2002,** *12* (9), 3671-3676.

73. Patrick, E. L.; Ray, C. J.; Meyer, G. D.; Ortiz, T. P.; Marshall, J. A.; Brozik, J. A.; Summers, M. A.; Kenney, J. W., Non-Localized Ligand-to-Metal Charge Transfer Excited States in (Cp)2Ti(IV)(NCS)2. *Journal of the American Chemical Society* **2003,** *125* (18), 5461-5470.

74. Vivian Wing-Wah, Y.; Qi, G.-Z.; Cheung, K.-K., Synthesis of luminescent zirconium thiolate complexes. Crystal structures of (η5-C5H5)2Zr(SC6H4Cl-p)2 and [(η5-C5H5)2Zr(SC6H4OMe-p)]2O. *Journal of Organometallic Chemistry* **1997,** *548* (2), 289-294.

75. Wing-Wah Yam, V.; Qi, G.-Z.; Cheung, K.-K., Synthesis, emission and molecular orbital studies of luminescent zirconium thiolate complexes. Crystal structure of [Zr(η5-C5Me5)2(SBun)2]. *Journal of the Chemical Society, Dalton Transactions* **1998,** (11), 1819-1824.

76. Yam, V. W.-W.; Qi, G.-Z.; Cheung, K.-K., Synthesis, Emission, and Molecular Orbital Studies of Luminescent Hafnium Thiolate Complexes. Crystal Structures of (η5-C5Me5)2Hf(SR)2 (R = nBu, C6H5, C6H4OMe-p). *Organometallics* **1998,** *17* (25), 5448-5453.

77. Loukova, G. V.; Smirnov, V. A., Phosphorescent ligand-to-metal charge-transfer excited states in the group IVB metallocene triad. *Chemical Physics Letters* **2000,** *329* (5-6), 437-442.

78. Loukova, G. V.; Huhn, W.; Vasiliev, V. P.; Smirnov, V. A., Ligand-to-Metal Charge Transfer Excited States with Unprecedented Luminescence Yield in Fluid Solution. *The Journal of Physical Chemistry A* **2007,** *111* (20), 4117-4121.

79. Pritchard, V. E.; Thorp-Greenwood, F. L.; Balasingham, R. G.; Williams, C. F.; Kariuki, B. M.; Platts, J. A.; Hallett, A. J.; Coogan, M. P., Simple Polyphenyl Zirconium and Hafnium Metallocene Room-Temperature Lumophores for Cell Imaging. *Organometallics* **2013,** *32* (12), 3566-3569.

80. Fermi, A.; Gualandi, A.; Bergamini, G.; Cozzi, P. G., Shining Light on Ti

IV

Complexes: Exceptional Tools for Metallaphotoredox Catalysis. *European Journal of Organic Chemistry* **2020,** *2020* (45), 6955-6965.

81. Zhang, Z.; Hilche, T.; Slak, D.; Rietdijk, N. R.; Oloyede, U. N.; Flowers, R. A.; Gansäuer, A., Titanocenes as Photoredox Catalysts Using Green-Light Irradiation. *Angewandte Chemie International Edition* **2020,** *59* (24), 9355-9359.

82. Dunlop, D.; Večeřa, M.; Gyepes, R.; Kubát, P.; Lang, K.; Horáček, M.; Pinkas, J.; Šimková, L.; Liška, A.; Lamač, M., Luminescent Cationic Group 4 Metallocene Complexes Stabilized by Pendant N-Donor Groups. *Inorganic Chemistry* **2021,** *60* (10), 7315-7328.

83. Večeřa, M.; Varga, V.; Císařová, I.; Pinkas, J.; Kucharczyk, P.; Sedlařík, V.; Lamač, M., Group 4 Metal Complexes of Chelating Cyclopentadienyl-ketimide Ligands. *Organometallics* **2016,** *35* (5), 785-798.

84. Martí, C.; Jürgens, O.; Cuenca, O.; Casals, M.; Nonell, S., Aromatic ketones as standards for singlet molecular oxygen O2(1Δg) photosensitization. Time-resolved photoacoustic and near-IR emission studies. *J. Photochem. Photobiol. A* **1996,** *97* (1), 11-18.

85. Sato, T.; Hamada, Y.; Sumikawa, M.; Araki, S.; Yamamoto, H., Solubility of Oxygen in Organic Solvents and Calculation of the Hansen Solubility Parameters of Oxygen. *Ind. Eng. Chem. Res.* **2014,** *53* (49), 19331-19337.

86. Sheldrick, G. M., Crystal structure refinement withSHELXL. *Acta Crystallographica Section C Structural Chemistry* **2015,** *71* (1), 3-8.

87. Spek, A. L., Structure validation in chemical crystallography. *Acta Crystallographica Section D Biological Crystallography* **2009,** *65* (2), 148-155.

88. Becke, A. D., Density-Functional Thermochemistry .3. The Role of Exact Exchange. *J Chem Phys* **1993,** *98* (7), 5648-5652.

89. Weigend, F.; Ahlrichs, R., Balanced basis sets of split valence, triple zeta valence and quadruple zeta valence quality for H to Rn: Design and assessment of accuracy. *Physical Chemistry Chemical Physics* **2005,** *7* (18), 3297-3305.

90. Weigend, F., Accurate Coulomb-fitting basis sets for H to Rn. *Physical Chemistry Chemical Physics* **2006,** *8* (9), 1057-1065.

91. Neese, F., The ORCA program system. *WIREs Computational Molecular Science* **2012,** *2* (1), 73-78.

92. Neese, F., Software update: the ORCA program system, version 4.0. *WIREs Computational Molecular Science* **2018,** *8* (1), e1327.

93. Grimme, S.; Ehrlich, S.; Goerigk, L., Effect of the damping function in dispersion corrected density functional theory. *Journal of Computational Chemistry* **2011,** *32* (7), 1456-1465.

94. Grimme, S.; Antony, J.; Ehrlich, S.; Krieg, H., A consistent and accurate ab initio parametrization of density functional dispersion correction (DFT-D) for the 94 elements H-Pu. *The Journal of Chemical Physics* **2010,** *132* (15), 154104.

95. Neese, F.; Wennmohs, F.; Hansen, A.; Becker, U., Efficient, approximate and parallel Hartree–Fock and hybrid DFT calculations. A 'chain-of-spheres' algorithm for the Hartree–Fock exchange. *Chemical Physics* **2009,** *356* (1), 98-109.

96. Izsák, R.; Neese, F., An overlap fitted chain of spheres exchange method. *The Journal of Chemical Physics* **2011,** *135* (14), 144105.

97. Cancès, E.; Mennucci, B.; Tomasi, J., A new integral equation formalism for the polarizable continuum model: Theoretical background and applications to isotropic and anisotropic dielectrics. *The Journal of Chemical Physics* **1997,** *107* (8), 3032-3041.

98. Barone, V.; Cossi, M.; Tomasi, J., A new definition of cavities for the computation of solvation free energies by the polarizable continuum model. *The Journal of Chemical Physics* **1997,** *107* (8), 3210-3221.

99. Miertuš, S.; Scrocco, E.; Tomasi, J., Electrostatic interaction of a solute with a continuum. A direct utilizaion of AB initio molecular potentials for the prevision of solvent effects. *Chemical Physics* **1981,** *55* (1), 117-129.

100. Cossi, M.; Barone, V.; Cammi, R.; Tomasi, J., Ab initio study of solvated molecules: a new implementation of the polarizable continuum model. *Chemical Physics Letters* **1996,** *255* (4), 327-335.

101. Marenich, A. V.; Cramer, C. J.; Truhlar, D. G., Universal Solvation Model Based on Solute Electron Density and on a Continuum Model of the Solvent Defined by the Bulk Dielectric Constant and Atomic Surface Tensions. *The Journal of Physical Chemistry B* **2009,** *113* (18), 6378-6396.

102. Garcia-Ratés, M.; Neese, F., Efficient implementation of the analytical second derivatives of hartree–fock and hybrid DFT energies within the framework of the conductor-like polarizable continuum model. *Journal of Computational Chemistry* **2019,** *40* (20), 1816-1828.

103. Bauernschmitt, R.; Ahlrichs, R., Treatment of electronic excitations within the adiabatic approximation of time dependent density functional theory. *Chemical Physics Letters* **1996,** *256* (4), 454-464.

104. Scalmani, G.; Frisch, M. J.; Mennucci, B.; Tomasi, J.; Cammi, R.; Barone, V., Geometries and properties of excited states in the gas phase and in solution: Theory and application of a time-dependent density functional theory polarizable continuum model. *The Journal of Chemical Physics* **2006,** *124* (9), 094107.

105. Furche, F.; Ahlrichs, R., Adiabatic time-dependent density functional methods for excited state properties. *The Journal of Chemical Physics* **2002,** *117* (16), 7433-7447.

106. Hess, B. A., Applicability of the no-pair equation with free-particle projection operators to atomic and molecular structure calculations. *Physical Review A* **1985,** *32* (2), 756-763.

107. Douglas, M.; Kroll, N. M., Quantum electrodynamical corrections to the fine structure of helium. *Annals of Physics* **1974,** *82* (1), 89-155.

108. Yanai, T.; Tew, D. P.; Handy, N. C., A new hybrid exchange–correlation functional using the Coulomb-attenuating method (CAM-B3LYP). *Chemical Physics Letters* **2004,** *393* (1), 51-57.

109. Adamo, C.; Barone, V., Toward reliable density functional methods without adjustable parameters: The PBE0 model. *The Journal of Chemical Physics* **1999,** *110* (13), 6158-6170.

110. Noro, T.; Sekiya, M.; Koga, T., Sapporo-(DKH3)-nZP (n = D, T, Q) sets for the sixth period s-, d-, and p-block atoms. *Theoretical Chemistry Accounts* **2013,** *132* (5), 1363.

111. Neese, F., Efficient and accurate approximations to the molecular spin-orbit coupling operator and their use in molecular g-tensor calculations. *The Journal of Chemical Physics* **2005,** *122* (3), 034107.

112. Pantazis, D. A.; Neese, F., All-electron scalar relativistic basis sets for the 6p elements. *Theoretical Chemistry Accounts* **2012,** *131* (11), 1292.

113. Sandhoefer, B.; Neese, F., One-electron contributions to the g-tensor for second-order Douglas–Kroll–Hess theory. *The Journal of Chemical Physics* **2012,** *137* (9), 094102.

114. Visscher, L.; Dyall, K. G., DIRAC–FOCK ATOMIC ELECTRONIC STRUCTURE CALCULATIONS USING DIFFERENT NUCLEAR CHARGE DISTRIBUTIONS. *Atomic Data and Nuclear Data Tables* **1997,** *67* (2), 207-224.

8 Supplementary information

8.1. X-ray crystallography

Table S1: Selected crystallographic data for compounds **7’-12’**, **7-11, 13** and **9h2o**.

Compound	**7’**	**7**	**8’**	**8**	**9’**	**9**	**9h2o**
Formula	$C_{26}H_{34}ClNO_2Zr$	$C_{50}H_{34}BF_{20}NO_2Zr$	$C_{26}H_{34}ClNO_2Hf$	$C_{50}H_{34}BF_{20}NO_2Hf$	$C_{25}H_{34}ClNOZr$	$C_{49}H_{34}BF_{20}NOZr$	$C_{49}H_{36}BF_{20}NO_2Zr$
M (g mol^{-1})	519.21	1162.81	606.48	1250.08	491.20	1134.80	1152.82
Crystal system	monoclinic	monoclinic	monoclinic	monoclinic	monoclinic	triclinic	triclinic
Space group	$P2_1$/n (No. 14)	$P2_1$/c (No. 14)	$P2_1$/n (No. 14)	$P2_1$/c (No. 14)	$P2_1$/m (No. 11)	P–1 (No. 2)	P–1 (No. 2)
a (Å)	14.0909(5)	10.7083(5)	14.0418(6)	10.7168(5)	8.6088(4)	10.766(2)	10.6801(6)
b (Å)	11.6028(4)	15.5410(8)	11.5724(5)	15.5612(8)	14.4099(6)	14.817(3)	15.0917(8)
c (Å)	14.4016(5)	27.7452(13)	14.3986(6)	27.6568(13)	9.6427(5)	15.208(3)	15.2779(9)
α (°)	90	90	90	90	90	71.93(3)	71.638(2)
β (°)	91.3650(14)	97.494(2)	91.300(2)	97.555(2)	102.319(2)	78.48(3)	84.773(2)
γ (°)	90	90	90	90	90	86.74(3)	78.441(2)
V (Å^3)	2353.91(14)	4577.9(4)	2339.1(2)	4572.2(4)	1168.65(10)	2259.8(9)	2288.7(2)
Z	4	4	4	4	2	2	2
D_{calc} (g mL^{-1})	1.465	1.687	1.722	1.816	1.396	1.668	1.673
μ (MoK_{α}) mm^{-1}	0.60	0.37	4.60	2.41	0.60	0.37	0.37
T_{min}, T_{max}	0.82, 0.92	0.87, 0.97	0.22, 0.27	0.55, 0.81	0.84, 0.88	0.82, 0.95	0.93, 0.97
Diffractions total	59 163	88 476	34 230	212 716	46 569	10 942	85 282
Unique/observed[a] diffractions	5 395/4 851	10 503/6 435	5 375/5 220	11 099/10 101	2 932/2 848	10 942/9 616	10 500/8 888
R_{int} (%)[b]	4.3	16.9	1.6	4.4	1.9	0.0	5.6
R (observed data) (%)[c]	2.16	5.65	1.50	1.99	1.79	5.37	3.95
R, wR (all data) (%)[c]	2.67, 5.30	11.76, 13.14	1.57, 3.62	2.42, 4.64	1.86, 4.70	6.93, 10.96	5.07, 9.28
$\Delta\rho$ (e Å^{-3})	0.36, –0.34	1.34, –1.07	0.94, –0.73	0.73, –0.86	0.32, −0.36	1.43, –0.77	2.99, –1.04

[a] Diffractions with $I_o > 2\sigma(I_o)$.
[b] $R_{int} = \Sigma|F_o^2 - \langle F_o^2\rangle|/\Sigma F_o^2$, where $\langle F_o^2\rangle$ is the average intensity of symmetry-equivalent diffractions.
[c] $R = \Sigma||F_o| - |F_c||/\Sigma|F_o|$, $wR = [\Sigma\{w(F_o^2 - F_c^2)^2\}/\Sigma\, w(F_o^2)^2]^{1/2}$

Table S1 continued. Selected crystallographic data for compounds **7'-12', 7-11, 13 and 9h2o**.

Compound	**10'**	**10**	**11'**	**11**	**12'**	**13**	**14**
Formula	$C_{26}H_{36}ClNOZr$	$C_{50}H_{36}BF_{20}NOZr$	$C_{25}H_{33}ClFNOZr$	$C_{49}H_{33}BF_{21}NOZr$	$C_{26}H_{36}ClNOZr$	$C_{53}H_{36}BCl_{0.05}F_{20}NOZr$	$C_{28}H_{27}ClN_2O_2Zr$
M (g mol^{-1})	505.23	1148.83	509.19	1152.79	505.23	1186.81	550.18
Crystal system	orthorhombic	triclinic	monoclinic	triclinic	monoclinic	monoclinic	triclinic
Space group	Pnma (No. 62)	P–1 (No. 2)	$P2_1$/m (No. 11)	P–1 (No. 2)	$P2_1$/n (No. 14)	$P2_1$/c (No. 14)	P–1 (No. 2)
a (Å)	11.2171(4)	10.9000(7)	8.5836(2)	10.6835(7)	9.9059(3)	15.1492(7)	10.0888(4)
b (Å)	14.0318(4)	13.2626(9)	14.3375(4)	14.8759(11)	14.9522(5)	18.7399(8)	10.6237(4)
c (Å)	15.2498(6)	16.7874(12)	9.6617(2)	15.2470(12)	16.5195(6)	18.8334(9)	11.8999(4)
α (°)	90	100.872(2)	90	71.873(3)	90	90	83.3080(10)
β (°)	90	100.456(2)	102.0110(10)	77.595(2)	96.7430(10)	93.987(2)	80.4870(10)
γ (°)	90	94.985(2)	90	86.954(3)	90	90	70.9430(10)
V (Å^3)	2400.26(14)	2325.2(3)	1163.01(5)	2248.9(3)	2429.86(14)	5333.8(4)	1186.28(8)
Z	4	2	2	2	4	4	2
D_{calc} (g mL^{-1})	1.398	1.641	1.454	1.702	1.381	1.478	1.540
μ (MoK$_\alpha$) mm^{-1}	0.59	0.36	0.61	0.37	0.58	0.32	0.61
T_{min}, T_{max}	0.70, 0.86	0.82, 0.88	0.84, 0.91	0.89, 0.95	0.66, 0.76	0.78, 0.86	0.88, 0.94
Diffractions total	3 578	105 489	25 677	10 342	33 178	137 691	42 860
Unique/observed[a] diffractions	3 578/3 045	10 706/9 965	2 781/2 671	10 342/9 341	5 593/5 137	12 293/10 864	5 452/4 844
R_{int} (%)[b]	0.0	2.4	2.83	0.0	1.9	3.3	4.6
R (observed data) (%)[c]	6.22	4.41	1.90	4.76	2.03	3.98	2.61
R, wR (all data) (%)[c]	7.54, 17.00	4.76, 10.87	2.02, 5.12	5.75, 11.27	2.34, 5.41	4.62, 10.00	3.28, 6.10
Δρ (e Å^{-3})	0.60, –0.93	2.25, –1.54	0.38, –0.36	2.01, –0.81	0.31, –0.29	1.22, –1.24	0.36, −0.53

[a] Diffractions with $I_o > 2\sigma(I_o)$.
[b] $R_{int} = \Sigma|F_o^2 - \langle F_o^2\rangle|/\Sigma F_o^2$, where $\langle F_o^2\rangle$ is the average intensity of symmetry-equivalent diffractions.
[c] $R = \Sigma||F_o| - |F_c||/\Sigma|F_o|$, $wR = [\Sigma\{w(F_o^2 - F_c^2)^2\}/\Sigma\, w(F_o^2)^2]^{1/2}$